

Wave-function mapping of electronic states in nanostructures by scanning tunneling spectroscopy

Dissertation
zur Erlangung des Doktorgrades
des Fachbereichs Physik
der Universität Hamburg

vorgelegt von
Theophilos Maltezopoulos
aus Hamburg

Hamburg
2004

The work described in this thesis is done at the
Institute of Applied Physics, University of Hamburg,
in the group of Prof. Dr. Roland Wiesendanger.

Gutachter der Dissertation:
Prof. Dr. Roland Wiesendanger
Prof. Dr. Detlef Heitmann

Gutachter der Disputation:
Prof. Dr. Roland Wiesendanger
Prof. Dr. Wolfgang Hansen

Datum der Disputation:
06. Februar 2004

Vorsitzender des Prüfungsausschusses:
Dr. Stefan Kettmann

Vorsitzender des Promotionsausschusses:
Prof. Dr. Roland Wiesendanger

Dekan des Fachbereichs Physik:
Prof. Dr. Günter Huber

Abstract

The following nanostructures are studied by scanning tunneling microscopy and spectroscopy and atomic force microscopy:

- Strain-induced InAs quantum dots produced by molecular beam epitaxy
- InAs, InP, and CdSe nanocrystals synthesized by colloidal chemistry
- Single-walled carbon nanotubes prepared by laser evaporation technique

Strain-induced **InAs quantum dots** are grown on GaAs(001) by molecular beam epitaxy and are subsequently investigated by low temperature ultra-high vacuum scanning tunneling spectroscopy. It turned out that an ultra-high vacuum transfer system between molecular beam epitaxy and scanning tunneling microscope had to be established in order to achieve highly reproducible results. Above the quantum dots, several peaks are found in dI/dV curves which belong to different single-electron states of the particular dot. Spatially resolved dI/dV images at the peak positions reveal a (000), (100), (010), (200), and (300) character of the squared wave function, where the numbers describe the number of nodes in $[1\bar{1}0]$, $[110]$, and $[001]$ direction, respectively. The total number and the energetic sequence of the states are found to be different for different dots. The (010) state, for example, is often missing even if (200) and (300) states are present. This electronic anisotropy is attributed to a shape asymmetry of the quantum dots.

InAs, InP, and CdSe nanocrystals are chemically prepared in solution and not in ultra-high vacuum. This requires a preparation technique compatible with scanning probe methods. Therefore, a scanning probe equitable preparation technique for deposition of nanocrystals on Au on mica substrates is developed. Air tapping-mode atomic force microscopy and scanning tunneling microscopy images show randomly shaped nanocrystal agglomerates.

Single-walled carbon nanotubes are also deposited on Au on mica substrates and measured with low temperature ultra-high vacuum scanning tunneling microscopy and spectroscopy. Atomic resolution is obtained and metallic or semi-conducting tubes are identified. Additionally, peaks are found in dI/dV curves on metallic tubes close to E_{Fermi} which are attributed to defect-induced confined states within the extended metallic tube. Spatially resolved spectroscopy reveal the extension of the confined regions to be about 20–40 nm. Thus, the quantum wire appears to be fragmented into quantum dots separated by defects. This is a direct evidence for defect induced backscattering within metallic carbon nanotubes.

Inhaltsangabe

Die folgenden Nanostrukturen wurden mittels Rastertunnelmikroskopie und -Spektroskopie und Rasterkraftmikroskopie untersucht:

- Mittels Molekularstrahlepitaxie hergestellte verspannungsinduzierte InAs Quantenpunkte
- Naßchemisch hergestellte InAs, InP und CdSe Nanokristalle
- Mittels Laserverdampfungstechnik hergestellte einwandige Kohlenstoff-Nanoröhren.

Auf GaAs(001) wurden verspannungsinduziert **InAs Quantenpunkte** mittels Molekularstrahlepitaxie gewachsen und anschließend mittels Tieftemperatur-Ultrahochvakuum-Rastertunnelspektroskopie untersucht. Ein Ultrahochvakuum-Transfer zwischen Molekularstrahlepitaxie und Rastertunnelmikroskop wurde etabliert, weil nur so reproduzierbare Ergebnisse erzielt werden konnten. Auf den Quantenpunkten wurden mehrere Peaks in dI/dV -Kurven aufgelöst, welche zu unterschiedlichen Einzelchenzuständen des jeweiligen Dots gehören. An den Peak-Positionen zeigen ortsaufgelöste dI/dV -Bilder das Betragsquadrat der Wellenfunktionen von (000), (100), (010), (200) und (300) Zuständen, wobei die Zahlen für die Anzahl der Knoten in $[1\bar{1}0]$, $[110]$ und $[001]$ Richtung stehen. Die Anzahl der Zustände und die energetische Ordnung sind bei unterschiedlichen Quantenpunkten unterschiedlich. Sehr häufig fehlt der (010) Zustand, obwohl (200) und (300) Zustände gefunden werden. Diese elektronische Anisotropie wird mit der Formanisotropie der Quantenpunkte erklärt.

Naßchemisch hergestellte **InAs, InP und CdSe Nanokristalle** liegen in Lösung und nicht im Ultrahochvakuum vor. Das erfordert eine rastersondenadäquate Präparation. Diese wurde auf einer Au auf Glimmer Oberfläche realisiert. Tapping-Mode-Rasterkraftmikroskopie und Rastertunnelmikroskopie zeigen unterschiedlich geformte Nanokristall-Agglomerate.

Einwandige Kohlenstoff-Nanoröhren wurden auch auf einer Au auf Glimmer Oberfläche deponiert und anschließend mittels Tieftemperatur-Ultrahochvakuum-Rastertunnelspektroskopie untersucht. Es konnte atomare Auflösung erzielt werden und metallische und halbleitende Nanoröhren identifiziert werden. Zusätzlich wurden Peaks in dI/dV -Kurven um E_F auf metallischen Nanoröhren gefunden, welche als defektinduzierte quantisierte Zustände identifiziert werden konnten. Die Ausdehnung der quantisierten Zustände wurde mittels ortsaufgelöster Spektroskopie zu 20–40 nm bestimmt. Der Quantendraht erscheint also fragmentiert in Quantenpunkte, welche über Defekte voneinander getrennt werden. Dies ist ein direkter Beweis für defektinduzierte Rückwärtsstreuung in metallischen Nanoröhren.

Contents

1	Introduction	1
2	Scanning probe methods	3
2.1	Scanning tunneling microscopy and spectroscopy	3
2.1.1	Principle	3
2.1.2	Theory	4
2.1.3	Low temperature UHV STM	8
2.2	Atomic force microscopy	11
3	InAs quantum dots	13
3.1	Basic properties	13
3.2	Sample preparation	17
3.3	STS results: Wave-function mapping	22
3.4	Conductive AFM results	32
3.5	Scanning capacitance microscopy results	35
4	InAs, InP, and CdSe nanocrystals	39
4.1	Basic properties	39
4.2	Sample preparation	43
5	Single-walled carbon nanotubes	51
5.1	Basic properties	51
5.2	Sample preparation	56
5.3	STS results: Defect-induced confined states	58
6	Summary and outlook	65
	Bibliography	67
	Publications	77
	Contributions to conferences and workshops	79
	Acknowledgement	81

Chapter 1

Introduction

Nanoscience is one of the most growing fields in science including all topics in physics, chemistry, and biology, which are related to phenomena characteristic for the nanometer scale [1 nm= 10^{-9} m].

Besides the scientific interest to understand the basic properties of nanostructures a nanotechnology can be developed. Nanotechnology includes, for example, single-electron nanodevices, self-organized nanomaterials for laser applications, and new tools to build nanostructures on an atom-by-atom basis.

One of the most basic nanostructures is a semiconductor quantum dot (QD). It exhibits atomic-like single-electron states due to the size quantization and is therefore also called an "artificial atom". Two kinds of semiconductor QDs are studied in this thesis: Pyramidal shaped InAs QDs, which are grown by molecular beam epitaxy (MBE), and spherical shaped InAs, InP, and CdSe nanocrystals, which are synthesized by colloidal chemistry.

MBE grown InAs QDs are used as new laser materials [1, 2] or single-photon sources [3]. CdSe and CdSe/ZnS core-shell nanocrystals display strong luminescence, which enables technological applications such as thin film light emitting devices [4], optical amplifiers for telecommunication networks [5], or even biological labeling [6].

The second part of this thesis is focussed on single-walled carbon nanotubes (SWCNTs). These tiny and hollow quantum wires can be metallic or semiconducting and have also a wide range of applications [7–10]: They are ultra strong, chemically inert and flexible, and they are used, for example, as field emitters in long-living lamps as well as storage media for H₂ gas. An application as field effect transistors, which permit high currents up to 25 μ A per tube, is reported [11]. Similar high current densities up to 10^9 A/cm² have been demonstrated elsewhere [12]. Nanotubes can even act as point electron sources in high-resolution electron beam instruments [13]. Moreover, nanotubes can be self-assembled into up to 30 cm long yarns [14]. Therefore, they are even considered for macroscopic applications such as bulletproof vests or as materials to block or polarize electromagnetic waves.

One basic electronic property of each nanostructure is the local density of states:

$$LDOS(E, r) \propto \sum_{E-\Delta E/2}^{E+\Delta E/2} |\Psi_i(E, r)|^2. \quad (1.1)$$

Here, Ψ_i is a single-particle wave function at energy E as a function of position r and ΔE is the energy resolution of the experiment. Indeed, many physical properties, which are useful for understanding and developing nanodevices, can be deduced from the LDOS. Thus, it appears challenging to measure the LDOS of nanostructures. This can be done by scanning tunneling microscopy and spectroscopy (STM and STS).

STM addresses individual nanostructures as part of an ensemble. Thus, differences between different nanostructures of the same kind can be studied. STS measures the LDOS down to the nanometer scale. Additionally, if the energy resolution of the microscope is better than the energy separation of the single-electron states, single wave-functions can be mapped.

The aim of this work was to measure the single wave-functions of semiconductor and molecular nanostructures. This was achieved on the strain-induced InAs QDs, which were prepared in an ultra-high vacuum (UHV) environment and were directly transferred to the STM system under UHV conditions. Partly this was also achieved on SWCNTs, where single confined states between defects have been identified. These nanotubes samples were prepared under ambient conditions before being transferred to the UHV system. Unfortunately, I was not able to image single wave-functions on chemically prepared nanocrystals so far. Anyhow, I prepared nanocrystals on Au and imaged them with STM under ambient conditions.

The present work is divided as follows:

- Chapter 2 introduces STM, atomic force microscopy (AFM), and explains how to interpret the measured data.

In the next chapters STM and AFM are used to analyze three kinds of nanostructures.

- Chapter 3 deals with strain-induced InAs QDs, which are grown by MBE.
- Chapter 4 deals with InAs, InP, and CdSe nanocrystals, which are synthesized by colloidal chemical methods.
- Chapter 5 deals with SWCNTs, which are produced by laser evaporation.

Each of the chapters 3 to 5 provides a literature survey of the nanomaterial studied, explains the experiment, presents the experimental results, and includes an analysis of the data.

- Chapter 6 summarizes all results from chapters 3, 4, and 5 and gives an outlook for future experiments.

Chapter 2

Scanning probe methods

2.1 Scanning tunneling microscopy and spectroscopy

Scanning tunneling microscopy (STM) can image conductive surfaces with atomic resolution. Additional to the imaging of the surface topography, scanning tunneling spectroscopy (STS) can obtain spatially resolved spectroscopic information. Thus, topography and spectroscopy can be directly related.

Section 2.1.1 summarizes the basic functions of a STM instrument. In section 2.1.2 the theoretical basis of STS is introduced, which is necessary to understand spectroscopic data. An extensive introduction to scanning tunneling microscopy and spectroscopy, however, can be found in references [15–17]. Finally, the low temperature UHV STM, which was mainly used in this work, is described in section 2.1.3.

2.1.1 Principle

The basic components of STM are a metallic, atomically sharp tip and a conductive sample with a preferably smooth surface. A voltage V_{sample} is applied between tip and sample. This creates a measurable tunneling current at a tip-sample separation of about 4–7 Å. This tunneling current is kept constant by means of a feedback loop. The output signal of the feedback loop adjusts the vertical z -position of the tip in order to achieve constant-current while a lateral (x, y) scanning is performed. The z -position of the tip as a function of (x, y) is displayed. The resulting constant-current image can be interpreted in a first approximation as the topography of the sample. This so-called constant-current mode is exclusively used in this work.

The x , y , and z scanning of the tip is made by piezo elements, which allow tip positioning with high accuracy in all three directions. Note, that the tunneling current depends exponentially on the tip-surface distance. Thus, atoms further away from the sample as well as tip surfaces do not contribute much to the tunneling current. Therefore, a high lateral resolution down to the atomic scale is obtained with STM.

2.1.2 Theory

In a first approximation, the electron tunneling between tip and sample can be described within a one-dimensional model. The simple case of single-electron tunneling through a rectangular one-dimensional potential barrier is calculated in several quantum mechanics textbooks (e.g. [18]) and PhD theses (e.g. [19–21]). The resulting transmission coefficient T is:

$$T \approx \frac{16k^2\kappa^2}{(k^2 + \kappa^2)^2} \cdot e^{-2\kappa z} \quad (2.1)$$

where k is the wave vector of the electron, z the barrier width (tip-sample distance), and κ is given by:

$$\kappa = \sqrt{2m(V_0 - E)/\hbar^2}. \quad (2.2)$$

Here, m is the effective mass of the electron and $V_0 - E$ is the effective barrier height for an electron with energy E . The expected exponential z -dependence of the tunneling current is evident.

However, this simple one-dimensional model is not sufficient to describe electron tunneling between a three-dimensional tip and a three-dimensional substrate. Bardeen gave a more detailed model in 1961 [22]. He considered time-dependent tunneling between two metallic layers through a sufficiently high barrier. Therefore, the time-dependent Schrödinger equation is solved based on a perturbation approach. First, the single-particle wave functions ψ_μ^t and ψ_ν^s for the separated and independent metallic layers are considered with their eigenvalues E_μ^t and E_ν^s . Note, that Bardeen performed the original calculations for tunneling between two general layers. The labels t and s for tip and sample are used here because of the application to STM later on. Within Bardeen's formalism, the tunneling current I_t can be evaluated to:

$$I_t = \frac{2\pi e}{\hbar} \sum_{\mu,\nu} \{f(E_\mu^t)[1 - f(E_\nu^s + eV)] - f(E_\nu^s + eV)[1 - f(E_\mu^t)]\} \cdot |M_{\mu\nu}|^2 \cdot \delta(E_\nu^s - E_\mu^t). \quad (2.3)$$

$M_{\mu\nu}$ is the tunneling matrix element between the unperturbed electronic states ψ_μ^t of the tip and ψ_ν^s of the sample surface, V is the applied sample-voltage, and f represents the Fermi-Dirac distribution. Since only elastic tunneling is considered, a delta function is found in the equation (energy conservation). According to Bardeen [22], the tunneling matrix element is given by:

$$M_{\mu\nu} = -\frac{\hbar^2}{2m} \int [(\psi_\mu^t)^* \nabla \psi_\nu^s - \psi_\nu^s \nabla (\psi_\mu^t)^*] d\vec{S}. \quad (2.4)$$

Tersoff and Hamann applied Bardeen's theory to STM and analyzed the tunneling current between tip and surface [23, 24]. For $T = 0$ K, the Fermi function is given by:

$$f(E) = \begin{cases} 0 & \text{for } E > E_F \\ 1 & \text{for } E < E_F \end{cases} \quad (2.5)$$

where E_F is the Fermi energy. For small applied voltages, equation 2.3 reduces to:

$$I_t = \frac{2\pi e^2 V}{\hbar} \sum_{\mu, \nu} |M_{\mu\nu}|^2 \delta(E_\nu^s - E_F) \delta(E_\mu^t - E_F). \quad (2.6)$$

In general, the tunneling matrix is difficult to calculate. For a point-shaped tip at position \vec{r}_0 , however, equation 2.6 reduces to:

$$I_t \propto V \sum_{\nu} |\psi_\nu^s(\vec{r}_0)|^2 \delta(E_\nu^s - E_F). \quad (2.7)$$

Here, $\sum_{\nu} |\psi_\nu^s(\vec{r}_0)|^2 \delta(E_\nu^s - E_F)$ is the LDOS at the Fermi energy and at the tip position \vec{r}_0 . Since a single point is a poor model for a real tip, Tersoff and Hamann presumed a spherical tip shape with radius R centered at \vec{r}_0 as is shown in Fig. 2.1.

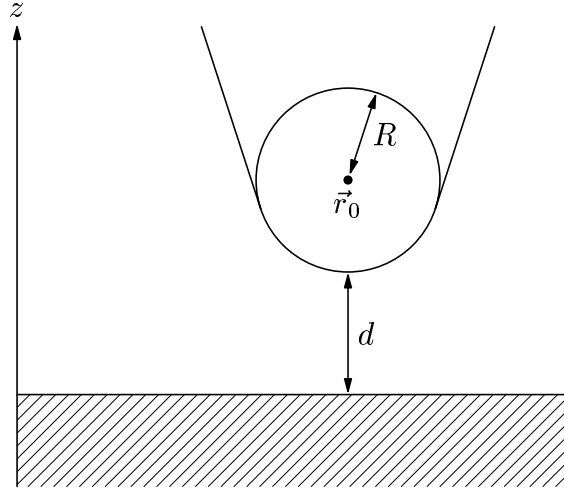


Figure 2.1: Shape of the STM tip in the Tersoff-Hamann model. Tip radius R at \vec{r}_0 and tip-sample distance d are marked in the figure (taken from [19] according to [23]).

Additionally, a spherical s-orbital at the tip end is assumed in the calculations. This leads to:

$$I_t \propto V \rho_t(E_F) e^{2\kappa R} \sum_{\nu} |\psi_\nu^s(\vec{r}_0)|^2 \delta(E_\nu^s - E_F) = V e^{2\kappa R} \rho_t(E_F) \rho_s(\vec{r}_0, E_F) \quad (2.8)$$

with $\rho_t(E_F)$ being the LDOS of the tip at the Fermi energy and $\rho_s(\vec{r}_0, E_F)$ the LDOS of the sample at the Fermi energy and tip position \vec{r}_0 (see Fig. 2.1). The decay rate κ is given by equation 2.2. Note, that equation 2.8 holds only for small sample-voltages V . If V is increased, the voltage dependence of the tip and sample LDOS has to be considered and the tunneling current is an integral over energy:

$$I_t \propto \int_0^{eV} \rho_t(E - eV) \cdot \rho_s(\vec{r}_0, E) dE. \quad (2.9)$$

The sample density of states $\rho_s(\vec{r}_0, E)$ at \vec{r}_0 is related to the LDOS of the sample $\rho_s(x, y, z = 0, E)$ via the relation:

$$\rho_s(\vec{r}_0, E) = \rho_s(x, y, z = 0, E) \cdot T(E, eV, z = d + R) \quad (2.10)$$

with $T(E, eV, z = d + R)$ being the transmission coefficient. T can be estimated using the WKB method for the tunnel barrier to:

$$T(E, eV, z) = e^{-2z[\frac{2m}{\hbar^2}(\frac{\Phi_t + \Phi_s}{2} + \frac{eV}{2} - E)]^{1/2}} \quad (2.11)$$

with Φ_t and Φ_s being the work functions of tip and sample, respectively. This leads to the following expression for the tunneling current:

$$I_t(x, y, V) \propto \int_0^{eV} \rho_t(E - eV) \cdot \rho_s(x, y, E) \cdot T(E, eV, z) dE. \quad (2.12)$$

This situation is visualized in Fig. 2.2. For negative sample-voltages, the electrons tunnel from occupied states of the sample into unoccupied states of the tip, whereas at positive sample-voltage, the electrons tunnel from occupied states of the tip into unoccupied states of the sample.

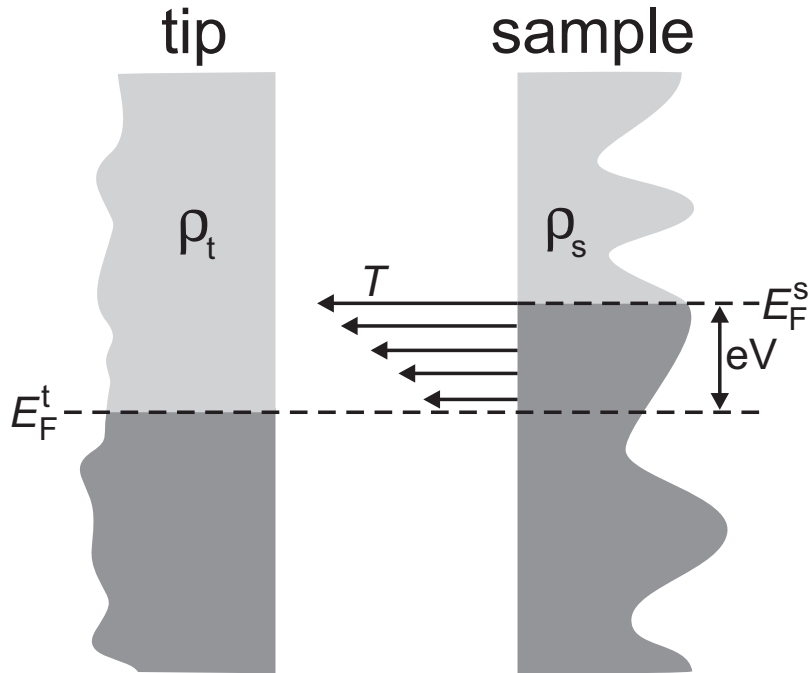


Figure 2.2: Electron tunneling from sample to tip. The applied voltage V shifts the Fermi energy by a value of eV . Occupied states are dark gray, unoccupied states light gray. The transmission coefficient T increases with increasing energy as indicated by the arrows.

The important quantity is $\rho_s(x, y, E)$: The LDOS of the sample as a function of position and energy. A direct access to $\rho_s(x, y, E)$ can be obtained by differentiating equation 2.12:

$$\begin{aligned} \frac{dI_t}{dV}(x, y, V) &\propto e \cdot \rho_t(0) \cdot \rho_s(x, y, E = eV) \cdot T(E = eV, eV, z) \\ &+ \int_0^{eV} \rho_t(E - eV) \cdot \rho_s(x, y, E) \cdot \frac{dT(E, eV, z)}{dV} dE \\ &+ \int_0^{eV} \frac{d\rho_t(E - eV)}{dV} \cdot \rho_s(x, y, E) \cdot T(E, eV, z) dE . \end{aligned} \quad (2.13)$$

The LDOS of the tip ρ_t is usually considered to be energy independent. Thus, the third term is neglected. At voltages lower than 200 mV, the second term is less than 10% of the first term [25]. Thus, the second term can be neglected at low voltages. In section 3.3, however, STS at voltages up to 1.8 V is performed. The justification, that the second term is still negligible will be given there.

Consequently, for established situations in STM and STS only the first term is dominant:

$$\frac{dI_t}{dV}(x, y, V) \propto \rho_s(x, y, E = eV) \cdot T(E = eV, eV, z). \quad (2.14)$$

The general conclusion is that dI/dV is proportional to the LDOS of the sample concerning the position dependence (x, y) and also basically proportional to the energy dependence of T . The so-called lock-in technique enables a direct access to dI/dV by adding a small amplitude high-frequency modulation voltage V_{mod} to the sample voltage V . Thus, the dI/dV signal can be measured with high accuracy in addition to I .

Electronic states in nanostructures are measured in this thesis with STS. Therefore, advantage is taken from equation 2.14. With dI/dV versus V data measured spatially resolved over the nanostructures maps of the LDOS are obtained. If, for example, the LDOS exhibits delta-function like single-electron states, peaks should be visible in dI/dV versus V curves.

2.1.3 Low temperature UHV STM

Two low temperature UHV STMs are used in this work. One of them is used for the measurements shown in chapter 5 and is described in [26]. The other one is presented here paradigmatic for a low temperature UHV STM. Most measurements in chapters 3 and 4 are done with this microscope. However, a more detailed description can be found in [27].

The complete 6 K UHV STM system is home built [20, 21]. It has an energy resolution down to 2 meV and a drift stability of 3 Å/h. A front and top view of the whole vacuum system is shown in Figs. 2.3 and 2.4, respectively. Three vacuum chambers and a cryostat can be recognized. The pressure in the room temperature UHV chambers is 10^{-10} mbar. In the low temperature chamber the cryostat acts as a liquid helium cold trap. Thus, the pressure is $\ll 10^{-10}$ mbar there.

In order to achieve UHV, the chambers are pumped down with a turbo molecular pump. Afterwards, a bake out is done for three or four days at a maximum temperature of 150°C. Note, that higher temperatures can damage the piezo elements of the STM. After bake out the ion pumps are switched on and the turbo pump is decoupled and switched off. Additionally, each chamber has its own Ti sublimation pump.

The vacuum chamber on the left has a load lock for passing samples into the vacuum system (Fig. 2.4). In the present work a vacuum transfer system between a MBE and this STM is build up. It is described in detail in section 3.2. The mobile vacuum transfer system and the docking position are marked in Fig. 2.4. An electron beam heater and an O₂ inlet are used for preparation of a tungsten single-crystal, which is used for tip preparation. Tip preparation includes short pulsing (5 msec, up to 30 V) and field emission (150 V at 10 μA). The tip is even sometimes dipped deliberately into the W substrate (1–5 walker steps, see below) and laterally moved up to 400 nm. These three preparation procedures are found to be sufficient in order to prepare tips, which yield high-quality topographic and spectroscopic data of the nanostructures studied in this work.

The vacuum chamber on the right has an Fe evaporator, a LEED/AUGER unit, and a resistance heater. However, this chamber is not used in the present work.

Samples can be transferred between the chambers by UHV manipulators and inserted into the STM. The STM is attached to a two meter long rod, which can be moved up and down with a z-manipulator, consisting of a motor and a UHV bellow. In upper position the STM is in the center of the middle chamber and the sample can be inserted or exchanged. When the STM is moved downwards into the cryostat, the rod is automatically decoupled from the STM in order to avoid mechanical vibrations.

Several other techniques are used to decouple external vibrations from the STM. The sand bath, shown in Fig. 2.3, is the main vibration isolation. Additionally, the complete system is mounted on four damping legs with passive air damping and the foundation of the system is decoupled from the rest of the building. The complete equipment is made very heavy and, thus, insensitive against high-frequent vibrations.

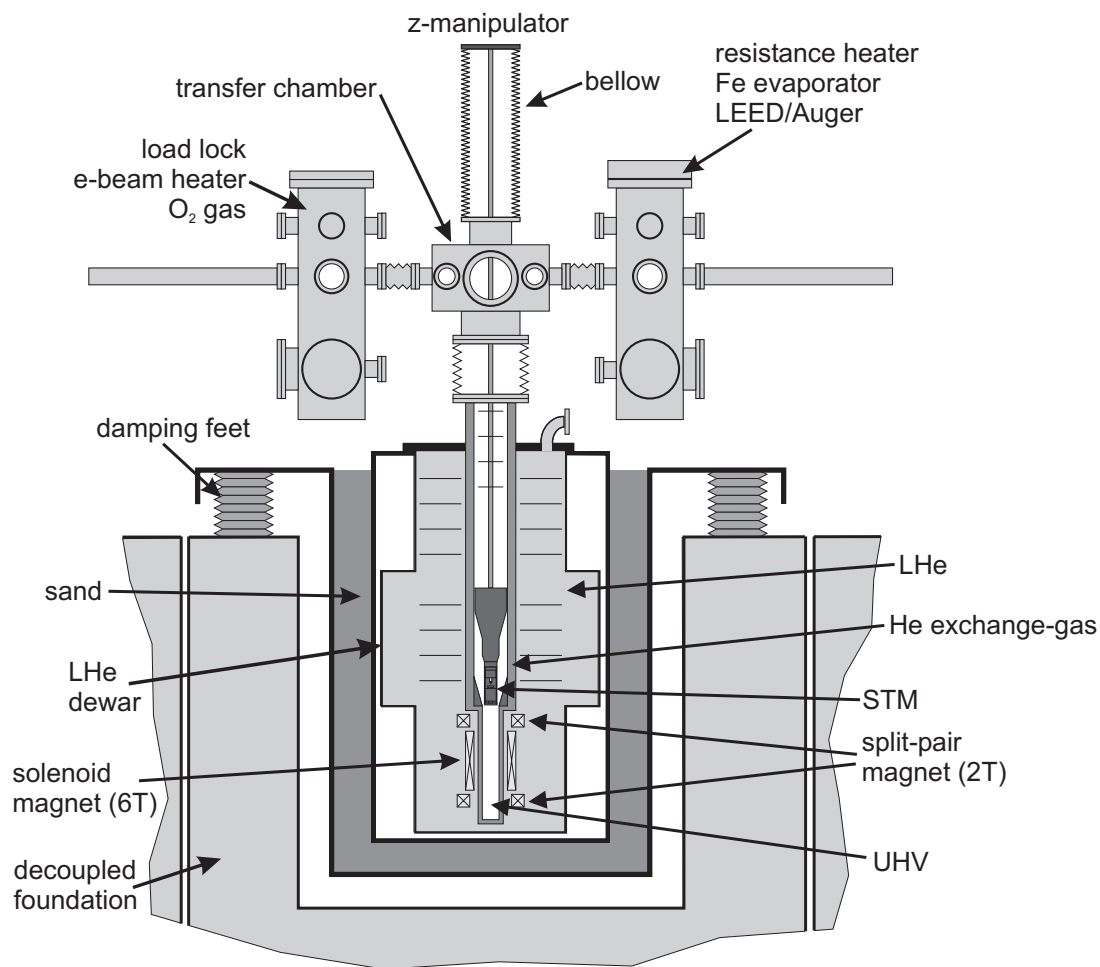


Figure 2.3: Front view of the 6K UHV system (taken from [28]).

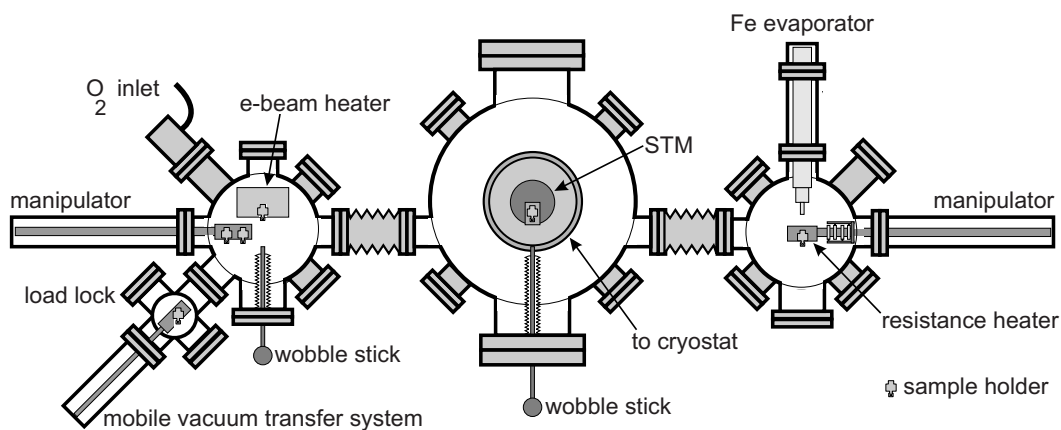


Figure 2.4: Top view of the 6 K UHV system (taken from [28]).

The STM is located in the cryostat during measurements. The cryostat has a dewar with a capacity of 100 liters of liquid He (LHe). Thermal super insulation of the dewar is obtained with an outer vacuum. While the STM is in UHV the thermal contact with the LHe bath is made by an exchange gas (Fig. 2.3). This is done for a better vibration isolation from the boiling LHe. The STM keeps a temperature of 6.5 K for about 72 h without refilling LHe. Thus, 72 h is the maximum duration for a single measurement.

Two super-conducting magnets are placed in the LHe bath. A solenoid produces a magnetic field up to 6 T perpendicular to the sample surface and a split-pair magnet produces a magnetic field up to 2 T parallel to the sample surface. However, the magnets are not used in the present work.

Figure 2.5 shows the STM and the walker system. The positions of the scanner, tip, sample holder, and walker are marked in (a). A system to exchange the tip *in situ* is in preparation but not used in this work. Therefore, the vacuum system must be opened to exchange the tip but not to exchange the sample.

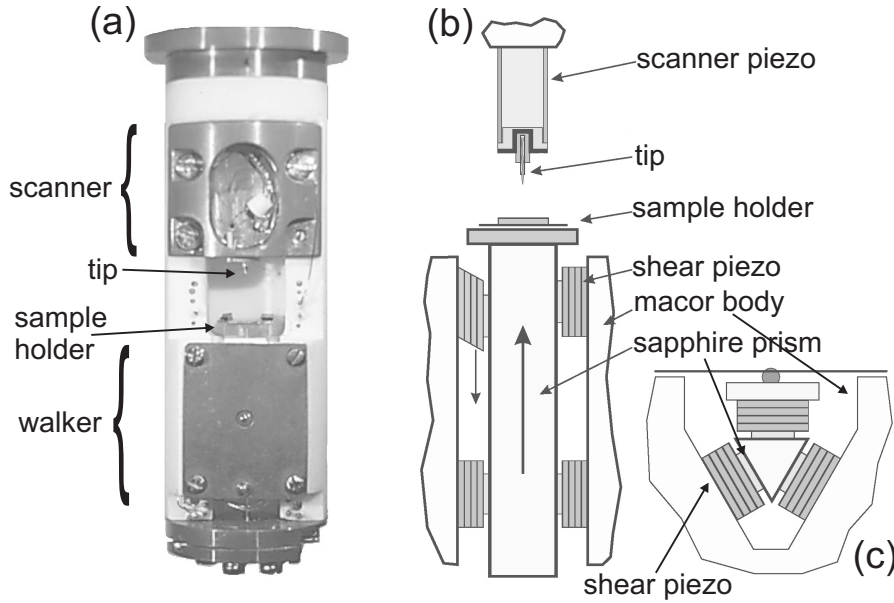


Figure 2.5: (a) Photo of the STM. (b) Sketch of the STM. (c) Cross section through the walker. Pictures are taken from [20].

During a sample exchange with the wobble stick, the tip-sample distance is about 1–2 mm. Afterwards, the sample is approached towards the tip by a stepwise movement of the walker. The design of the walker is shown in Figs. 2.5(b) and (c). A sapphire prism is held by six shear piezos. One after the other they shear along the prism, while the other five keep the prism in position. After all piezos have moved, they move back concurrently, bringing the prism with the sample one step towards the tip. One walker step is about 100–200 nm long. First, a rough manual approach with 50 steps/sec is made down to a tip-sample distance of about 50–100 μm . The

rough approach is controlled with an optical microscope. Finally, the computer controls the fine approach at 1 step per 3 seconds. Before performing each step the tip-sample distance is checked by extending the piezo scanner slowly. If a tunneling current is detected, the tip is close enough to the sample and no further walker steps are required.

The measurements are controlled by a feedback system, a data acquisition system (TOP System II), and a computer. The feedback hardware and the software have been developed at the University of Hamburg [20,21]. The commercial TOP System II controls the measurements, collects the data, and acts as high-voltage amplifier. At the computer the user can control the measurement and handle the recorded data.

2.2 Atomic force microscopy

Atomic force microscopy (AFM) is another scanning probe technique with atomic resolution in UHV. In contrast to STM, AFM works also on insulating samples. In air, for example, Au on mica and highly oriented pyrolytic graphite (HOPG) are reproducibly imaged with STM, but even a native oxide layer on a n-doped semiconducting sample reduces the imaging quality.

Commercial air AFMs (D3000 and Nanoscope IIIa, Digital Instruments) are used in this work to characterize the nanostructures. Since STM is the main topic of this thesis, only a brief introduction to AFM should be given here. A detailed introduction to AFM can be found in [15] and a recent overview article can be found in [29].

In the case of AFM, the force between tip and sample replaces the current between tip and sample measured with STM. Therefore a force sensor is required. The force sensor in AFM is a cantilever with a sharp tip at one end. A photo and a top/side view of a cantilever is shown in Figs. 2.6(a) and (b), respectively. It has a width w , thickness t , and length L as indicated in (b).

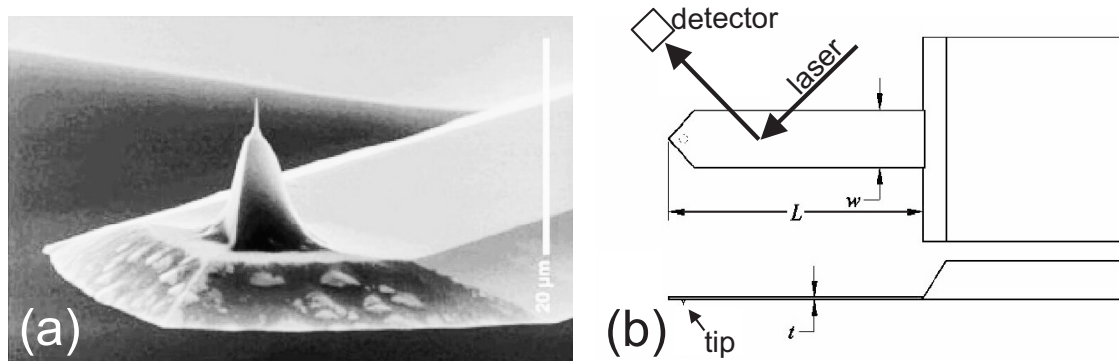


Figure 2.6: (a) Photo of a micro-fabricated cantilever with an integrated tip (made by Nanosensors). (b) Top view and side view of a cantilever (dimensions w , t , L , and the laser path are marked). Pictures are taken from [29].

The most common technique nowadays to measure the cantilever displacement in air AFMs is the laser beam deflection. The cantilever displacement is measured by detecting the deflection of the laser beam, which is reflected off the rear side of the cantilever. The direction and magnitude of the reflected laser beam is sensed with a position sensitive detector. The laser path is shown schematically in Fig. 2.6(b).

Two AFM modes are used in this thesis: Contact and tapping mode AFM.

In contact AFM the tip is in permanent "contact" with the surface. The repulsive forces between tip and sample can be measured due to the deflection of the cantilever described above. The scanning is performed in the so-called constant-force mode (analogous to the constant-current mode in STM). The condition of constant-force is achieved by keeping the cantilever deflection constant by means of a feedback loop. The output signal of the feedback loop adjusts the vertical z -position of the sample in order to achieve a constant cantilever deflection (constant-force) during scanning. The resulting constant-force images are interpreted as topography (analogous to the constant-current images in STM). In this thesis, Nanosensors contact cantilevers are used ($L=226 \mu\text{m}$, $w=26\text{--}27 \mu\text{m}$, $t=1.6 \mu\text{m}$, with a resonant frequency $f=71\text{--}85 \text{ kHz}$, and a spring constant $k=2\text{--}3.6 \text{ N/m}$).

If conductive AFM tips are used, spatially resolved conductance images can be obtained in addition to the constant-force topography. This AFM mode is called conductive AFM. The mode where capacitance is measured simultaneously to topography (with a capacitance bridge) is called scanning capacitance microscopy (SCM).

A further mode available in commercial AFMs from Digital Instruments is the so-called "tapping mode". Tapping mode (tm) is a dynamic AFM mode. The cantilever oscillates at or near its resonant frequency and "taps" the surface at the lower reversal point. The oscillation amplitude is used for the feedback control. Thus, constant-amplitude images are interpreted as topography in tmAFM. In this thesis, Nanosensors non-contact cantilevers are used ($L=225 \mu\text{m}$, $w=34\text{--}37 \mu\text{m}$, $t=10\text{--}15 \mu\text{m}$, with a resonant frequency of $f=181\text{--}209 \text{ kHz}$, and a spring constant of $k=40\text{--}64 \text{ N/m}$). The in-plane forces, which are present in contact AFM, are strongly reduced in tmAFM. This AFM mode is preferable, if the nanostructures are not strongly bound to the surface. Contact AFM (and even STM) can push loosely bound nanostructures away during scanning. This tip-induced mobility is strongly reduced in the case of tmAFM.

Chapter 3

InAs quantum dots

This chapter deals with strain-induced InAs QDs grown on GaAs(001) by MBE and studied with low temperature UHV STM and AFM under ambient conditions. The InAs QDs are grown by Arne Bolz and Dr. Christian Heyn in the group of Prof. Dr. Wolfgang Hansen (Institute of Applied Physics, University of Hamburg, Germany). Section 3.1 gives a short introduction to strain-induced InAs QDs and a literature survey on related experiments. In section 3.2 the sample preparation is explained and band calculations motivate the chosen sample geometry. In section 3.3, wavefunction mapping of the QD single-electron states is shown measured with STS. Finally, the influence of an oxide layer is studied in air by conductive AFM (section 3.4) and SCM (section 3.5).

3.1 Basic properties

Strain-induced InAs QDs are grown in UHV with molecular beam epitaxy (MBE) on GaAs(001) as described in [30]. Due to the lattice mismatch between InAs and GaAs of 7.16% a dot formation is energetically more favorable than layer-by-layer growth. First, a so-called wetting layer (WL) is formed, then, the pyramidal-shaped InAs QDs appear. This growth mode is named Stranski-Krastanov growth.

In situ STM measurements on freestanding InAs QDs with atomic resolution have been reported in [31]. Figure 3.1(a) demonstrates a 3D image of a pyramidal shaped InAs QD with atomic resolution. It appears elongated in $[110]$ direction. This shape asymmetry is better visible in the two linescans in $[1\bar{1}0]$ and $[110]$ direction shown in (b). A detailed analysis identified the facets of the QDs, which are indicated in a model shown in (c). It should be noted, however, that a similar STM study demonstrate QDs, which were elongated in the $[1\bar{1}0]$ direction [32]. Thus, the elongation is growth dependent.

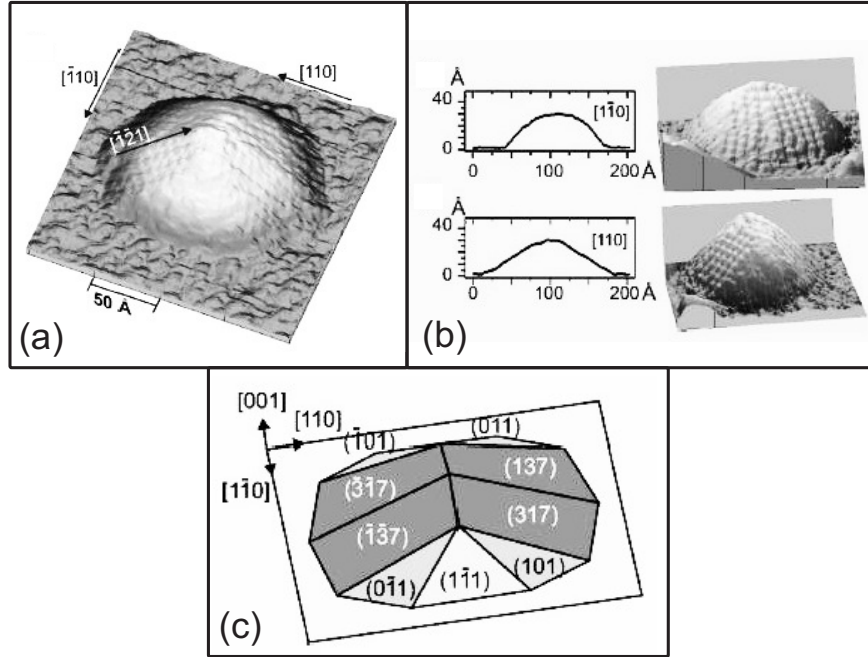


Figure 3.1: (a) Atomically resolved 3D STM image of an InAs QD on GaAs(001). (b) QDs appear elongated in $[110]$ direction (shape asymmetry). (c) Model of the facets found in atomically resolved images. All data are taken from [31].

In these experiments, high-resolution topographic information of the QDs was achieved but there is no information about the electronic structure of the dots. The following experiment is the opposite. Magnetotunneling spectroscopy is used to measure the electronic states of overgrown InAs QDs on GaAs(311)B [33]. This is shown in Fig. 3.2. The differential conductance G is measured vertical through an ensemble of embedded QDs at different voltages (e_2 , e_4 , and e_7). Additionally, a magnetic field is applied perpendicular to the current direction and the change in G is recorded. $G(B)$ data are shown in Fig. 3.2 (b). The differential conductance is measured at certain increasing energies (e_2 , e_4 , and e_7) and as a function of a magnetic field, which is applied parallel to the $[01\bar{1}]$ direction. Thus, the tunneling electrons are accelerated in the $[\bar{2}33]$ direction. In the tunneling process the electron picks up a \vec{k} component parallel to the interface and, therefore, probes the corresponding \vec{k} distribution of the QD state. If the procedure is done for all directions in the surface plane, one can obtain the complete squared wave functions as shown in (a). In energetic sequence, (000), (100), and (200) states are found, where the numbers describe the number of nodes in $[\bar{2}33]$, $[01\bar{1}]$, and $[311]$ direction, respectively. Surprisingly, the (010) state is missing although the (200) state appears. The reason could not be clarified in this experiment. For embedded InAs QDs on GaAs(001) the individually probed wave functions are less well resolved. A spherical (000) state and an approximately toroidal higher state are only weakly concluded in [34].

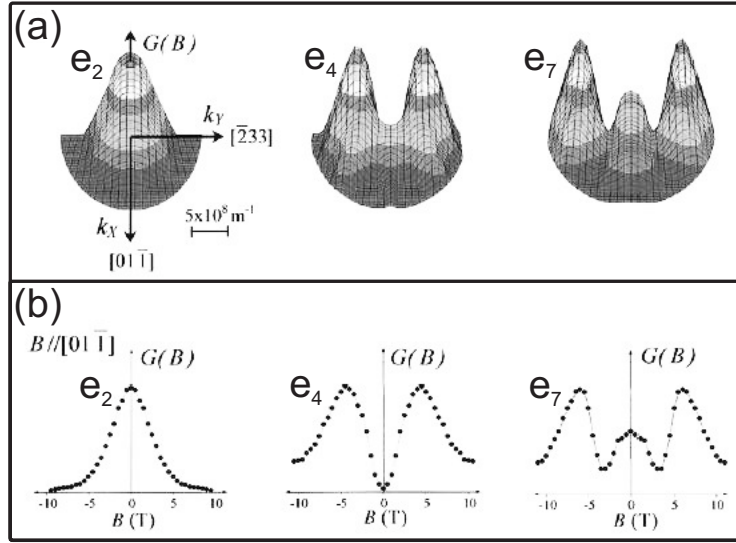


Figure 3.2: (a) Wave-function mapping at different energies (e_2 , e_4 , and e_7). (b) Linescans demonstrate the nodes in the wave functions. All data are taken from [33].

Evidence for wave-function mapping in single QDs has been demonstrated by cross-section STM [35]. The results are presented in Fig. 3.3: A cross-section STM image of the InAs QDs grown on GaAs(001) is shown in (a). The inset shows the sample and tip geometry of this experiment. It is obvious that only a part of the complete wave function can be imaged in cross-section STM. They are shown in the current images (b) and (c) which are obtained at $V_{\text{sample}}=0.69$ and 0.82 V, respectively. In (b) a pure s-state is visible while in (c) an overlap between s- and p-state is found. This overlap originates from the current measurement. At 0.82 V both the s-state and the p-state contribute to the current and, thus, an overlap is measured.

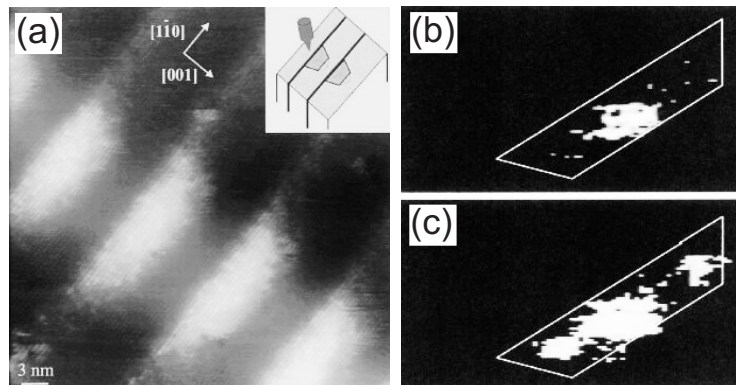


Figure 3.3: (a) STM image of embedded InAs QDs; inset: sample and tip geometry. (b) and (c) Current images at $V_{\text{sample}}=0.69$ and 0.82 V, respectively. All data are taken from [35].

With the so-called 8-band $k \cdot p$ theory it is possible to calculate energies and wave functions of QDs [36] including strain, which is present in the dots due to the lattice mismatch between InAs and GaAs. Calculated wave functions for symmetrical InAs QDs on GaAs(001) are shown in Fig. 3.4. The shapes of the measured wave functions in Fig. 3.2(a) are in reasonable agreement to the calculated (000), (100), and (200) states. One important result of the theoretical study is that the (100) and the (010) states form a nondegenerate pair. Nevertheless, the (010) state appears between (100) and (200).

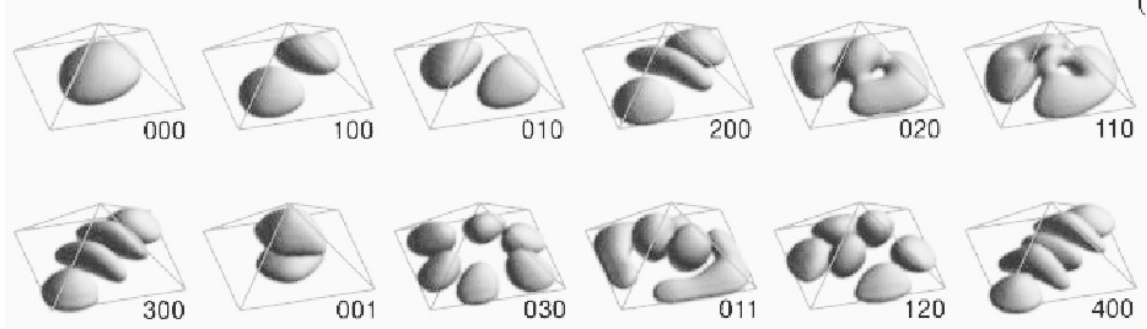


Figure 3.4: Calculated wave functions for symmetrical InAs QDs on GaAs(001) with a base width of 20.4 nm (taken from [36]). The numbers describe the number of nodes in $[110]$, $[1\bar{1}0]$, and $[001]$ direction, respectively.

The main aim of this work is to measure the shape, the electronic states, and the corresponding wave functions of InAs QDs grown on GaAs(001). STM is used for topographic information, STS is used for spectroscopic information, and spatially resolved STS is used for wave-function mapping of freestanding and single InAs QDs. The local probing of individual QDs can reveal differences between them. This and a comparison between our data and theory are presented in section 3.3. The influence of an oxide layer on the same sample is analyzed with conductive AFM in section 3.4 and with SCM in section 3.5. At first, however, section 3.2 explains the sample preparation and establishes the chosen sample geometry.

3.2 Sample preparation

Strain-induced InAs QDs are usually grown on relatively large GaAs wafers by MBE in UHV. The UHV STM (explained in 2.1.3), in contrast, takes up much smaller sample holders. It is reported in section 3.3 that an air based transfer between MBE and STM does not allow wave-function mapping. Additionally, section 3.4 and 3.5 will show a strong influence of an oxide layer on the surface properties. Thus, a vacuum transfer between MBE and STM is necessary.

The complete experimental setup is shown in Fig. 3.5. The MBE system is shown in (a). The growth chamber is located below the monitor and the load lock is on the right hand side. In order to grow QDs for the STM experiment, small pieces are cut from a full GaAs(001) wafer ($N_D=2\times 10^{18}\text{cm}^{-3}$) and glued with a liquid In droplet on the STM sample holders, which are shown in the inset. Inside the MBE a transport system allows growth and subsequently transfer of the sample from the growth chamber to the load lock. In order to transfer the samples from the MBE load lock to the STM system, a mobile UHV transfer system, shown in (b), is built up. It has a battery driven ion getter pump, a suitable long wobble stick, and a vacuum valve in order to connect to and disconnect from the UHV systems. A connection to the MBE load lock is shown in (c). The sample can be pulled out from the MBE with the wobble stick. Then the transfer chamber is disconnected and moved to the STM

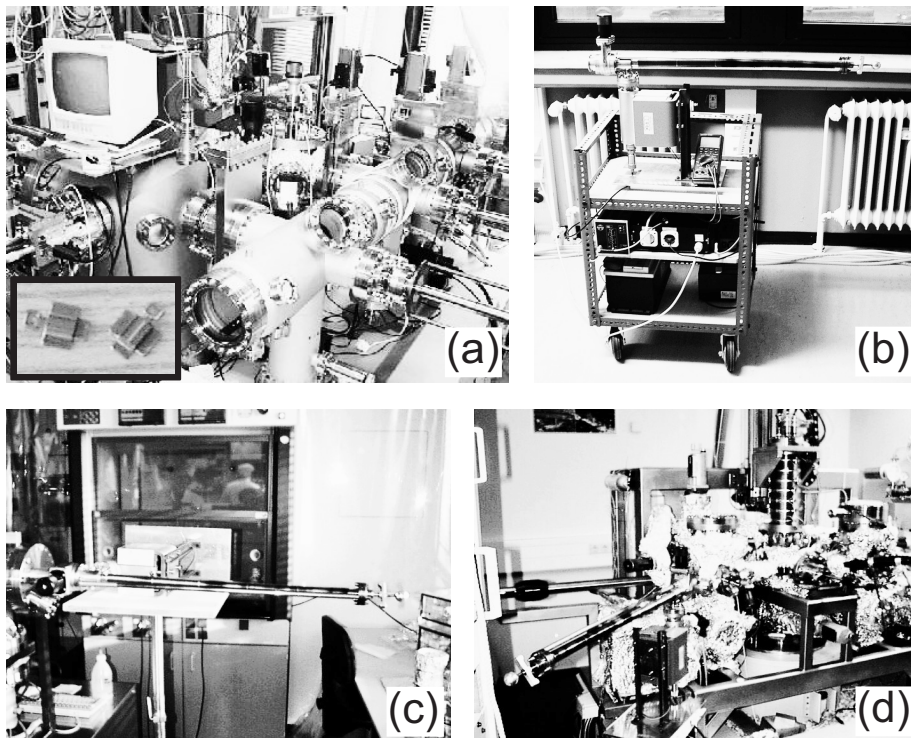


Figure 3.5: (a) Photo of the MBE; inset: photo of the STM sample holders. (b), (c), and (d) Photo of the mobile vacuum transfer system alone, connected to the MBE, and connected to the 6 K UHV STM, respectively.

system without breaking the UHV. There, it is connected as shown in (d) and the sample is pushed into the STM system. During the approximately 1 h transfer time the pressure is always $<10^{-9}$ mbar. Thus, a UHV transfer is realized between two UHV chambers, which are located in different laboratories within the same institute.

In test experiments the topography of the QDs on the smaller STM sample holders are determined using contact AFM in air after removing the samples from UHV. The following growth parameters are found to create relatively high InAs QDs with a large number of confined states: n-doped GaAs(001) ($N_D=2\times 10^{18}\text{cm}^{-3}$) is first overgrown with a 400 nm thick n-doped buffer layer ($N_D=2\times 10^{18}\text{cm}^{-3}$) of GaAs at $T = 600^\circ\text{C}$. Afterwards, a 15 nm thick GaAs tunneling barrier ($N_A < 1 \times 10^{15}\text{cm}^{-3}$) is grown. The reason for this tunneling barrier is explained in the next paragraphs. Finally, two monolayers of InAs are deposited at $T = 495^\circ\text{C}$ in order to form the QDs. This growth is done in a Riber MBE (Fig. 3.5(a)) at a base pressure $<4\times 10^{-11}$ mbar by Arne Bolz [37].

A sketch of the QD sample including STM tip and current path z is shown in Fig. 3.6. The tunneling barrier decouples the single-electron states of the QDs from the highly doped GaAs backgate. On the one hand, a thick tunneling barrier decouples the states effectively. On the other hand, a thin barrier allows a stable tunneling current, which should be at least on the order of the tunneling current from the tip to the QD.

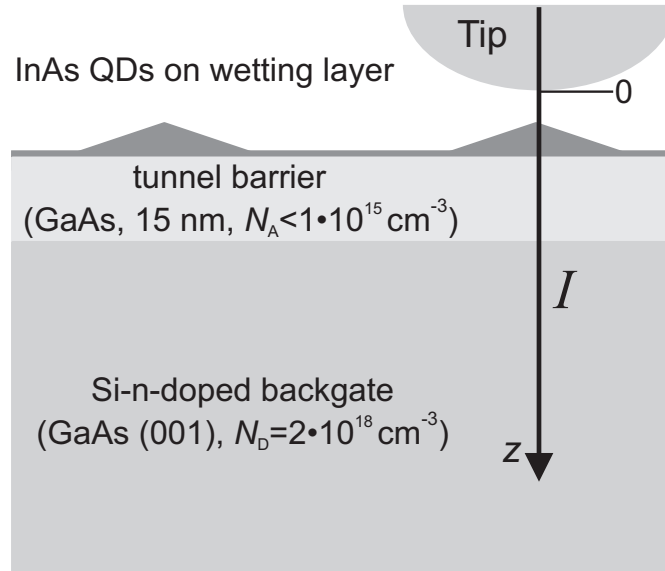


Figure 3.6: Sketch of STM/STS measurement of the sample with freestanding InAs QDs (tunneling path I along z is indicated).

In order to find a reasonable thickness, band profile calculations are performed with a freeware 1D-Poisson solver [38,39]. A result of such a calculation is shown in Fig. 3.7. In the z -direction (marked in Fig. 3.6) the tip ends at $z=0$ followed by a vacuum barrier. The work functions of PtIr tips and InAs QDs of about 5.3 eV and 4.9 eV, respectively, are used to estimate the barrier. A QD of height $H=9.4$ nm is used in this calculation. Following a band offset between InAs QD and GaAs, the band bending ends at the backgate, which is degenerately doped (E_F within the conduction band). The calculation is done for a 15 nm thick tunneling barrier. Low temperature material parameters are used in the calculation with the doping concentrations marked in Fig. 3.6. The band offset between InAs QD and GaAs of 390 meV is estimated according to 40% Ga content within the dot. This is reasonable, since grazing incidence x-ray diffraction on an identically grown sample (performed by a method described in [40]) indicate an average Ga content of 33% increasing towards the bottom of the dots [41]. Note, that this calculation is performed assuming Fermi equilibrium between tip and sample ($V_{\text{sample}}=0$ V).

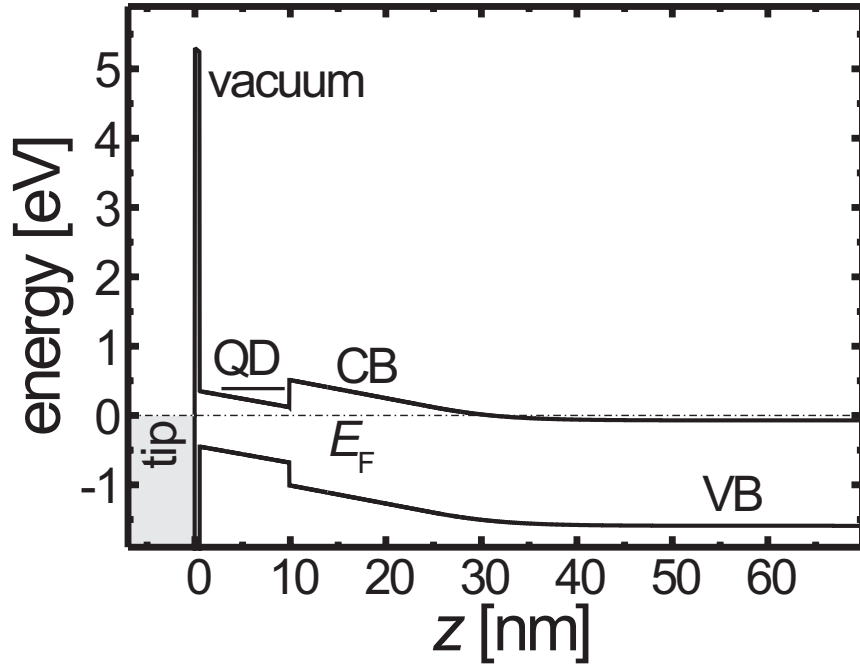


Figure 3.7: Band profile along the z -direction marked in Fig. 3.6 as calculated with a 1D-Poisson solver [38,39]; $V_{\text{sample}}=0$ V, CB: conduction band, VB: valence band; a confined CB state is marked as a full line.

An additional voltage, which is necessary for STM and STS, induces an additional band bending in the semiconducting sample. This is demonstrated in Fig. 3.8. The black curves show the band profile at the QD region for $V_{\text{sample}}=0$ V (zoom of Fig. 3.7). The gray curves show the band profile for $V_{\text{sample}}=1$ V. A negative tip-voltage (positive sample-voltage) induces an upward band bending.

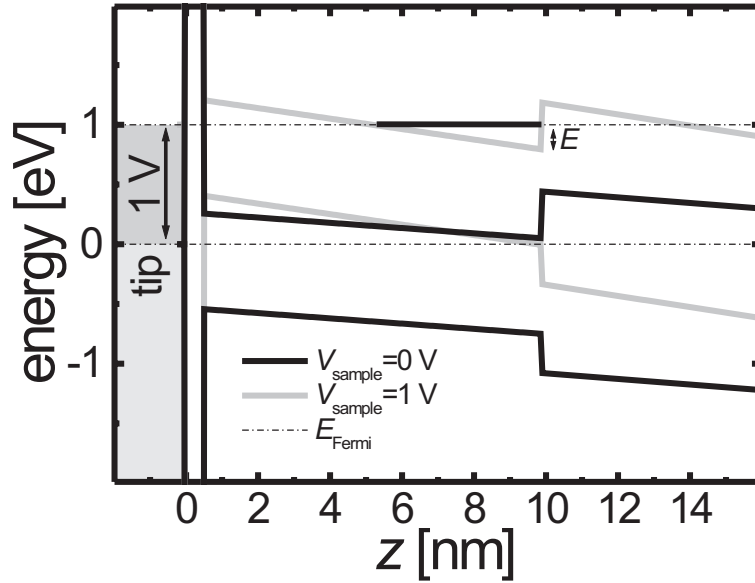


Figure 3.8: Band profile at the QD region for $V_{\text{sample}}=0$ V (black line, zoom of Fig. 3.7) and $V_{\text{sample}}=1$ V (gray line). Negative tip-voltage induces an upward band bending and enables tunneling into the quantized state (marked as a full line).

If the single-electron state of the QD marked in Fig. 3.7 and 3.8 as a solid line is energetically reached by the Fermi level of the tip, a new conduction channel is opened. Sequentially, tunneling can occur from the tip, through the vacuum barrier, to the QD state, and then through the second tunneling barrier into the backgate. For each single-electron state, a new conduction channel is opened. Consequently, steps should appear in $I(V)$ curves at the voltage where the new state is reached. These steps are actually found as demonstrated in section 3.3.

Note, that if tunneling through a single-electron state of the QD starts at 1 V, the energy of the state E (marked in Fig. 3.8) is still much smaller than 1 eV with respect to the conduction band minimum of InAs. Thus, the Poisson calculation can also correct for the influence of the tip-induced band bending. If, for example, resonant tunneling occurs at a certain V_{sample} , the calculation can reconstruct the band bending and, thus, the energy E of the corresponding state with respect to the conduction band minimum.

However, it should be pointed out that these simple 1D-Poisson calculations only estimate the band profile in z -direction and not in the other directions. Additionally, some of the parameters such as work functions of tip and sample or band offsets are not accurately known.

A further advantage of the band-profile calculations is the possibility to estimate the tunneling rate through the second tunneling barrier. The second tunneling barrier in Fig. 3.8 (gray curve) is nearly triangular and has a width of 4 nm and a height of 0.185 eV. The tunneling rate (e_t) for a triangular barrier is [42, 43]:

$$e_t = \frac{eF}{4\sqrt{2m^*\Delta E_t}} \times \exp\left(-\frac{4\sqrt{2m^*\Delta E_t}^{3/2}}{3e\hbar F}\right). \quad (3.1)$$

If we insert:

$$m^*(GaAs) = 0.067 \times m_e \quad \Delta E_t = 0.185\text{V} \times e \quad \text{and} \quad F = \frac{0.185 \text{ V}}{4 \text{ nm}}$$

we get

$$e_t = 1.48 \times 10^{12} \frac{1}{\text{sec}}.$$

Note, that depending on the confined energy of the state and the dot height, tunneling rates up to

$$e_{t,\text{max}} = 3 \times 10^{13} \frac{1}{\text{sec}}$$

are found. The maximum current used in the STS experiment shown in section 3.3 is 100 pA. This corresponds to a tunneling rate from the tip into the QD of $6.25 \times 10^8/\text{sec}$. Since the barriers (vacuum and band offset) are very different, no charging effects should be visible. This is indeed the case as shown in section 3.3.

The intrinsic width of the single-electron states can be estimated from e_t by considering life-time broadening according to $\hbar/2 \approx \Delta E/e_t$. The result is $\Delta E \approx 0.5 \text{ meV}$ for $e_t = 1.48 \times 10^{12}/\text{sec}$ and $\Delta E \approx 10 \text{ meV}$ for $e_{t,\text{max}} = 3 \times 10^{13}/\text{sec}$. This is smaller than the energy separation of the single-electron states of the QD ($\approx 50 \text{ meV}$ [36]). Note, that this estimation is extremely sensitive to the band offset as well as the tip work function which, as mentioned, are not accurately known.

3.3 STS results: Wave-function mapping

The experimental setup presented in section 3.2 is used to grow InAs QDs on GaAs(001) directly on the STM sample holder and to transfer the sample between MBE and STM without breaking the UHV. The 6 K UHV STM is described in section 2.1.3.

A constant-current image of the QD sample is shown in Fig. 3.9(a). Besides the QDs, which are visible as bright spots, several steps appear on the WL. The crystallographic directions are marked in the figure. The QDs appear slightly elongated in $[1\bar{1}0]$ direction. Two dots in the scanning area are considerably larger. The lower right one, for example, is about $60 \times 40 \text{ nm}^2$. Such dots are regularly found on the sample but they do not exhibit any spectral features in STS.

A 3D representation of a typical QD is shown in Fig. 3.9(b). The shape is comparable to previous STM results [31, 32]. Additionally, a superstructure on the WL is visible in the 3D image. This is better shown in (c). The unit cell of $0.93 \times 1.51 \text{ nm}^2$ is marked in the figure. This superstructure is compatible with the (2×4) reconstruction ($0.792 \times 1.584 \text{ nm}^2$; unit cell = $0.396 \times 0.396 \text{ nm}^2$) found previously on the GaAs buffer layer without QDs during growth with reflection high-energy electron diffraction (RHEED).

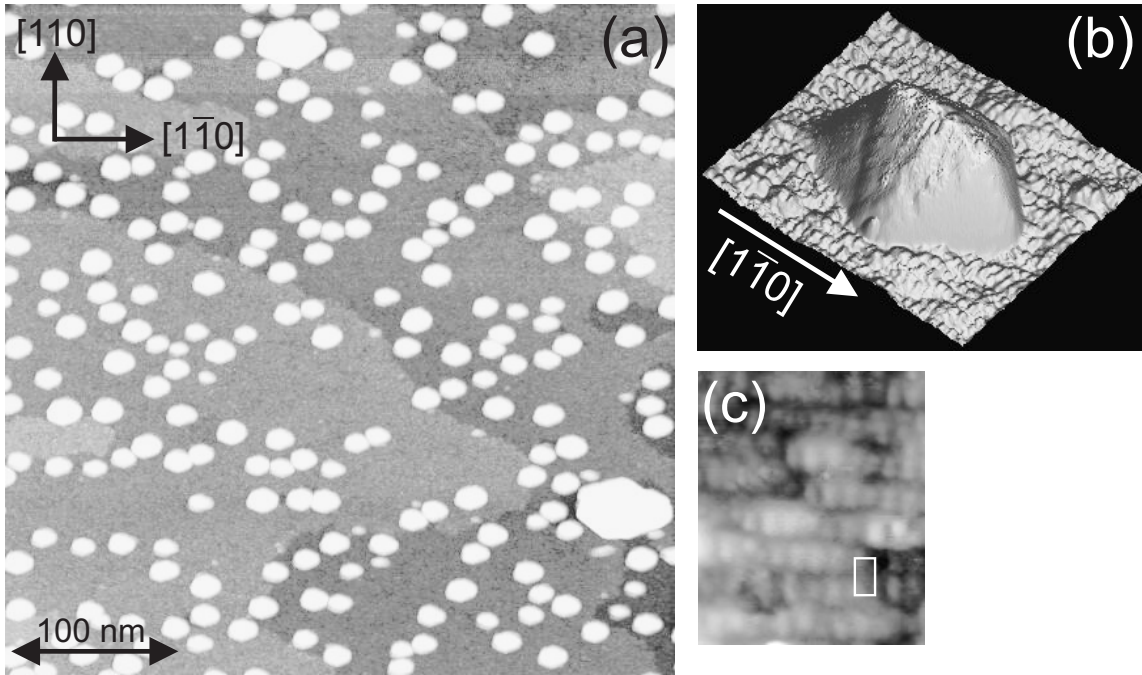


Figure 3.9: (a) Constant-current STM image of the InAs QD sample I ($V_{\text{sample}}=3 \text{ V}$ and $I=70 \text{ pA}$); crystallographic directions are marked in the figure. (b) 3D representation of a typical QD from sample III elongated in $[1\bar{1}0]$ direction. (c) WL on sample III with atomic resolution; (2×4) unit cell is marked (white rectangle).

Altogether, three QD samples were grown by MBE and transferred into the STM system without exposure to air. The only difference is that sample I and II were grown with a 15 nm thick tunnel barrier and sample III with a 20 nm thick one. All QDs studied with STM so far are elongated in $[1\bar{1}0]$ direction. This is demonstrated in the following table (very large dots are not considered any more):

sample I	in $[1\bar{1}0]$ [nm]:	24	19	19	23	22	20	22	18	18	23
	in $[110]$ [nm]:	20	15	16	19	17	17	19	14	14	19
	H [nm]:	9.4	3.4	3.4	8.4	4.1	3.7	4.4	2.7	2.8	4.5
sample II	in $[1\bar{1}0]$ [nm]:	23	21	17	20	22	20	22	26	20	13
	in $[110]$ [nm]:	20	16	15	17	19	16	17	19	14	11
	H [nm]:	5.8	5.0	4.1	4.7	5.9	5.0	5.5	5.7	4.2	1.8
sample III	in $[1\bar{1}0]$ [nm]:	26	28	30	30	25	24	22	20	20	17
	in $[110]$ [nm]:	22	22	21	22	20	17	17	17	13	14
	H [nm]:	3.8	4.8	5.8	4.8	3.8	3.3	3.5	4.3	3.1	1.7

Extensions in the $[1\bar{1}0]$ and $[110]$ directions and the corresponding heights H for different dots are listed. The QDs of sample I have an average extension of 21 ± 2 nm along $[1\bar{1}0]$ and 17 ± 2 nm along $[110]$ and a height of 5 ± 2 nm. The QDs of sample II have an average extension of 20 ± 3 nm along $[1\bar{1}0]$ and 16 ± 3 nm along $[110]$ and a height of 5 ± 1 nm. The QDs of sample III have an average extension of 24 ± 4 nm along $[1\bar{1}0]$ and 19 ± 3 nm along $[110]$ and a height of 4 ± 1 nm.

Note, that the apparent lateral extensions of the dots can depend on the actual tip shape. This is not the case for the dot heights. Anyhow, since the extensions of the QDs are similar on all three samples measured with different tips, it is not likely that the asymmetry of the shape is an artifact of the tip.

A constant-current STM image of a single and relatively small QD is shown in Fig. 3.10(a). It has a height of only 1.8 nm. Figure (b) shows $I(V)$ curves recorded above the QD (black) and on the WL (gray), respectively. Two current steps are observable on the QD. On the other hand, a continuous $I(V)$ increase appears on the WL. The increase on the WL is interpreted as a direct tunneling of electrons from the tip to the degenerately doped GaAs substrate. The effective barrier consisting of the vacuum barrier, the WL, and the GaAs tunnel barrier, gets smaller for increasing energy. Consequently, the tunnel current increases.

Figure 3.10(c) shows the simultaneously recorded dI/dV curves corresponding to (a). While the dI/dV signal on the WL does not show any structure, the dI/dV signal on the QD exhibits two peaks. It is demonstrated in section 2.1.2 that $dI/dV \propto$ LDOS at least for $V_{\text{sample}} < 200$ mV. Here we have slightly higher voltages. That dI/dV is still \propto LDOS in this case will be justified later. Anyhow, peaks in the LDOS correspond to single-electron states, which are expected for QDs.

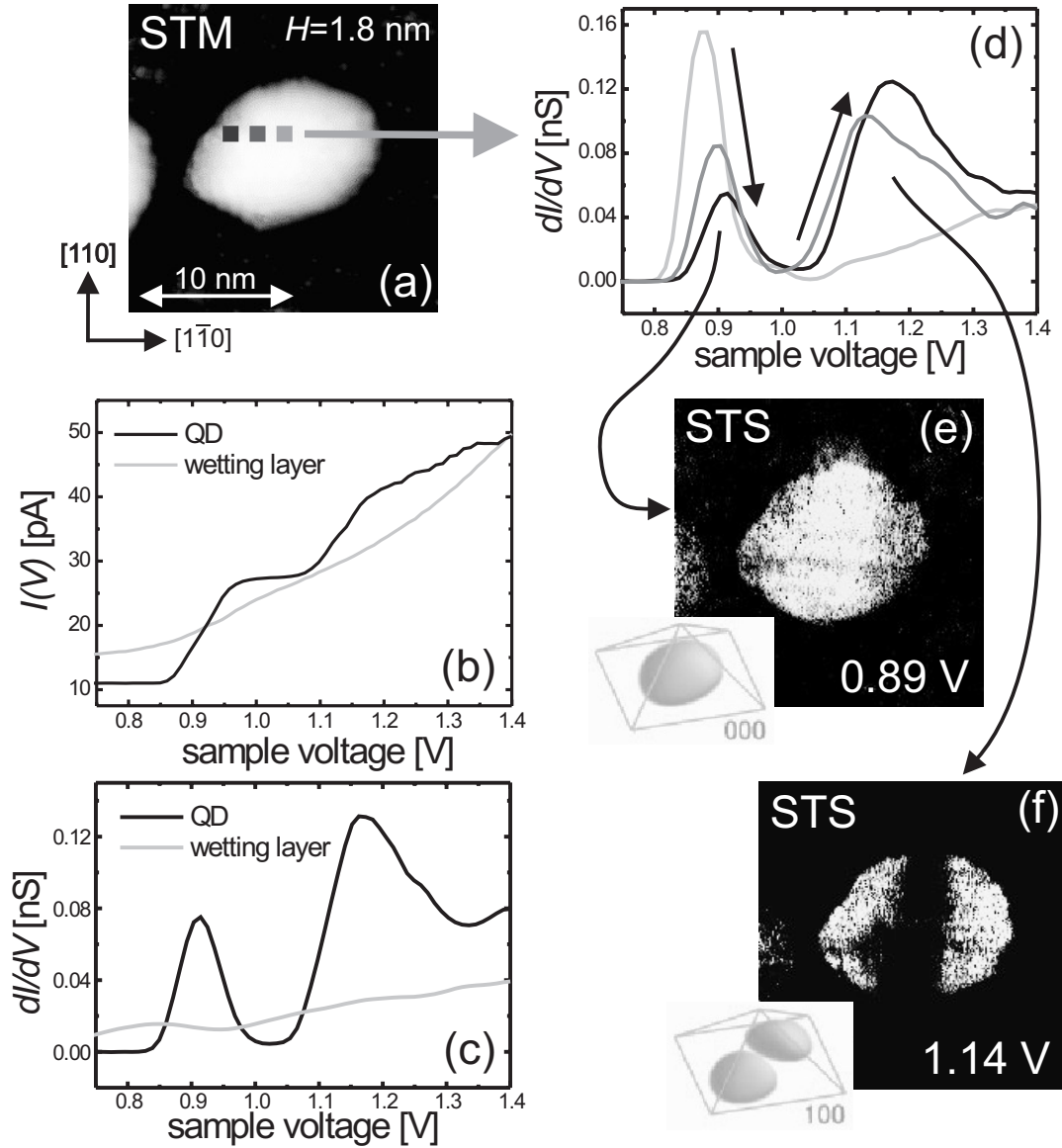


Figure 3.10: (a) Constant-current image of a QD from sample II ($V_{\text{sample}}=1.7$ V, $I=50$ pA, W tip, height H and crystallographic directions are marked in the figure). (b) $I(V)$ curves recorded on the QD (black) and on the WL (gray) with $V_{\text{stab}}=1.6$ V and $I_{\text{stab}}=50$ pA. (c) Simultaneously recorded dI/dV curves with $V_{\text{mod}}=28$ mV. (d) dI/dV curves recorded at different positions above the QD as marked in (a). (e) and (f) Spatially resolved dI/dV images at $V_{\text{sample}}=0.89$ and 1.14 V, respectively. Calculated squared wave functions are taken from [36] and are labeled by the number of nodes in different directions. All data in this figure are raw data.

In order to spatially resolve the intensity distribution of the peaks within the QD, the scanning area is divided into 150×150 points. At each point full $I(V)$ and dI/dV spectra are recorded consisting of 64 data points between V_{start} and V_{end} ($V_{\text{start}} \leq V_{\text{stab}}$). A sequence of 64 $I(V)$ and dI/dV images corresponding to different values of V_{sample} results.

Figure 3.10(d) shows that the intensity of the first peak decreases with distance from the QD center while the intensity of the second one increases. This is better visible in dI/dV images recorded at the peak positions. Figure (e), for example, shows the dI/dV image recorded at the first peak of (c) while (f) shows the dI/dV image at the second peak. Obviously, the first peak has a circular symmetric intensity distribution as expected for a (000) state of the conduction band, while the second one has a pronounced node in the center as expected for a (100) state. The numbers describe the number of nodes in $[\bar{1}\bar{1}0]$, $[110]$, and $[001]$ direction, respectively. Calculated wave functions are shown as insets (from [36]). In all of the 64 dI/dV images for this QD only the symmetries presented are found. Note, that all data in Fig. 3.10 are raw data without any filtering ¹.

The peak widths found in Fig. 3.10(c) and (d) require some discussion. They have a full width at half maximum (FWHM) of 70 and 150 mV. I believe that the widths are basically given by the lifetime of the electrons in the confined states. An upper boundary for this lifetime is the tunneling rate e_t through the undoped GaAs tunnel barrier. Tunneling rates up to $e_{t,\text{max}} = 3 \times 10^{13}$ /sec are deduced in section 3.2 from 1D Poisson calculations. Accordingly, the intrinsic lifetime broadening of the QD states should be $\leq \hbar/2 \times e_{t,\text{max}} = 10$ meV. Considering an average lever arm factor of about 5.5, which is deduced straightforwardly from the 1D-Poisson calculations presented in section 3.2, single-particle peaks with FWHM up to about 55 mV are expected. Thus, this simple model basically explains the measured peak widths. Generally, slightly larger peak widths are observed than deduced from 1D-Poisson calculations. Note, that a few parameters in the calculation are not accurately known. Measurements at different GaAs tunnel barrier widths are necessary to decide, if the tunnel coupling to the back gate is indeed the process which determines the peak widths.

As promised in section 2.1.2, a justification for $dI/dV \propto \text{LDOS}$ is needed for $V_{\text{sample}} > 200$ mV. In Fig. 3.10(c) the first peak at $V_{\text{sample}} = 0.9$ V has a height of $dI/dV = 0.0751$ nS and the following minimum at $V_{\text{sample}} = 1.02$ V has a height of $dI/dV = 0.0045$ nS. The remaining contribution of 0.0045 nS, which is 6% of the first peak intensity, suggests a contribution from the second term of equation 2.13. The intensity of 0.0751 nS originates only from the first term. Note, that for the first state no prior integration is needed, since ρ_s is zero for lower voltages. Thus, the experimental data show that the second term of equation 2.13 can be neglected. This ratio of 6% can additionally be deduced directly from equation 2.13. I assume that $\rho_t(E - eV) = \rho_t(0) = \text{constant}$ and that $\rho_s(E) = \text{constant}$ within a 10 meV energy interval around the peak and else zero. The 10 meV energy interval is deduced

¹This procedure works reproducibly for vacuum transferred samples. In contrast, no wave-function mapping was obtained for air-transferred samples (exposure to air for a few seconds). Only weakly reproducible peaks in dI/dV curves were found, although STM imaging was possible.

above from lifetime considerations. $dT/dV(E, eV, z)$ is in good approximation constant within the 10 meV interval. Thus, all coefficients can be extracted out of the integral. In ratio to the first term, ρ_t , ρ_s , and e are canceled. From the second term, $dT/dV(E = eV, V = 0.9V, z) \times 10 \text{ mV}$ is remaining after integration. This intensity should remain from the first state in dI/dV data at higher voltages. From the first term only $T(E = eV, V = 0.9V, z)$ remains, which is proportional to the intensity of the first state at the peak position. If I assume, that $z=0.5 \text{ nm}$, $\Phi_t=5.3 \text{ eV}$, and $\Phi_s=4.9 \text{ eV}$ and calculate the quotient $dT/dV(E = eV, V = 0.9V, z = 0.5\text{nm}) \times 10 \text{ mV} / T(E = eV, V = 0.9V, z = 0.5\text{nm})$, I get 2%. This is in reasonable agreement to the 6% deduced from the STS data. Thus, a measurable influence of the second term is present at voltages above the first peak, but anyhow the LDOS at the higher peaks is still largely proportional to dI/dV . The influence of the second term can explain the continuous increase in dI/dV data at higher voltages.

Another point, which requires some discussion, is the peak shift as a function of position, visible in Fig. 3.10(d). The peaks shift with increasing distance from the QD center. A possible explanation is the following: Since the QD is pyramidal, the tip gets closer to the WL and, thus, to the backgate by moving towards the rim of the QD. This leads to a stronger band-bending within the sample, which moves the QD states upwards. However, since the resulting peak shifts are small and no intermixing takes place, dI/dV images largely represent the peak intensity as a function of position. For a detailed quantitative comparison with calculations, the peak shift has to be considered and a plot of the peak intensity as a function of position would be more appropriate.

In short, the term "wave-function mapping" for dI/dV images is justified in the present case. The energy distance between the peaks is larger than the energy resolution δE (see section 2.1.3) of the STM. The peaks are broad but still resolvable and they show no intermixing. The LDOS is largely proportional to dI/dV . Consequently, the shape of a single $|\Psi_i(E_i, x, y)|^2$ is displayed in a single dI/dV image.

In order to get statistically relevant information of the state sequences for different QDs and to further prove the reliability of the method, a total of 25 QDs were investigated. Two macroscopically different tips were used (PtIr and W) and they were all prepared (pulsing, field emission, etc.) several times. Additionally, QDs on three different samples were analyzed. Thus, tip artifacts or sample dependences can be largely excluded.

The first two samples are identically grown (see section 3.2 and Fig. 3.6). All results presented in the Figs. 3.10 and 3.11 are obtained on these two samples. The only difference of the third sample is that it is grown with a 20 nm thick tunnel barrier instead of 15 nm. The thicker barrier should lead to a longer lifetime of the electrons within the dot. This should in turn lead to a reduced life time broadening of the single-electron states as discussed above, or even to charging effects. Unfortunately, spatially resolved STS measurements on sample III were not successful because several tip changes occurred during scanning. Only once, wave-function mapping could be obtained and indeed indicates charging effects as discussed at the

state sequence	number of QDs
(000)	10
(000), (100)	7
(000), (100), (010)	2
(000), (100), (010), (200)	1
(000), (100), (200)	3
(000), (100), (200), (300)	2

Table 3.1: Energetic state sequence for 25 different QDs.

end of this section.

Results obtained on three different QDs (15 nm tunnel barrier), all exhibiting more than two states, are shown in Fig. 3.11. 3D representations of the QDs are shown in (a1), (b1), and (c1), and again the QDs appear elongated in $[1\bar{1}0]$ direction. The QD height H is marked in the figures. Spatially averaged dI/dV curves over the whole QD area are shown in (a2), (b2), and (c2). The peaks are less well resolved in the averaged spectra due to the discussed peak shift as a function of position. For clarity, vertical lines mark the peaks. The squared wave functions are again visible in dI/dV images at the peak positions as shown in Fig. 3.11. The state sequences are (000), (100), and (200) for (a3)–(a5) (left row), (000), (100), (010), and (200) for (b3)–(b6) (middle row), and (000), (100), (200), and (300) for (c3)–(c6) (right row). V_{sample} for each image is indicated up/right and again the numbers describe the number of nodes in $[1\bar{1}0]$, $[110]$, and $[001]$ direction, respectively. For comparison, calculated squared wave functions are shown on the left of Fig. 3.11 (from [36]).

A total of 25 different QDs are analyzed with this method and the state sequences are summarized in table 3.1. In 40% of the QDs only a single (000) state is found. On the other hand, up to four states are partly observed. It is found that higher QDs tend to have a larger number of confined states. The heights of the 25 different dots vary between 1.7 and 9.4 nm (mean value: 4.5 nm). An interesting result is that different dots show a different number and a different energetic sequence of states. The (010) state is often missing, although (200) and even (300) states appear (see table 3.1). Thus, strong anisotropy in the electronic structure is found. This can be emphasized even more, if the nodes in $[110]$ and $[1\bar{1}0]$ are summed up: Only 3 nodes are found in $[110]$ direction while 33 nodes are found in $[1\bar{1}0]$.

The simplest explanation for the electronic anisotropy is the shape asymmetry of the QDs. The QDs appear slightly elongated in $[1\bar{1}0]$ direction. An average aspect ratio $A = \text{FWHM in } [1\bar{1}0] / \text{FWHM in } [110]$ of 1.3 is found in the constant-current image of Fig. 3.9(b). Partly larger aspect ratios appear in Fig. 3.11: $A = 1.6$ for (a1) and (b1) and $A = 1.4$ for (c1). These aspect ratios lead to a stronger confinement in $[110]$ than in $[1\bar{1}0]$ direction.

The confinement difference can be estimated from calculations on symmetric dots [36, 44–46] for different base lengths. Let us take, for example, the QD of Fig. 3.11(a1). The apparent QD base lengths in the $[1\bar{1}0]$ and $[110]$ direction are 26 and 19 nm, respectively. Note, that STM measures a convolution between tip and QD. The real base lengths can be smaller than the measured ones. If a symmetric

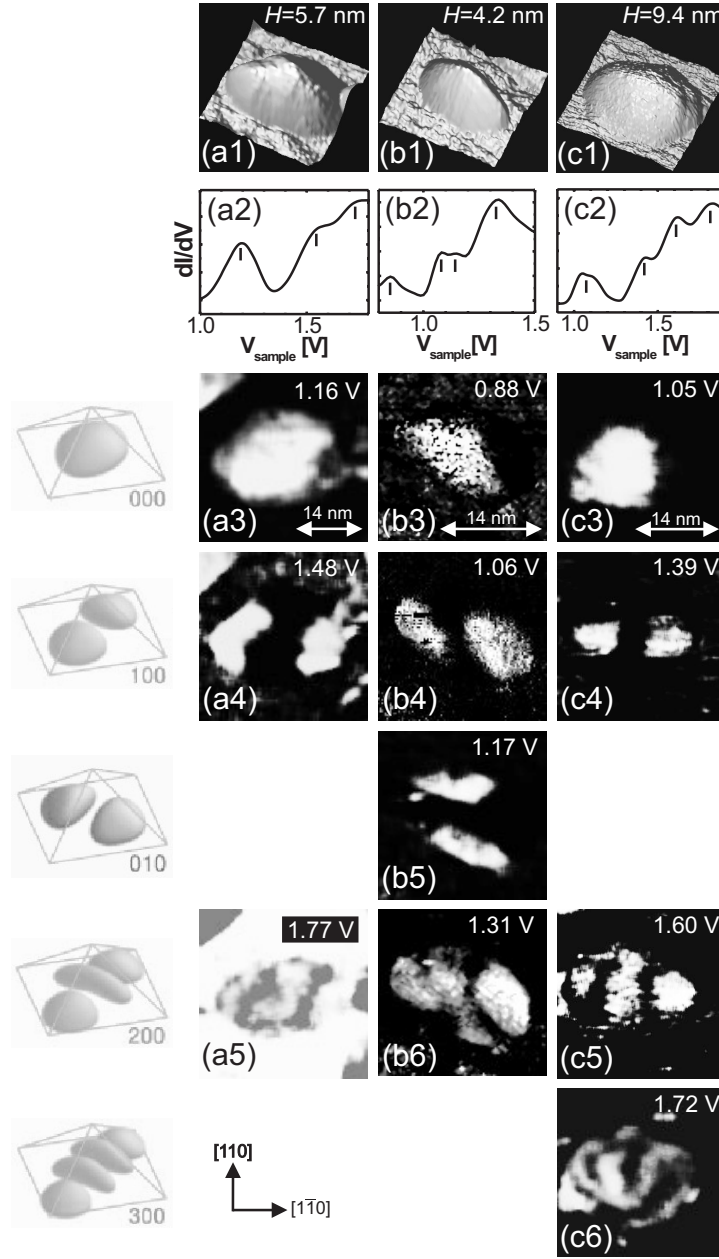


Figure 3.11: STS data of three different QDs. (a1), (b1), and (c1) 3D representation of constant-current images with heights H indicated. (a2), (b2), and (c2) $dI/dV(V)$ curves spatially averaged over QD area; peak positions are marked by vertical lines. (a3)–(a5), (b3)–(b6), and (c3)–(c6) dI/dV images recorded at V_{sample} as indicated; data are partly smoothed in order to enhance picture quality; the state in (a5) exhibits an energy close to the onset of the wetting layer, which results in a bright surrounding of the wave function; crystallographic directions are marked. (a1)–(a5) W tip, QD sample II, $V_{\text{stab}}=1.85$ V, $I_{\text{stab}}=50$ pA, $V_{\text{mod}}=15$ mV; (b1)–(b6) W tip, QD sample II, $V_{\text{stab}}=1.6$ V, $I_{\text{stab}}=50$ pA, $V_{\text{mod}}=27$ mV; (c1)–(c6) PtIr tip, QD sample I, $V_{\text{stab}}=2.4$ V, $I_{\text{stab}}=70$ pA, $V_{\text{mod}}=15$ mV. Constant-current images at $V_{\text{sample}} = V_{\text{stab}}$ and $I = I_{\text{stab}}$. Left column: calculated squared wave functions taken from [36] and labeled by the number of nodes in different directions.

QD with a base length of 26 nm and another one with a base length of 19 nm is considered, one gets according to [36] an energy difference of the p states of 125 meV. For comparison with the experimental results, V_{sample} at the peak positions has to be translated into energy E by using the 1D-Poisson solver as explained in section 3.2. The states in Fig. 3.11(a3)-(a5) at $V_{\text{sample}}=1.16, 1.48, \text{ and } 1.77$ V result in $E=126, 180, \text{ and } 226$ meV with respect to the conduction band minimum of the QD. Accordingly, the (010) state should appear at $180 \text{ meV} + 125 \text{ meV} = 305 \text{ meV}$. This is indeed above the (200) state which appears at 226 meV.

This consideration is also valid for the QD in Fig. 3.11(c1). This QD has apparent base lengths of 24 and 19.5 nm in the different directions. From [36] an energy shift of 75 meV between (100) and (010) states is predicted. With the 1D-Poisson correction the states of Fig. 3.11(c3)-(c6) at $V_{\text{sample}}=1.05, 1.39, 1.60, \text{ and } 1.72$ V result in $E=139, 212, 254, \text{ and } 278$ meV. Accordingly, the (010) state should appear at $212 \text{ meV} + 75 \text{ meV} = 287 \text{ meV}$ and this is indeed above the (300) state which appears at 278 meV.

This simple consideration, however, does not work for the QD of Fig. 3.11(b1): This QD has apparent base lengths of 20 and 14 nm in the different directions. An energy shift of 110 meV is predicted from [36]. With the 1D-Poisson correction the states of Fig. 3.11(b3)-(b6) at $V_{\text{sample}}=0.88, 1.06, 1.17, \text{ and } 1.31$ V result in $E=184, 212, 229, \text{ and } 249$ meV. The (010) state should therefore appear at $212 \text{ meV} + 110 \text{ meV} = 322 \text{ meV}$. Surprisingly, the (010) state appears immediately after the (100) state at 229 meV.

In short, this qualitative discussion cannot explain all details of Fig. 3.11. Although the discrepancy might be due to a wrong determination of the base lengths from Fig. 3.11(b1), detailed calculations taking the shape, the stress fields, as well as the Ga alloying of the InAs QDs into account are highly desirable in order to make more quantitative comparison.

The strong electronic anisotropy, which is attributed to shape asymmetry, is surprisingly not found for embedded InAs QDs on GaAs(001). For example, far-infrared measurements combined with capacitance spectroscopy revealed only evidence for a very weak anisotropy of 2 meV [47]. In this experiment, the QD s-states are charged *in situ* with capacitance spectroscopy and transitions between occupied s- and unoccupied p-states are measured with far-infrared spectroscopy at different magnetic fields. They found an energy separation at $B=0$ of approximately 2 meV [47]. By using, additionally, linear polarized light they explained this separation by a slight elongation of the dots of ≈ 0.5 nm in $[1\bar{1}0]$ direction.

In capacitance measurements, two s- and four p-states are found as a function of the magnetic field [48]. Charging and exchange energy (Hund's rule) can explain the peak separations and the magnetic field dependence [49]. No shape anisotropy is needed in order to explain the observed capacitance data.

Magnetotunneling spectroscopy on embedded InAs QDs on GaAs(001) show a rather degenerate (100) and (010) state, which is weakly visible as a torus in [34]. Thus, no electronic anisotropy is found there either. However, strong electronic anisotropy is found in embedded InAs QDs on GaAs(311)B with this technique [33],

where a missing (010) state is found between (100) and (200) (Fig. 3.2).

Nevertheless, there is not a single report about strong electronic anisotropy for embedded InAs QDs on GaAs(001). None of the authors find an indication for a (200) state appearing prior to the (010) state. The most likely explanation for this discrepancy between freestanding and embedded InAs QDs on GaAs(001) is that the strain field changes during overgrowth. Moreover, there might be compositional or shape changes of the QDs due to the overgrowth.

All results which are presented above are obtained on sample I and II. At the end, a challenging result on a QD of sample III should be presented. In contrast to sample I and II, sample III is grown with a 20 nm thick tunneling barrier.

STS images at different V_{sample} are shown in Fig. 3.12(a)–(g). Unfortunately, this QD drifted out of the scanning area during measurement. An STM image obtained prior to spectroscopy is shown in (A). The averaged spectrum shown in (B) indicates, as expected, peaks, but not all states have a clearly resolved corresponding peak. The sample voltages of the states shown in (a)–(g) are indicated, for clarity, with vertical lines in (B).

Surprisingly, each corresponding wave function, except of (f), appears twice. The state sequence starts, as expected, with (000) (a) and (100) (b), but than again (000) (c) and (100) (d) states appear. Afterwards, (200) (e) and (300) (f) appear, but than again the (200) state (g) is repeated. The symmetries shown in (a)–(g) are the only symmetries appearing at all voltages between 0.4–1.55 V.

The QD apparent base lengths of Fig. 3.12(A) are 17.4 nm and 14.4 nm in $[1\bar{1}0]$ and $[110]$ direction, respectively, and the height is 1.7 nm. The states in Fig. 3.12(a)–(g) at $V_{\text{sample}}=0.71, 0.81, 0.94, 1.03, 1.14, 1.28,$ and 1.42 V result in $E=134, 144, 156, 165, 175, 187,$ and 199 meV, according to the 1D-Poisson calculation. Note, that the difference between s- and p-states of 10 meV is unexpectedly small. From [36] an energy shift between the (100) and (010) states of 70 meV is predicted. Accordingly, the (010) state should appear at $(144+60)$ meV=204 meV. This is indeed above the highest state which appears at 199 meV.

Note, that a QD charging could not be included in the simple 1D calculation. This was not necessary for the QD sample I and II where at maximum one electron is in the QD. However, in the present case the QD is obviously charged. A charge which remains in the QD will increase the electrostatic potential. Thus, the calculated energies E include a charging energy and, therefore, the single-electron states are less separated than predicted based on the simple 1D-Poisson calculations.

As mentioned above, a possible explanation for the repeating of the wave functions is charging. An s-shell charging energy of 21.5 meV and 23.3 meV for strain-induced InAs QDs is concluded from capacitance data in [47] and [48], respectively. Theory finds an s-shell charging energy for symmetric QDs (base plane lengths=14–17 nm) of 24–21 meV [36]. Here we found in good agreement that the two (000) states are separated by 22 meV, the (100) states by 21 meV, and the (200) states by 24 meV.

The obtained sequence might be the following: First, the electrons tunnel through an s-state at zero charging of the QD (a). Then, the electrons tunnel through the p-state at zero charging (b). Next, the electrons tunnel through the s-state at single charging (c) and so on. Consequently, charging appears to be possible but not to be necessary. In average, the QD is charged at a part of the time. Such a situation requires similar barriers on both sides of the QD.

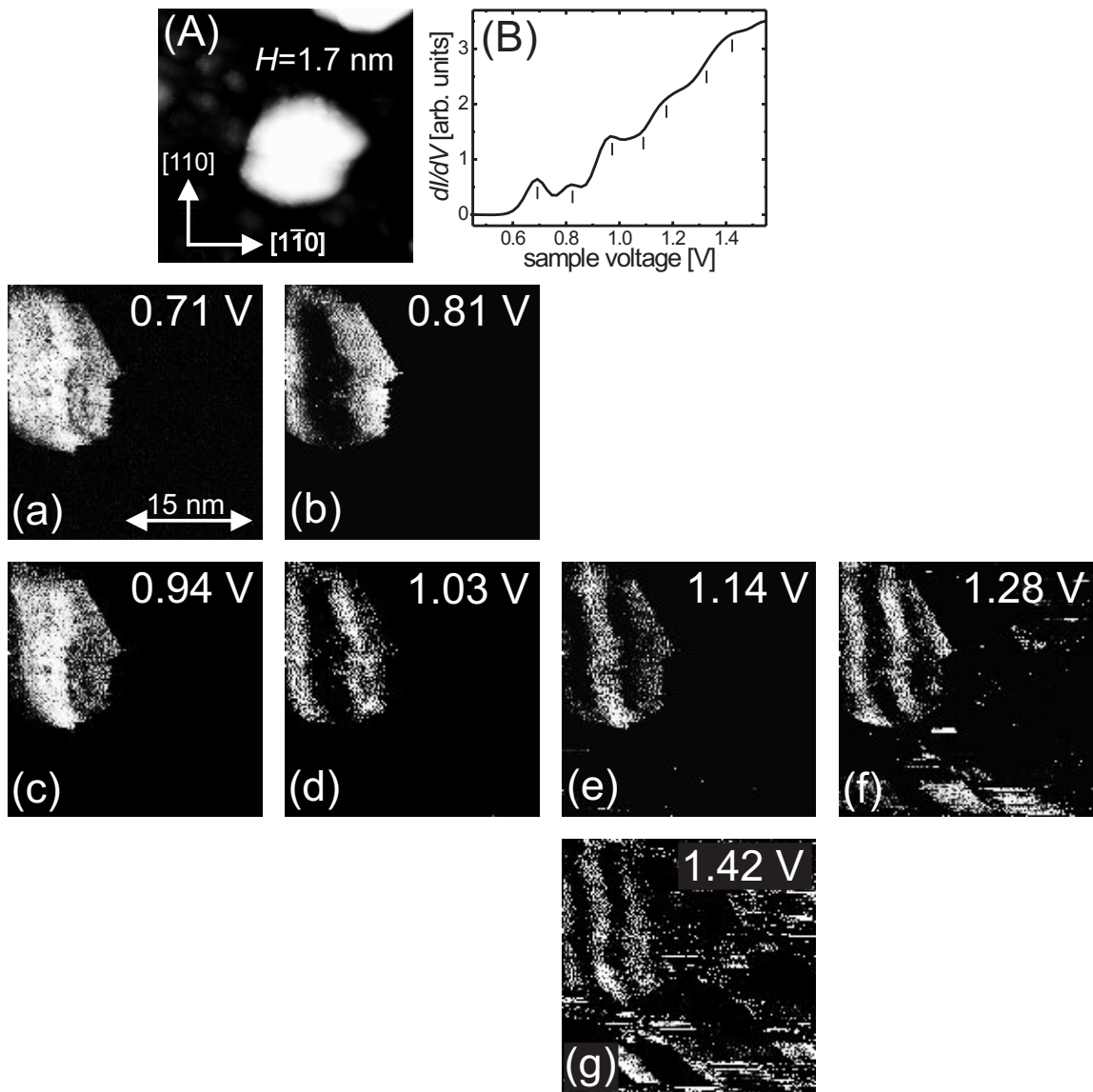


Figure 3.12: (A) STM image prior to spectroscopy ($V_{\text{sample}}=2.3$ V, $I=70$ pA, crystallographic directions are marked). (B) dI/dV curves spatially averaged over QD area (vertical lines mark the V_{sample} of (a)–(g)). (a)–(g) dI/dV images at different V_{sample} marked in the figures ($V_{\text{stab}}=1.8$ V, $I_{\text{stab}}=70$ pA, $V_{\text{mod}}=29$ mV, W tip, sample III). All data in this figure are raw data.

On the other hand, charging cannot be explained for a 20 nm thick tunneling barrier with 1D-Poisson calculations. The second tunneling barrier (InAs/GaAs band offset) shows for the strongest confined state at $V_{\text{sample}}=0.71$ V a width of 6.7 nm and a height of 0.26 eV. Consequently, a tunneling rate of $e_t=5.43 \times 10^{10}/\text{sec}$ is deduced from equation 3.1. However, the highest current in the experiment is the stabilization current of 70 pA. This corresponds to $4.4 \times 10^8/\text{sec}$ which is still two orders of magnitude too small in order to explain charging.

Note, that a corresponding calculation for a 1.7 nm high dot at $V_{\text{sample}}=0.71$ V but 15 nm tunneling barrier results in $e_t=2.6 \times 10^{11}/\text{sec}$. Thus, the 5 nm thicker tunneling barrier reduces e_t by one order of magnitude.

However, it should be stressed, that the calculations are based on a 1D model and require parameters which are not exactly known. Further experiments are required to find out if charging indeed appears in these QDs.

Note finally, that the results shown in Fig. 3.12 could not be reproduced on other QDs of sample III. Spatially resolved STS on sample III appeared to be difficult, because a lot of tip changes occurred during the measurement. This is even visible in Fig. 3.12: The STM image prior to spectroscopy (A) shows the QD to be elongated in $[1\bar{1}0]$. Surprisingly, the STS data (a)–(g) show the QD elongated in $[110]$ direction. Such a tip change during STS was never observed on samples I and II. I assume that the thicker tunneling barrier of sample III made a reproducible wave-function mapping more difficult. The tip is closer to the surface at similar I_t and can, thus, easier pick up adsorbates which lead to tip changes.

3.4 Conductive AFM results

All experimental results in section 3.3 are obtained on QD samples grown, transferred, and measured in UHV by STM. To demonstrate that UHV is necessary, this section describes conductive AFM results produced under ambient conditions after removing the sample (15 nm thick barrier) out of the UHV.

STM measurements (Nanoscope E, Digital Instruments) within an Ar glove-box (MBraun) can be performed on QD samples, which are exposed to air for a few seconds, but the imaging is very unstable. A more stable method in air is AFM (described in section 2.2). A 3D image obtained from contact AFM (Nanoscope IIIa, Digital Instruments) is shown in Fig. 3.13.

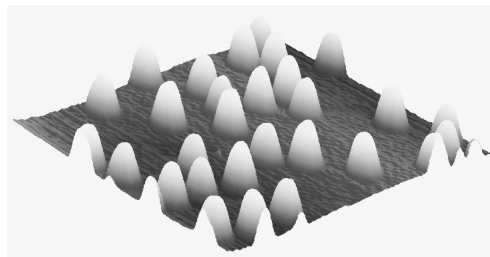


Figure 3.13: 3D contact AFM image in air of an InAs QD sample (400×400 nm²).

Simultaneously with the topography a current flow between tip and sample can be measured, if conductive AFM tips are used. The current flow is measured at different voltages and can be displayed as a function of position. This leads to a map of the local conductivity. Thus, this method can study the topography and the electronic properties of InAs QDs in air. Conductive Co/Cr coated n^+ -Si tips (2.8 N/m, 70 kHz) are used for this purpose.

Conductive AFM results in air on InAs QDs grown on GaAs(001) samples (same as in Fig. 3.6) are shown in Fig. 3.14. Figure (a) shows the sample topography obtained with contact AFM. Simultaneously, current-images are obtained for $V_{\text{sample}} = -1, -2,$ and -3 V as shown in (b1), (c1), and (d1), respectively. For small V_{sample} no current is observed, neither on the QDs nor on the WL. Thus, only noise is measured at $V_{\text{sample}} = -1$ V in (b1) (I range=0.5 pA). At $V_{\text{sample}} = -2$ and -3 V the current flow starts basically over the QDs as shown in (c1) (I range=3 pA) and (d1) (I range=40 pA), respectively.

1D-Poisson calculations can reconstruct this voltage dependence of the current over the QDs. The band profile for $V_{\text{sample}} = -1, -2,$ and -3 V is shown in (b2), (c2), and (d2), respectively. An averaged dot height of 6 nm and room temperature material parameters are used in these calculations. Further, a 0.5 nm oxide layer between tip and sample, a workfunction of the metallic tip of 5.3 eV, and a Ga content within the dot of 40% are assumed.

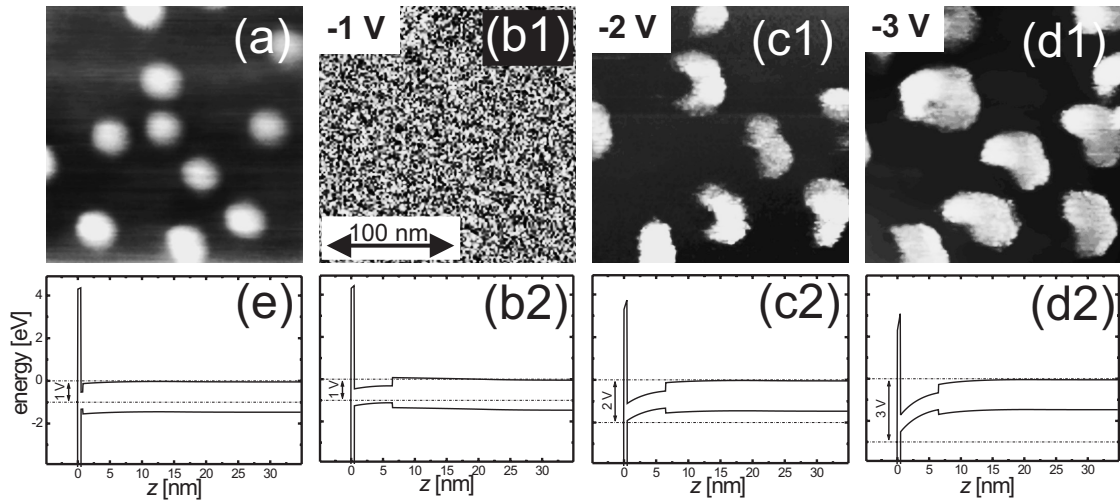


Figure 3.14: Conductive AFM (a) Contact AFM topography (z range=10 nm). (b1), (c1), and (d1) Current images at $V_{\text{sample}} = -1$ V (I range=0.5 pA), -2 V (I range=3 pA), and -3 V (I range=40 pA), respectively. (b2), (c2), and (d2) Calculated band-profiles over a QD at $V_{\text{sample}} = -1, -2,$ and -3 V, respectively. (e) Calculated band-profile over the WL at $V_{\text{sample}} = -1$ V (Fermi level pinning not included).

Electrons tunnel from the conduction band of the sample to the tip at negative V_{samples} ². In (b2) a barrier is remaining at the band offset between InAs and GaAs, which inhibits a current flow. Thus, only noise is measured in (b1). At higher voltages, however, the barrier disappears as shown in (c2) and (d2). Consequently, a current flow sets in above the QDs as shown in (c1) and (d1).

An open question is, why the current flow is suppressed over the WL. It is even more surprising, if we consider the band profile over the WL at -1V (the InAs WL is assumed to be 0.303 nm thick in the calculation with a Ga content of 40%). This is shown in (e). A current onset at -1 V should be possible above the WL (e) and not above the QDs (b2). In (e) the electrons can flow from the conduction band of the sample into the tip without any barriers (except the tip and sample oxide). In contrast, a barrier at the band offset between InAs and GaAs remains in (b2). A similar experiment and a possible reason for this discrepancy is reported in [50]. The authors claim that the thin InAs WL oxidizes in air. Therefore, the WL should behave like an oxidized GaAs substrate. It is reported in [50] that oxidized GaAs surfaces have a Fermi level pinning at midgap due to surface states. This results in a formation of a surface depletion layer. This in turn forms a nanoscale Schottky diode between WL and tip which effectively inhibits the current flow above the WL. In contrast, oxidation of InAs is reported to have a Fermi level pinning at 0.13 eV above the conduction band [51]. Thus, the only barrier over the QDs is the band offset between GaAs and InAs. The applied voltage can induce an additional band bending which leads to an accumulation and, consequently, to a current flow. Note, that Fermi level pinning could not be included in these simple 1D-Poisson calculations. Thus, the contrast in conductance images observed in air is due to a different oxidation of the WL and the QDs and has nothing to do with confined states of the dots.

A published STM study of InAs QDs on GaAs(001) samples, which were transferred in air, showed a similar increasing of the conductivity above the QDs in current-images at negative sample voltage [52]. At positive sample-voltage no contrast was obtained. They interpret this result as electron tunneling through single-electron states. I think that this explanation is not appropriate. In comparison with [50] and the results presented here, the contrast in the current-images of [52] is probably only due to the different Fermi level pinning of QD and WL.

²This is the opposite case as in the STM experiment of section 3.3 where a positive sample voltage detects the single-electron states within the conduction band. Anyway, single-electron states could not be resolved with conductive AFM. No contrast was obtained up to +10 V.

3.5 Scanning capacitance microscopy results

Single-electron states in embedded InAs QDs are detectable by capacitance spectroscopy [47, 48], as already mentioned in section 3.3. Two separated s-states appear and also different p-states are weakly resolved. However, the capacitance measurements average over 1400 - 70000 embedded dots depending on the gate areas [48]. This can be improved down to approximately only 10 embedded dots for gate areas $< 0.5 \mu\text{m}^2$, which has proven to provide a much better resolution for the s- and p-states [53]. Section 3.3, however, demonstrates differences between different dots and differences between freestanding and embedded dots. Thus, a spatially resolved technique for capacitance measurements on individual and freestanding QDs is desirable, too.

High-end spectroscopy measurements require low temperatures and UHV. Such a UHV low temperature scanning capacitance microscope is still under construction [54].

In order to check if SCM contrast is possible under ambient conditions (same sample as in Fig. 3.6), a commercial AFM (Dimension 3000, Digital Instruments) is used. It measures topography and capacitance in contact mode. The latter is done with a capacitance bridge which works at a fixed modulation voltage $V_{\text{mod}}=1 \text{ V}$, an adjustable frequency f , and bias voltage V_{sample} ³.

However, no SCM contrast could be obtained on the InAs QD samples, which include a native oxide, even after varying all available parameters. Figure 3.15(a) gives a qualitative explanation: Two capacitances C_1 and C_2 are in series. The capacitance C_1 is different between tip and QD or tip and WL, but C_2 (between QD/WL and backgate) is the same in both cases. The total capacitance C_{tot} is given by:

$$\frac{1}{C_{\text{tot}}} = \frac{1}{C_1} + \frac{1}{C_2}.$$

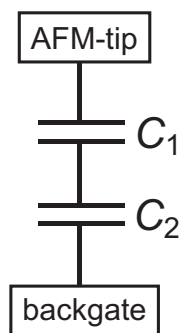


Figure 3.15: Sketch of two capacitances in series for the case of SCM: C_1 between tip and QD (or WL) and C_2 between QD (or WL) and backgate.

³Note, that for the detection of single-electron states as in section 3.3 a modulation voltage of 1 V (fixed in this AFM) is much too large.

Each capacitance is proportional to the reciprocal distance of the electrodes. The distance between tip and QD (or WL) is only the thickness of the thin native oxide film (≈ 0.5 nm), while the distance between QD (or WL) and backgate is much larger (≈ 25 nm, deduced from 1D-Poisson calculations). It results from this simple consideration that $C_1 \gg C_2$. Note, that C_{tot} is measured in SCM. Therefore, mainly C_2 contributes to C_{tot} and the contribution from C_1 is negligible. But C_1 includes the information about the electronic states in the QD and the WL. Thus, no contrast could be obtained in SCM between QDs and WL with a native oxide. In order to reduce C_1 , a thicker oxide layer is desirable.

A common method to enhance the native oxide thickness is the oxidation under O_3 atmosphere [55, 56]. The O_3 is prepared with an UV lamp within a furnace. An O_3 treatment at 200°C for 10 min is sufficient to enhance the oxide thickness. The resulting SCM image is shown in Fig. 3.16. Contrast is obtained between QDs and WL. The capacitance above the QDs is larger than above the WL. In this SCM measurement a modulation voltage of 1 V is applied with a frequency of 5 kHz at a sample voltage of 0 V. The more electrons that tunnel out and into the tip, the higher is the measured capacitance signal. Note, that the conductance was found to be larger above the QDs than on the WL in section 3.4. Thus, the QDs can be better charged than the WL and, consequently, a larger capacitance $C = Q/U$ is measured above the dots.

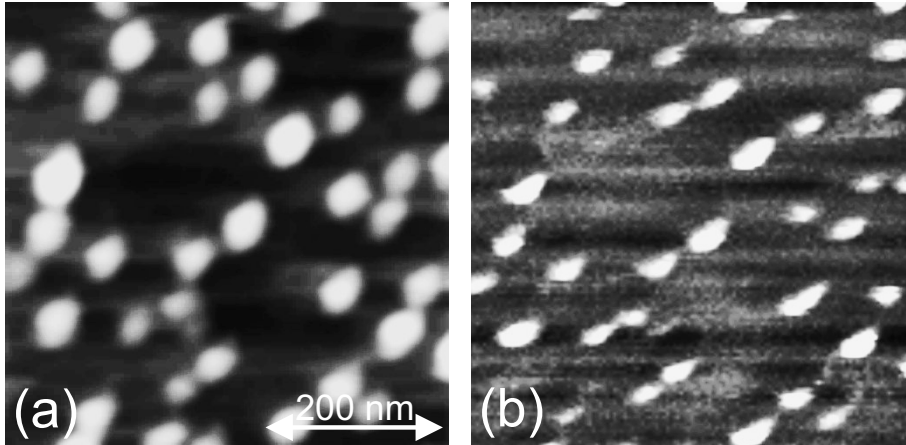


Figure 3.16: (a) Topographic image of the InAs QDs measured by contact AFM (z range=11 nm). (b) Simultaneously obtained SCM image (SCM signal in [arb. units], $V_{\text{mod}}=1$ V, $f=5$ kHz, and $V_{\text{sample}}=0$ V).

A similar SCM experiment is reported in [57]. They used an UHV SCM with $V_{\text{mod}}=0.1$ V and measured on samples which are transferred in air and have a native oxide. At $V_{\text{sample}}=0$ V no contrast is obtained between QDs and WL. However, at -0.5 and -1 V contrast appears even with the thin native oxide. With these sample voltages no contrast was obtained with the Dimension 3000. This can have the following reasons: In [57] the dots are grown directly on the n-doped GaAs. Thus,

C_2 is larger due to the missing tunneling barrier. Additionally, another capacitance sensor is used, which may have a better resolution.

Summary

Wave-function mapping of single-electron states is achieved with STS on freestanding strain-induced InAs QDs, which are grown by MBE and transferred within UHV. The number of nodes in $[1\bar{1}0]$ direction is larger than the number of nodes in $[110]$ direction. This effect is attributed to shape asymmetry of the QDs, which are elongated in $[1\bar{1}0]$ direction. The influence of an oxide layer is analyzed by SCM and conductive AFM in air. The oxidized QDs have a larger conductance and a larger capacitance than the oxidized WL. This effect is attributed to a different Fermi level pinning between oxidized WL and oxidized InAs QDs.

Chapter 4

InAs, InP, and CdSe nanocrystals

Another type of QDs studied in this thesis are semiconductor nanocrystals, also called clusters, which are synthesized by colloidal chemistry. Nanocrystals are spherical and not pyramidal shaped as the strain-induced QDs studied in chapter 3. Additionally, the nanocrystals are in organic solutions and they can be size-selected down to approximately 5%. For this study, they were synthesized by Dr. Dimitri Talapin in the group of Prof. Dr. Horst Weller (Institute of Physical Chemistry, University of Hamburg, Germany). A lot of different materials are available as clusters, for example, InAs, InP, CdSe, CdS, HgS, PbS, ZnO, FePt, Co, and even core/shell nanocrystals can be fabricated, for example, InAs/ZnSe is possible. Here, we concentrate on semiconductor InAs, InP, and CdSe nanocrystals.

A big advantage of the clusters with respect to the strain-induced InAs QDs is that they are pure materials with no intermixing and that they have a more well defined geometry. This makes the interpretation of the data easier.

However, since the clusters are not produced in UHV, a sample preparation compatible with low temperature STM measurements in UHV is required before wave-function mapping could be possible. Unfortunately, I did not achieve wave-function mapping so far, but I would like to show some preliminary results. After an introduction and a literature survey given in section 4.1 these first results are presented in section 4.2.

4.1 Basic properties

Semiconductor nanocrystals are nm-sized spherical crystals, which are surrounded by organic ligands. In this work, InAs, InP, and CdSe are used as semiconductors and trioctylphosphine (TOP) as the organic ligand. The nonpolar TOP ligands enable solubility of the clusters in nonpolar solvents like toluene. A scheme of InP clusters in solution and the chemical structure of the ligands are shown in Fig. 4.1.

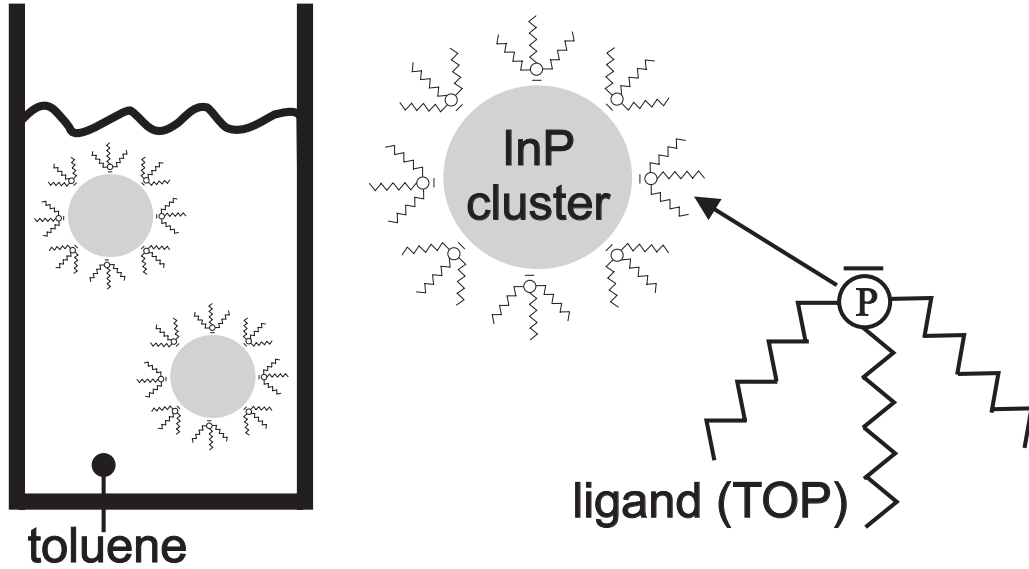


Figure 4.1: Scheme of InP clusters solved in toluene with organic TOP ligands.

The InP clusters are synthesized via the reaction of InCl_3 and $\text{P}(\text{Si}(\text{CH}_3)_3)_3$ in TOP at elevated temperatures. A detailed description of InP nanocrystal synthesis can be found in [58]. A similar synthesis of InAs clusters is described in [59]. Additionally, several PhD thesis deal with preparation and characterization of these clusters as [60, 61].

Semiconducting nanocrystals are also QDs, which show strong quantization of the electronic states [62, 63]. The major difference to the strain-induced QDs of the previous chapter is that they are spherical and not pyramidal in shape. This has an influence on the wave functions of the single-electron states. Squared wave functions of InAs clusters calculated by Michael Tews in the group of Prof. Dr. Daniela Pfannkuche (Institute of Theoretical Physics, University of Hamburg, Germany) [64] are shown in Fig. 4.2. The first state has an s-like symmetry (not shown). The p-states are separated into a p_z^2 -state (a) and a degenerate $p_x^2 + p_y^2$ -state (b). The lifting of the degeneracy is due to the fact that the STM tip voltage has been taken into account. The resulting Stark effect annihilates the degeneracy between p_z and p_x/p_y , but not between p_x and p_y . The p_x/p_y energy is shifted downwards in energy with respect to the p_z energy, due to the orientation of the corresponding wave functions.

A general goal of this project is to measure the predicted wave functions with STS, as it is done in the case of strain-induced InAs QDs in section 3.3. Therefore, a connection between the liquid "cluster world" with the "UHV world" of STM has to be established. This has been tried with the following simple technique: A droplet (or more) of the cluster solution is deposited on a Au or HOPG sample in air. Spin coating or N_2 blowing can be used to dry the sample. Au and HOPG are used, because they enable stable STM imaging in air.

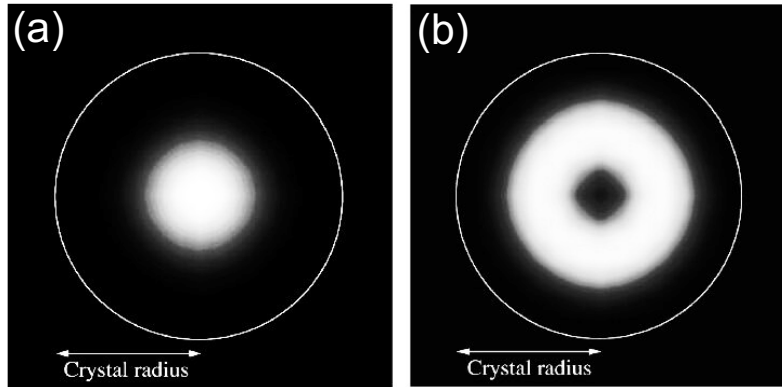


Figure 4.2: Calculated wave functions of InAs clusters as seen from an STM tip. (a) p_z^2 - and (b) degenerate $p_x^2+p_y^2$ -state. Data are taken from [64].

The cluster preparation from solution is reported to form monolayer-high cluster agglomerates on HOPG [65–68], as shown in the air tmAFM images of Fig. 4.3. A chloroform CdSe cluster (diameter, $\varnothing=4$ nm) solution was deposited on HOPG [65]. Randomly shaped agglomerates are found but no isolated clusters. This is due to the

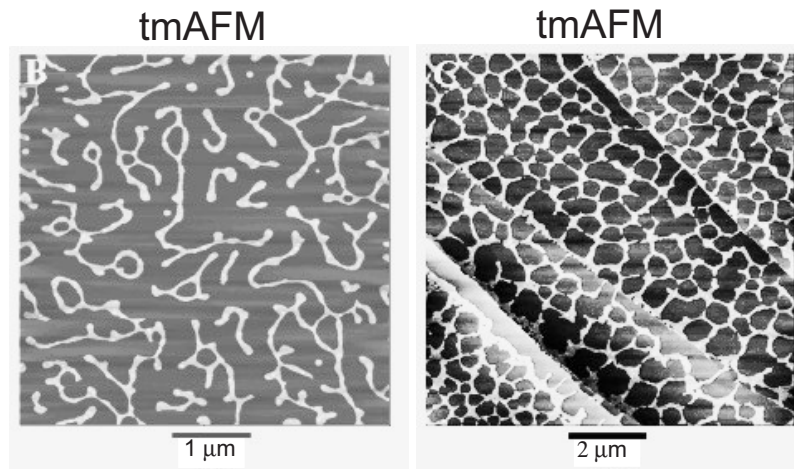


Figure 4.3: Monolayer of GdSe cluster ($\varnothing=4$ nm) agglomerates deposited from a chloroform solution on HOPG and measured with tmAFM in air (taken from [65]).

following reason: During the drying process the concentration of the clusters in the solution increases. Consequently, the nanocrystals experience a stronger attraction due to the reduced screening of the Van der Waals forces between each other. Homogeneous nucleation is the result. The agglomerates are monolayer thick due to the strong wetting of the cluster solution onto HOPG. Additionally, the agglomerates are found to be mobile at elevated temperatures on HOPG but not dividable. In [66] it is reported that CdSe cluster agglomerates diffuse rapidly on a graphite surface at 50–100°C without dissociation.

The cluster agglomeration is reproduced in this thesis for InAs, InP, and CdSe clusters on HOPG and Au, as shown in the next section.

A method to obtain individual and single nanocrystals is reported in [69–73]: First, 1,6-hexanedithiol [HS(CH₂)₆SH] is used to create a self-assembled monolayer (SAM) on Au. Therefore, the molecules are arranged vertically on the surface and are close-packed. The one sulfur atom bonds to the Au surface while the other stands freely on the top and can bond, for example, to clusters. The hexanedithiol preparation is as follows ¹: 0.22 ml 1,6-hexanedithiol is removed via a syringe and is filled into a petri dish filled with isopropanol or ethanol. The solution is stirred and the Au on mica sample is placed in the solution for 12 h. After the preparation, a SAM should be formed which can bond the nanocrystals from solution [69]. Note, that other SAMs are also used to bond clusters. For example, a SAM of sulfur-terminated oligo(cyclohexylidene) is used in [74] to bond single CdSe nanocrystals on Au.

All the experiments mentioned above report topographic imaging of single nanocrystals with STM. Additionally, low temperature STS is performed on the clusters. One example is presented here: InAs/ZnSe core/shell nanocrystals are analyzed with STM and STS in [73]. They were bound to Au via a hexanedithiol SAM. The main results are shown in Fig. 4.4. In (b) the topography of a cluster is shown, as measured with STM. A corresponding spectrum is shown in (a). Peaks are visible in the conduction band of the cluster, which are noted as s and p. The s-state is two fold degenerate with a spacing assigned to the single-electron charging energy ². The higher order multiplet is assigned to tunneling through the p-states. The peaks in the valence band are not further analyzed. Current images at different voltages revealed a wave-function mapping of different states. This is shown in (c), (d), and (e), for an s²-, p_x²+p_y²-, and p_z²-state, respectively. As predicted from theory [64] and shown above, only the p_x- and p_y-state is degenerate while the p_z-state is shifted compared to p_x/p_y due to the Stark effect induced by the electric field between tip and sample. Note, that current images always display an overlap of all states below the Fermi level of the tip. Thus, Fig. 4.4(d) shows an overlap of s, p_x, and p_y, while (e) shows an overlap of s, p_x, p_y, and p_z.

Note further, that it has never been established, that hexanedithiol actually forms a SAM on Au. None of the experiments mentioned above resolve a SAM with STM. Additionally, structural studies including STM show no evidence of ordered vertical phases of hexanedithiol on Au even if different growth conditions are used [76]. A striped phase is found with the molecules lying flat on the surface due to the strong S–Au bond of both sulfur atoms. In contrast, STM on monothiols on Au show a vertical and highly ordered SAM, reported for example in [77, 78]. In [77], again, a stripe phase is found for hexanedithiol on Au.

¹Private communication with Dr. Erik Scher, Department of Chemistry, University of California Berkeley, USA.

²A possibility to overcome this charging is to deposit the clusters without a SAM. This is shown in [75] for InAs clusters which are deposited on HOPG.

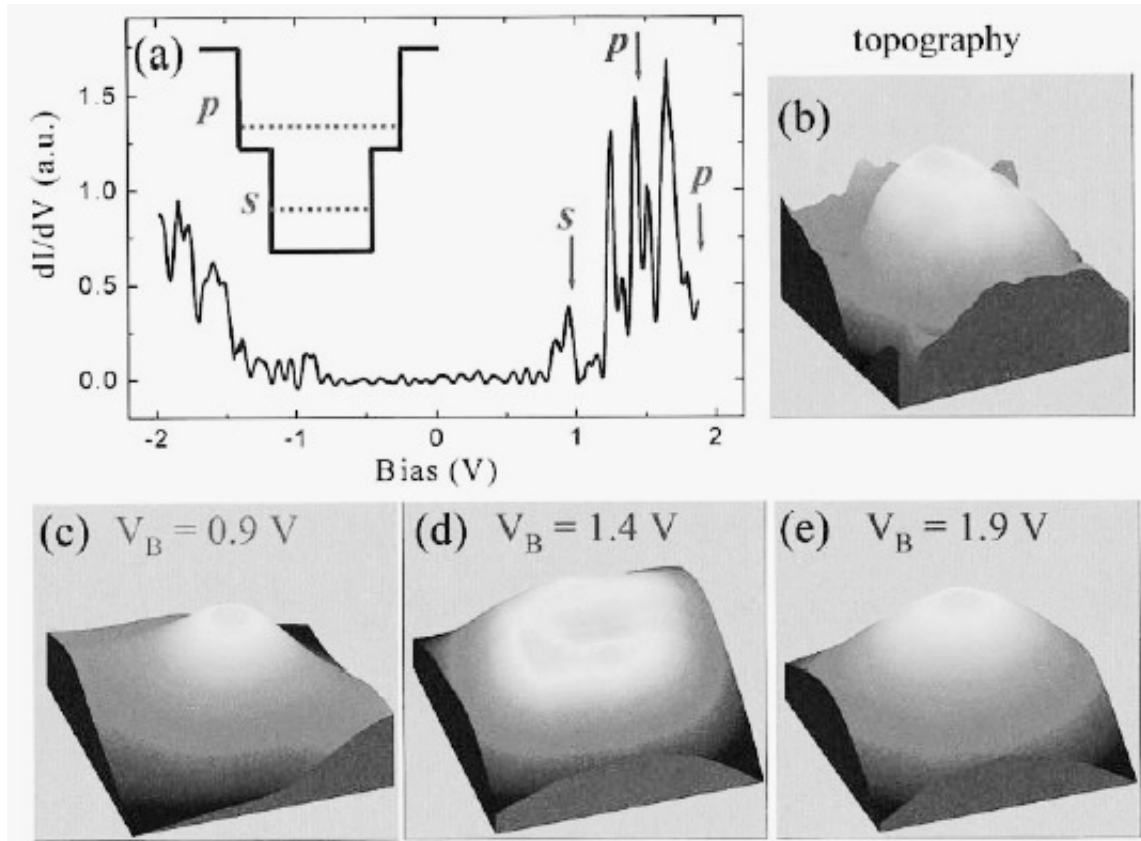


Figure 4.4: (a) STS curve taken above a single InAs/ZnSe core/shell cluster (s- and p-states are marked). (b) STM image of the cluster. (c), (d), and (e) Current images at different voltages (marked) reveal s^2 , $p_x^2 + p_y^2$, and p_z^2 squared wave functions, respectively (taken from [73]).

4.2 Sample preparation

InAs, InP, and CdSe clusters with TOP ligands solved in toluene are used. An optical density, which is measured with ultraviolet/visual spectroscopy, of 0.1–0.3 at the exciton peak is used. The optical density of the exciton peak is proportional to the nanocrystal concentration of the solution. Note, that the absolute concentration is not exactly known. A droplet is deposited on the freshly cleaved graphite surface and is blown dry with N_2 . Randomly shaped agglomerates could be obtained on graphite samples as exemplified in Fig. 4.5. They have the same height in tmAFM as the cluster diameter obtained previously by high-resolution transmission electron microscopy (TEM). Cluster resolution within the agglomerates could not be achieved with tmAFM but with TEM as shown in (b). As reported in [66], the agglomerates are not fixed on the HOPG surface. Here, contact AFM could easily push the clusters during scanning. The effect is called tip-induced mobility. It is demonstrated in (c) and (d), where the same surface region is measured with tmAFM before and after contact AFM. The area not scanned by contact AFM is unchanged, but in the

scanned area the clusters are pushed aside. Maybe this pushing creates unbound clusters or cluster agglomerates, which can be easily pulled towards the AFM tip during tapping mode. Probably this is the reason for the reduced image quality in (d).

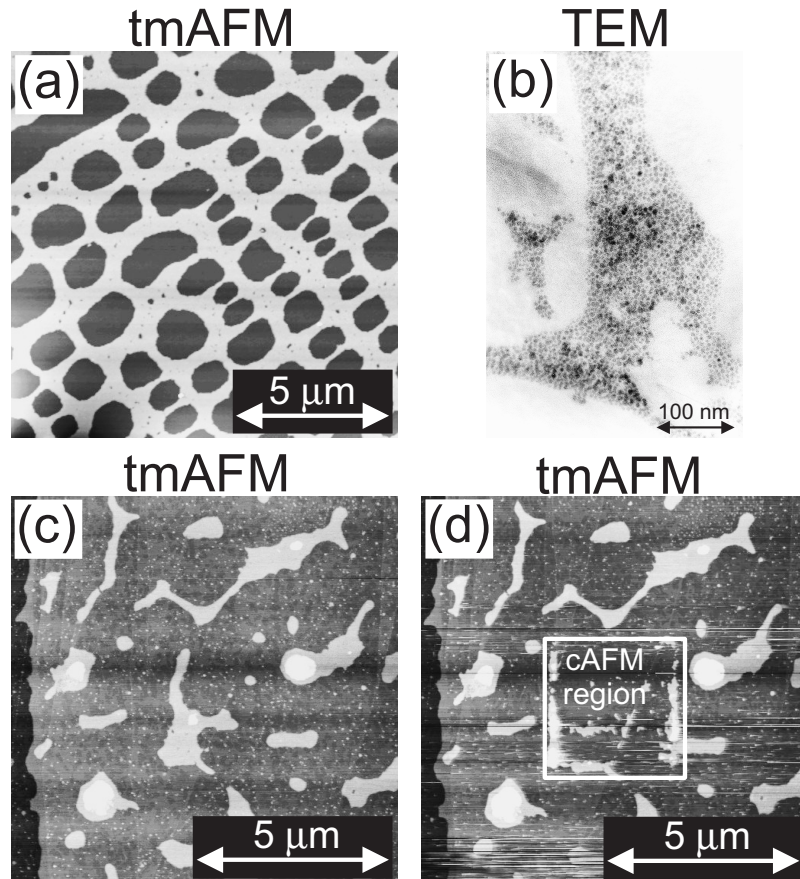


Figure 4.5: Cluster agglomerates on graphite (imaging techniques indicated). (a) CdSe clusters ($\varnothing=5$ nm) on a graphite TEM grid prepared by Dr. Dimitri Talapin. (b) InAs clusters ($\varnothing=2-10$ nm) on HOPG (TEM by Dr. Dietmar Junkereit, Dr. Petra Kreutzer, and Prof. Dr. Rainer Anton). (c) InP clusters ($\varnothing=4-6$ nm) on HOPG. (d) Same as (c) but after contact AFM (area marked).

This successful preparation is only the first step towards the major goal of this project: Wave-function mapping. Therefore, STM and STS imaging on these samples must be made possible. Unfortunately, STM could not image the cluster agglomerates on graphite substrates. The tip-induced mobility is too strong and a very unstable imaging results.

Thus, another idea has been tested: Nanopits "burned" into the graphite surface could potentially trap and immobilize the clusters or even prevent them from agglomeration. They are prepared by mild UHV Ar⁺ sputtering up to 300 eV and subsequent heating in air. Sputtering breaks up the graphite interatomic bonds at certain locations. At these locations the graphite oxidizes at, for example, 500°C in air. Up to three layer deep holes (1 layer=0.34 nm) can be obtained by this technique. The diameter of the pits can be controlled by the annealing time and temperature. Thus, also pits with diameters as large as the QDs can be created. A more detailed introduction into nanopit formation can be found in [79,80]. Unfortunately, the pits did not prevent the clusters from agglomeration and the tip-induced mobility again made STM imaging impossible. These results are shown in more detail in a previous work [67].

A possible reason for the tip-induced mobility on HOPG with nanopits could be that the pits are not deep enough. Therefore, deeper pits are desirable. Indeed, up to 6 layers deep holes can be prepared by 4 keV C₆₀ sputtering [81].

Up to 3–5 nm deep nanopits (9–15 layers) with \varnothing of 6–15 nm are prepared on a HOPG sample by Ralf Wellmann in the group of Prof. Dr. Manfred Kappes (Institute of Physical Chemistry, University of Karlsruhe, Germany) by C₆₀ sputtering. A STM image before cluster preparation is shown in Fig. 4.6(a). Unfortunately, even these deep nanopits did not prevent the InAs clusters ($\varnothing=5$ nm) from agglomeration and tip-induced mobility still disabled stable STM imaging. A typical STM image after cluster preparation is shown in Fig. 4.6(b). The InAs cluster agglomerates are easily pushed away during scanning and empty pits are left back. Note, that even for STM measurements at 2 V and 100 pA the tip-induced mobility is too strong.

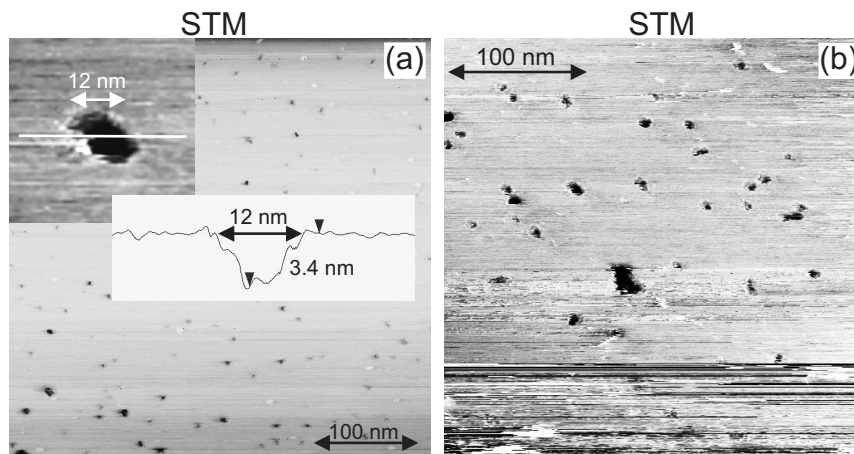


Figure 4.6: (a) STM on HOPG with 3–5 nm deep and 6–15 nm wide nanopits before cluster deposition (STM by Ralf Wellmann). (b) Tip-induced mobility of InAs clusters ($\varnothing=5$ nm) on HOPG: The agglomerates are pushed away during scanning and empty pits are left (air STM, PtIr tip, $I=333$ pA, and $V_{\text{sample}}=888$ mV).

Another air compatible substrate for STM is Au on mica. A Au film of 100 nm thickness is evaporated on mica with 1 Å/sec at a sample temperature of 300°C in HV (5×10^{-7} mbar). Afterwards, a post annealing for 2 h at 350°C is performed and the substrate is slowly cooled down at a rate of 3°C/min. This creates a flat Au surface with atomically high steps.

These Au on mica substrates are used for InAs cluster ($\varnothing=5$ nm) deposition. Figure 4.7(a) shows a tmAFM image of a Au on mica sample covered with InAs cluster agglomerates. In contrast to HOPG, STM imaging in air is possible on this sample (b) but with a low image quality. Tip-induced mobility is again present, and a lot of tip changes occur during scanning. Figure (b), although of pure quality, is the best case. Note, that for $V_{\text{sample}} < 2$ V or $I > 300$ pA the imaging of the agglomerates is completely impossible. As well in tmAFM as in STM the agglomerates appear 4–6 nm high. This is comparable to the specified cluster \varnothing of 5 nm ($\pm 10\%$, size-selected solution) further supported by the previous high-resolution TEM measurements.

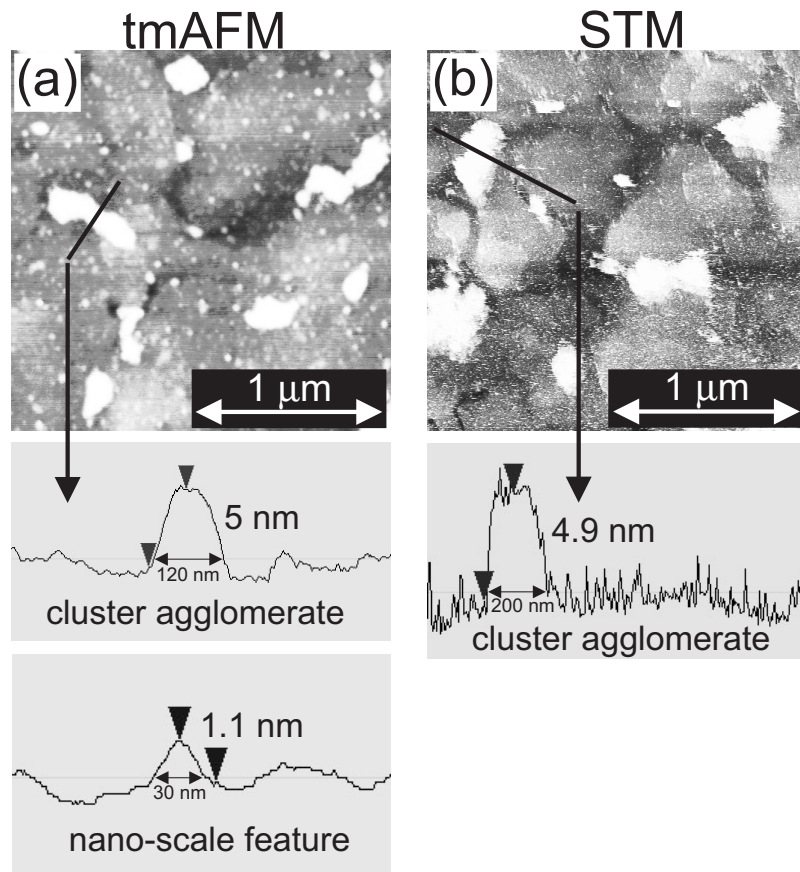


Figure 4.7: (a) tmAFM and (b) STM image (PtIr tip, air, $I=111$ pA, and $V_{\text{sample}}=2$ V) of InAs cluster ($\varnothing=5$ nm) agglomerates on Au. Down: line scans on the agglomerates of different sizes and on a smaller nano-scale feature (heights and widths are marked).

Note, that some small nano-scale features are visible in Fig. 4.7(a). They appear only 0.5–2 nm high. These features are also found on test samples where only a droplet of pure toluene is deposited. However, the cluster agglomerates appear only when clusters were actually prepared. Additionally, other pure solvents of different grade (for analysis and for spectroscopy) were tested. Nano-scale features are always found, for example, in the case of ethanol, isopropanol, dichloroethane, methanol, and distilled water. They even appear when the Au is stored in air for longer than 1 day. This behavior is also reported in a former diploma thesis [82]. However, the data shown in Fig. 4.7 are obtained on freshly evaporated Au, which shows almost no additional features before exposure to the cluster solution. Sample storage in an Ar glove box is found to prevent the contamination of Au substrates on a time scale of months.

In [83] it is reported that contact AFM performed in water also reveals nano-scale features on Au. If the lowest force for AFM is used without losing contact to the surface, they found features of 0.4–6 nm height. At higher forces the additional features are not detected. When they reduce the force afterwards to the previous set point, the features reappear at the same position. If the features were pushed to the side at higher forces, they should be afterwards found at the rim of the scanning area, which is not the case. The explanation is that the features, at least in this experiment, are liquid and that the tip penetrates through them during scanning at higher forces. Note, that even when the features are imaged, a penetration of the tip into these features cannot be excluded.

In my case, tmAFM images nano-scale features reproducibly. However, STM sometimes shows these features and sometimes not. Figure 4.8 demonstrates this behavior. In tmAFM images, as shown for example in (a), nano-scale features always appear (height: 0.5–2 nm). In the STM image (b) these features are not imaged at all, while the STM image (c) resolves at least some features (0.5–2 nm high, marked with arrows). STM imaging of these nano-scale features is found to be irreproducible: Different tips show a different behavior even at the same tunneling parameters. The imaging of these features depends on the actual tip shape, V_{sample} , I , but also on the proportional and integral gains of the STM feedback.

In comparison to [83], I cannot rule out that the tip penetrates into the features in tmAFM and STM. I never observed such a disappearance and reappearance of these features, which is mentioned above. It is, however, not certain that the features found in this work are of the same kind as the ones reported in [83]. Thus, the exact origin of these features is still an open question.

If a clean Au sample is exposed to an 1,6-hexandithiol solution in ethanol, nano-scale features appear, too. In accordance with [76] discussed in section 4.1 no evidence for a vertical ordered SAM is found in the case of hexanedithiol on Au.

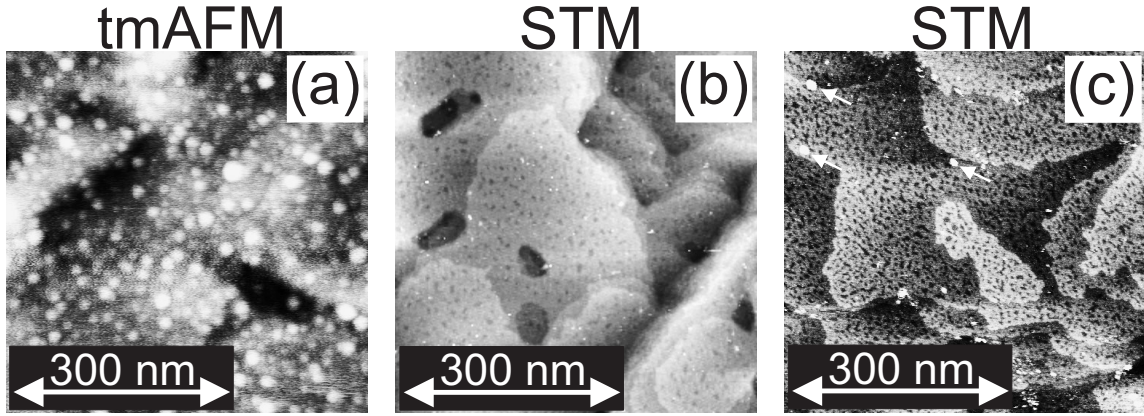


Figure 4.8: (a) Nano-scale features are always imaged with tmAFM (Au sample stored in air). Nano-scale features are sometimes and irreproducibly imaged with STM: (b) No additional features are imaged ($I=333$ pA, $V_{\text{sample}}=777$ mV, PtIr tip, hexanedithiol covered Au). (c) At least some features are imaged ($I=333$ pA, $V_{\text{sample}}=555$ mV, PtIr tip, hexanedithiol covered Au with InAs cluster $\varnothing=5$ nm). Note, that the features are 0.5–2 nm high and that they appear also on hexanedithiol samples without clusters (not shown).

In an early stage of this work the appearance of additional nano-scale features on test samples was not known. InP clusters were prepared on a hexanedithiol covered Au surface and the sample was inserted into the low temperature UHV STM (described in section 2.1.3). A lot of features were imaged with low temperature UHV STM. Note, that InP clusters and additional features cannot be certainly distinguished in this case. STS brings a little light into this problem. Indeed, peaks appeared in the conduction and valence band of the features studied (being InP clusters or not)³. Most of the measurements showed a band gap of about 4 eV, which is far too large to be interpreted as InP clusters even if the tip-induced band bending is considered. Only one exception out of five more or less reproducible measurements is found, where a band gap of 2.5 V is measured with STS. The data are shown in Fig. 4.9. The feature or cluster is shown in (a). It has a height of only 2 nm which is not compatible with the InP clusters \varnothing of 4–6 nm. The $I(V)$ and dI/dV data are shown in (b) and (c), respectively. The first peak of the conduction band at 1.3 V and the first peak of the valence band at -1.2 V are marked. If the tip-induced band bending is considered by 1D-Poisson calculations as explained in section 3.2, the true band gap can be deduced to 1.8 eV after reduction of a probably present charging energy of approximately 110 meV [70].

According to [58], 4–6 nm large clusters should have a band gap of 1.65–1.9 eV. Thus, the band gap deduced from the STS data can be related to an InP cluster. On the other hand, the band gap of 1.8 eV corresponds to a \varnothing of about 3.5–4.5 nm. Unfortunately, the measured height of 2 nm is much lower than the cluster diameter.

³Note, that the STS data were much less reproducible as the one obtained on strain-induced InAs QDs reported in section 3.3. Spatially resolved spectroscopy was impossible.

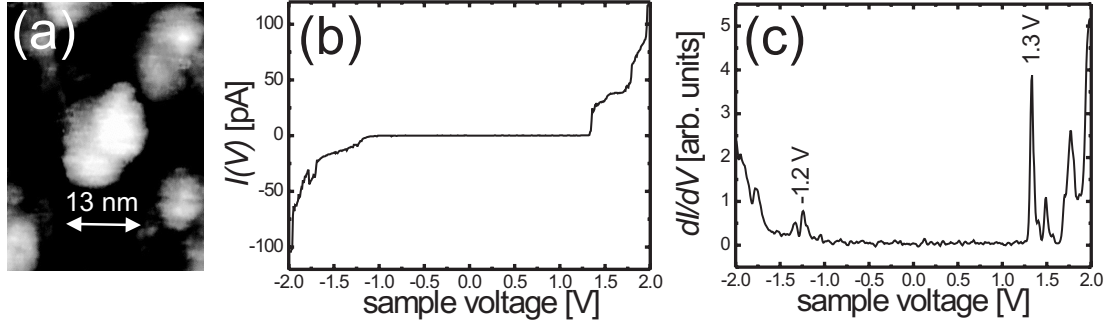


Figure 4.9: (a) STM image ($T=6$ K, PtIr tip, $V_{\text{sample}}=3$ V, $I=10$ pA) of a single InP cluster or other nano-scale feature (height=2 nm). (b) and (c) $I(V)$ and dI/dV curves taken above the feature or InP cluster, respectively ($V_{\text{stab}}=2$ V, $I_{\text{stab}}=100$ pA, and $V_{\text{mod}}=10$ mV).

Additionally, 3.5–4.5 nm is the cluster diameter without ligands, which are additive ≈ 0.5 nm long. Even if the ligands are bent away due to the tip forces or cluster-substrate interaction, at least 3.5–4.5 nm should be determined as height of the cluster, except if the cluster is positioned in a nanohole on the Au substrate.

This problem also appeared in [70–73]: Their STS data are in agreement with InAs clusters but the measured heights are also too low⁴. They claim that the reduced conductivity is responsible for the lower height, which is measured in constant-current images⁴. However, typical tip heights during tunneling are known to be about 0.5 nm. If it is assumed that the hexanedithiol is standing upwards with a height of ≈ 0.5 nm, the tip on the hexanedithiol covered Au substrate is at maximum 1 nm above the Au surface. Assuming additionally that the clusters are directly sitting on the Au and that the ligands are pushed away from the clusters at the Au contact as well as at the tip interface, a minimum apparent height of 3 nm remains for a \varnothing 4 nm cluster. This is, however, larger than the measured heights. The only explanation, as mentioned above, is that the clusters are lying in a hole of the substrate.

However, in the experiments of [70–73] the FWHM of linescans over the size-selected clusters fits nicely with the \varnothing obtained previously with TEM⁴.

In my case, the cluster (or nano-scale feature) of Fig. 4.9(a) has a FWHM of 7 nm. That does not fit so well to the \varnothing 3.5–4.5 nm deduced from STS. Yet again, it should be kept in mind that the FWHM strongly depends on the actual tip shape due to the convolution between tip and cluster.

⁴Private communication with Prof. Dr. Uri Banin (Department of Physical Chemistry, The Hebrew University, Jerusalem, Israel).

Summary

In conclusion, cluster preparation contaminates the surface with 0.5–2 nm high nano-scale features. These features even appear if the pure solvent is used in the preparation instead of the cluster solution. Thus, single clusters and nano-scale features cannot be reliably distinguished with STM and tmAFM. However, peaks are found in dI/dV curves in the conduction and valence bands above a single InP cluster (or a nano-scale feature) with low temperature UHV STS. The band gap is consistent with an InP cluster of 4 nm diameter while on the other hand the measured height is only 2 nm.

Additionally, InAs nanocrystal agglomerates are prepared from a toluene solution on a Au surface and are measured with STM and tmAFM in air. Hopefully, low temperature UHV STS will allow wave-function mapping on single QDs within the agglomerates in the future.

Chapter 5

Single-walled carbon nanotubes

In the previous chapters 3 and 4 zero-dimensional nanostructures (QDs) are analyzed. In this chapter the focus is on a one-dimensional nanostructure namely single-walled carbon nanotubes (SWCNTs). They are prepared by a laser evaporation technique by the group of Prof. Dr. Richard E. Smalley (Rice University, Houston Texas, USA). The preparation of individual SWCNTs from the raw material onto a Au surface as well as test measurements with tMAFM in air are shown in section 5.2. All results presented in this section are obtained in cooperation with Dr. Serge G. Lemay from the group of Prof. Dr. Cees Dekker (Department of Nanoscience and DIMES, Delft University of Technology, The Netherlands). Low temperature STM and STS measurements on these samples are reported in section 5.3. Atomic resolution is achieved with STM and a distinction between metallic and semiconducting tubes could be made by STS. Additionally, defect-induced QD states within a metallic nanotube are resolved. All results presented in this section are obtained in cooperation with Dr. André Kubetzka. In order to put the results into perspective, the basic properties of SWCNTs and a literature survey is given in section 5.1.

5.1 Basic properties

SWCNTs are prepared by the laser evaporation technique [84]. Co/Ni catalysts are used to create crystalline bundles of SWCNTs by graphite vaporization in an Ar atmosphere at 1200°C. A TEM image of a SWCNT bundle is shown in Fig. 5.1. Individual tubes within the bundle are visible. The extraction of individual nanotubes from these bundles is the main topic of section 5.2.

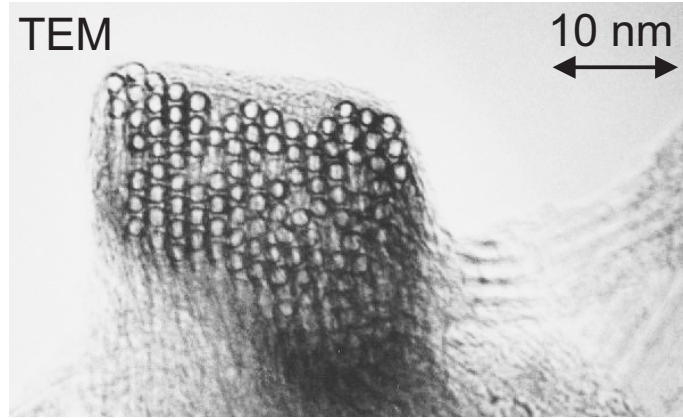


Figure 5.1: TEM image of a SWCNT bundle (taken from [84]).

A SWCNT is a graphene sheet which is rolled up into a cylinder. A graphene sheet consists of a hexagonal lattice of sp^2 -hybridized carbon. Each carbon atom bonds to its three neighbors via sp^2 σ -bonds, while the fourth electron is in a π -orbital perpendicular to the plane. The hexagonal graphene lattice is shown in Fig. 5.2. Two zigzag directions forming an angle of 60° and an armchair direction are marked. Any vector \vec{C} can be marked with two indices (n, m) :

$$\vec{C} = n\vec{a}_1 + m\vec{a}_2 \quad (5.1)$$

where \vec{a}_1 and \vec{a}_2 are the unit vectors marked in Fig. 5.2.

Additionally, (n, m) can be used to identify the geometry of SWCNTs. For example, a $(10,5)$ nanotube is obtained if we cut the graphene sheet two times perpendicular to \vec{C} at $(0,0)$ and $(10,5)$ and roll it up along \vec{C} . If $n = m$, tubes are called armchair, if $m = 0$ zigzag, and any other (n, m) are referred to as chiral SWCNTs. Note, that the so-called chiral angle Φ between \vec{C} and the armchair direction is given by:

$$\Phi = \arccos \frac{\sqrt{3}(n+m)}{2\sqrt{n^2+m^2+nm}} \quad (5.2)$$

while the diameter of the SWCNT can be calculated from:

$$d = \frac{a}{\pi} \sqrt{n^2 + m^2 + nm} \quad (5.3)$$

where $a=0.246$ nm is the lattice constant (the C-C distance in graphene is 0.142 nm). A model for an armchair, zigzag and chiral SWCNT can be found in Fig. 5.3. Note, that the chiral SWCNT of Fig. 5.3(c) is the same as the one discussed in Fig. 5.2.

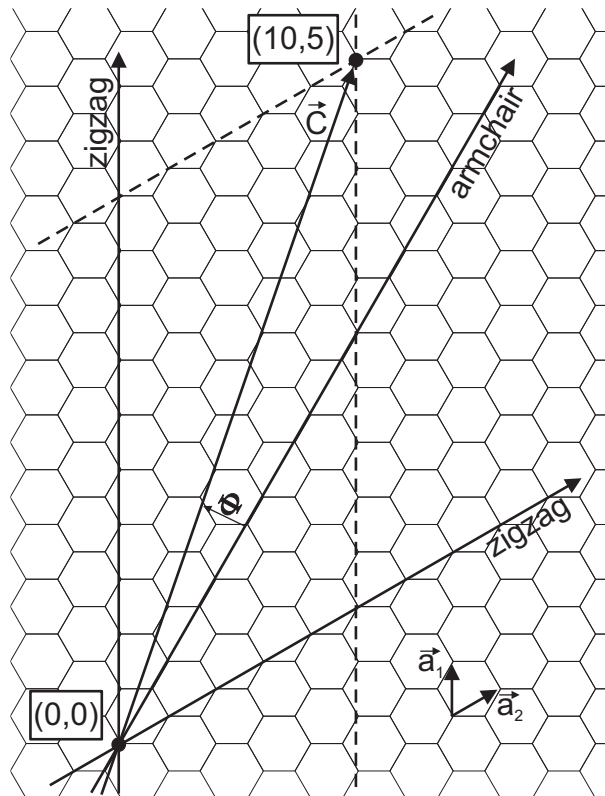


Figure 5.2: Graphene sheet with crystallographic directions marked in the figure. Unit vectors \vec{a}_1 and \vec{a}_2 of the hexagonal graphene sheet are marked.

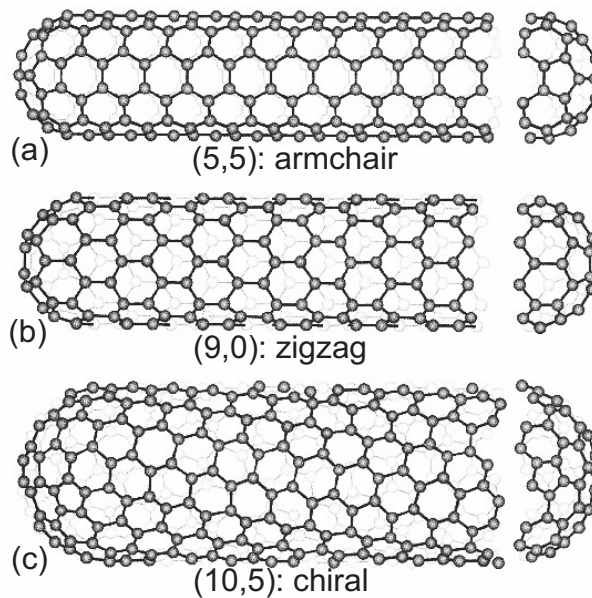


Figure 5.3: Models of SWCNTs (taken from [85])

The two-dimensional band structure of graphene (tight-binding calculation [86]) is shown in Fig. 5.4(a). The valence band ($E < 0$) is connected to the conduction band ($E > 0$) at 6 points in k -space. Therefore, graphene is called a zero-gap semiconductor or semi-metal.

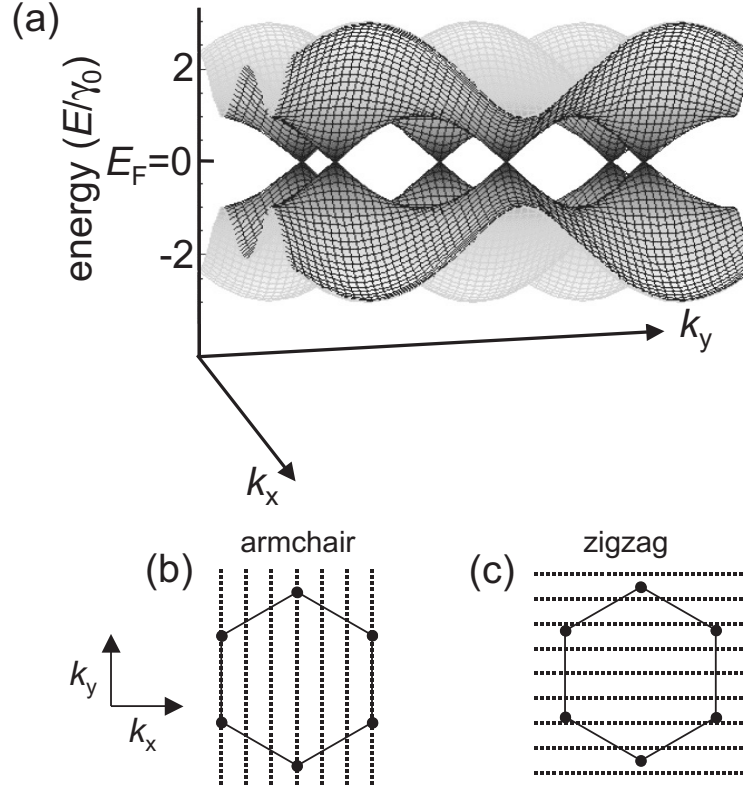


Figure 5.4: (a) Band structure of graphene (picture is taken from [86]). The conductivity of graphene depends on 6 points in k -space (γ_0 is the energy overlap integral between nearest neighbors). (b) and (c) Reciprocal space for an armchair and zigzag nanotube, respectively. The parallel dotted lines represent the allowed values of \vec{k} in a SWCNT.

The conductivity depends strongly on the 6 points in k -space at E_F . If the graphene is rolled up into a cylinder, an additional quantization appears in the circumferential direction: $\vec{k} \cdot \vec{C} = 2\pi q (q = 0, 1, 2, \dots)$. This additional quantization corresponds to parallel lines in k -space with an interline spacing of $\Delta k = \frac{2\pi}{|\vec{C}|} = \frac{2}{d}$. The line direction corresponds to the tube direction and depends on the chiral angle Φ . This is shown for an armchair and zigzag SWCNT in Fig. 5.4(b) and (c), respectively. The dotted lines mark the allowed k -values for the SWCNT. If the lines cross one of the 6 points in k -space the SWCNT is metallic, otherwise it is semiconducting. Thus, all armchair SWCNTs are conductive.

In general, there is a simple rule: If

$$(n - m)/3 = \text{integer}, \quad (5.4)$$

it is a metallic SWCNT, otherwise it is a semiconducting one. Consequently, two out of three SWCNTs should be semiconducting.

Both the metallic and the semiconducting SWCNTs are considered promising candidates for molecular electronics [9]. They can be used as ultra small wires and even as transistors in source-drain-gate configuration [11]. It is therefore highly desirable to understand their electronic properties in detail. In particular, the effect of defects on transport properties must be understood and is currently under debate. A literature survey is given here: Early experiments generally assumed ballistic transport in SWCNTs. The mean free path in individual as well as in bundles of metallic SWCNTs appeared to be restricted only by the contacts [87–89]. Later experiments found evidence for defects in semiconducting SWCNTs by using an AFM tip to locally change the transport properties of the tube [90]. Theoretical studies explained both results by stating that all defects larger than the lattice constant do not lead to backscattering within metallic tubes, whereas backscattering is present in semiconducting tubes [91,92].

More recently, low-temperature transport measurements using individual metallic SWCNTs have been interpreted in terms of disorder-induced quantum dots [93,94]. This behavior is shown in Fig. 5.5. The source-drain differential conductance $dI/dV_{sd}(V_{sd})$ is shown gray scaled as a function of V_{sd} and the gate voltage V_g . At the gate voltage region A and C the defects appear transparent, while in region B strong electron scattering is found. This leads to a defect-induced QD within the SWCNT, which shows the typical Coulomb blockade pattern. A QD state within an extended SWCNT obviously requires scattering at defects.

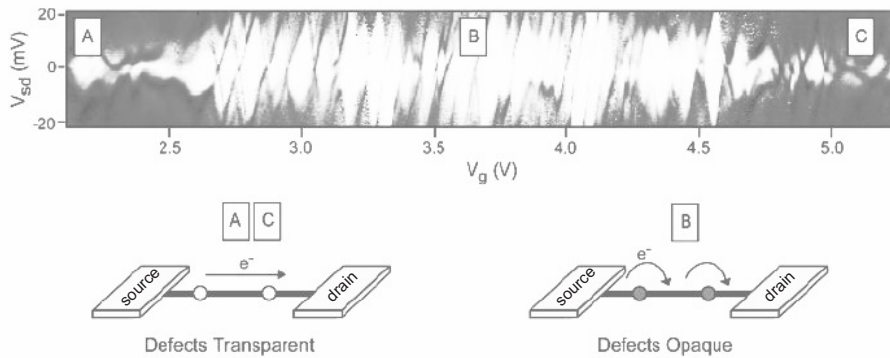


Figure 5.5: Defect-induced QD within a 250 nm long metallic SWCNT measured at 4 K in source-drain-gate configuration (taken from [93]). The gray-scaled plot (white corresponds to zero conductance) of the source-drain differential conductance $dI/dV_{sd}(V_{sd})$ as a function of V_{sd} and V_g (applied from the bottom) shows a Coulomb blockade pattern in region B. In region A and C the defects appear transparent.

According to theory, a corresponding backscattering could originate from certain arrangements of vacancies [95]. Figure 5.6 shows such vacancies for a metallic armchair nanotube schematically. Let N_A and N_B be the number of removed atoms at A and B lattice points (marked in the figure), respectively. The difference is defined as $\Delta N_{AB} = N_A - N_B$. Numerical results show, that the conductance vanishes for $|\Delta N_{AB}| \geq 2$, and that the conductance is quantized into one and two times $e^2/\pi\hbar$ for $|\Delta N_{AB}| = 1$ and 0, respectively [95]. Note, that $2 \times e^2/\pi\hbar$ corresponds to perfect transmission. Consequently, the vacancy of Fig. 5.6(a) results in a reduced conductance of $1 \times e^2/\pi\hbar$. In the case of (b) a perfect transmission appears and in the case of (c) and (d) the conductance vanishes. Note, that defects larger than the lattice constant do not have any backscattering according to theory [95], thus, backscattering can exclusively arise from defect constellations as in (a), (c), and (d).

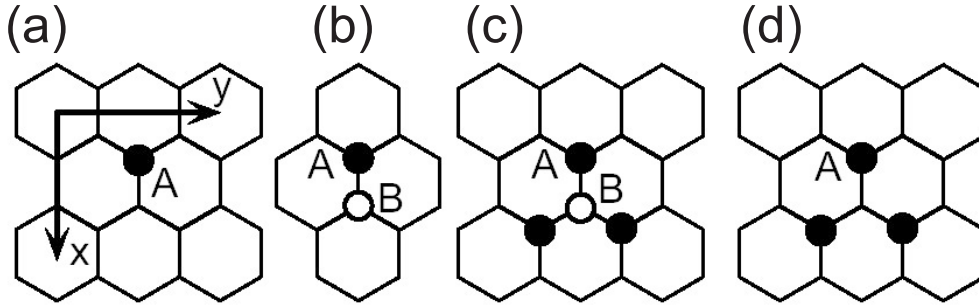


Figure 5.6: Schematic illustration of vacancies in armchair nanotubes (taken from [95]). The tube direction is y . Vacancies on A (B) lattice sites are represented by black (white) spots.

STM and STS can directly probe a defect-induced QD within extended metallic SWCNTs. This is shown in section 5.3. At first, however, a scanning probe adequate preparation technique of the SWCNTs has to be realized. This is the topic of the next section.

5.2 Sample preparation

A photo of the raw SWCNT material is shown in Fig. 5.7(a). Individual SWCNTs are obtained by sonicating the raw material in dichloroethane [96]. A clear gray colored solution results. A droplet of this solution is deposited on a Au or HOPG substrate. Afterwards, the substrate is blown dry with N_2 . TmAFM can resolve individual (height < 1.4 nm) and bundles of SWCNTs. This is shown in the case of a Au on mica substrate in (b) and (d), and for HOPG in (c). Note the ring formation of a nanotube bundle visible in (b). Similar ring formations are reported in the literature [97–101], but in this work they appear only seldom and are not further analyzed.

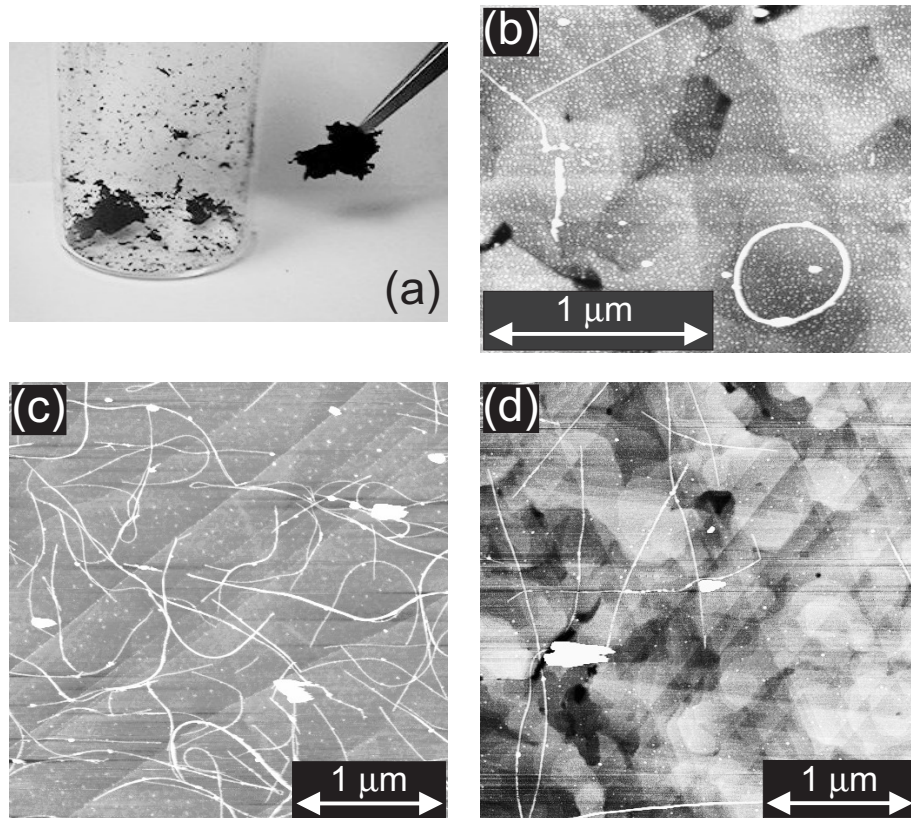


Figure 5.7: (a) Photo of the raw SWCNT material (taken from [85]). (b) and (d) SWCNTs deposited on Au on mica and measured with tMAFM. (c) SWCNTs on HOPG imaged with tMAFM.

Unfortunately, STM imaging was impossible for SWCNTs on graphite due to a strong tip-induced mobility. This behavior on HOPG substrates is similar to the one reported in section 4.2. Tip-induced mobility disabled imaging of cluster agglomerates there. On the other hand, the cluster agglomerates could be imaged with STM when deposited on Au. The same is true here: STM in air and in UHV at low temperatures can reproducibly image SWCNTs on Au. Therefore, Au on mica samples were prepared and glued with Thermostix3000 on the STM sample holder. Bond wires make the electrical contact. This is done, because conductive glues contaminate the samples with dirt (as seen by tMAFM). Although the sample is prepared in air, STM images could reveal atomic resolution at low temperatures and even reproducible STS spectra could be obtained on the SWCNTs. This is the topic of the next section.

5.3 STS results: Defect-induced confined states

An UHV ($p < 10^{-10}$ mbar) low temperature ($T=14$ K) STM system, which is described in [26], is used to image SWCNTs. Bundles are not considered in this thesis. A zoom into an individual SWCNT with atomic resolution is shown in Fig. 5.8. The raw data in (a) show an angle of 70° between the two zigzag directions. This is demonstrated in (b). Since the angle between these rows is known to be 60° , a tip-convolution effect must be responsible. A simple image processing program can correct this angle to the expected 60° . Therefore, the image was compressed perpendicular to the nanotube direction. This is shown in (c). Only afterwards the correct chiral angle of 13.7° can be deduced from the image with an error of $\pm 0.5^\circ$. This procedure was adapted from [102].

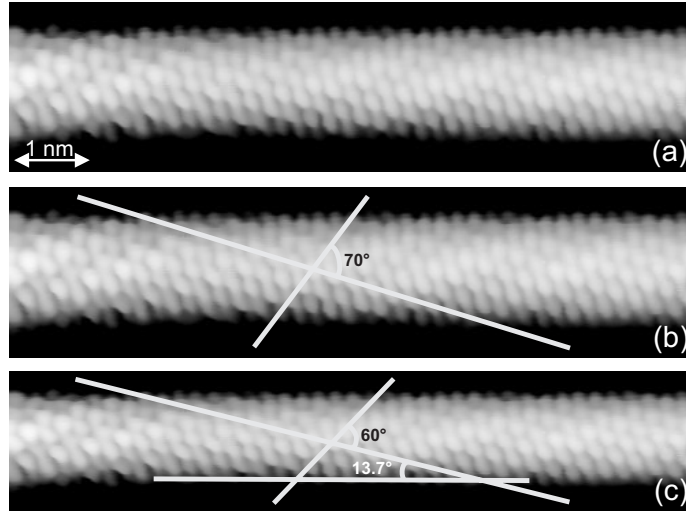


Figure 5.8: (a) Atomically resolved STM image of a SWCNT (W tip, $T=14$ K, $I=1$ nA, $V_{\text{sample}}=-50$ mV, raw data). (b) Due to tip convolution the two zigzag directions form a wrong angle of 70° . (c) Correction with an image processing program to the correct angle of 60° . The chiral angle Φ is determined to be $13.7^\circ \pm 0.5^\circ$.

Altogether, three main features can be deduced from the STM and STS measurements of this SWCNT: (i) STS shows that this SWCNT is metallic (spectra on metallic and semiconducting tubes will be discussed later). (ii) From corrected STM images a chiral angle of $13.7^\circ \pm 0.5^\circ$ is obtained, and (iii) the apparent height of the tube is determined to be 1.2–1.3 nm. Note, that the actual SWCNT diameter can be expected to be 0.2–0.4 nm larger than the measured value, because the tip forces (also present in STM) are known to bend the tube downwards during scanning [102].

Based on these informations we can determine the (n, m) of this SWCNT as is shown in Fig. 5.10. The zigzag and armchair directions are marked. Two lines with 13.2° and 14.2° from the armchair direction are drawn. All possible convolution points for a SWCNT are marked (black points: metallic tubes; gray points: semiconducting tubes). Considering a diameter d of 1.5 nm and a chiral angle of 13.9° , only the $(15,6)$ geometry remains possible. The others are too small, too large, or semiconducting.

As already reported in the literature [102], only every second atom of the SWCNT carbon lattice is imaged with STM. This is also shown in Fig. 5.10 and the measured STM image is inserted for comparison (correct angle but different scale).

Besides atomic resolution, reproducible STS data are obtained on individual SWCNTs. This is exemplified in Fig. 5.9. Note, that the measured dI/dV is proportional to the LDOS as described in section 2.1.2. A non-zero LDOS at E_F is characteristic for a metallic SWCNT (a), whereas a band gap is found in the case of a semiconducting tube (b). The metallic tube (a) shows a large subband separation of about 2 eV while the semiconducting tube (b) has a small band gap of about 0.74 eV. Similar values are reported in [96].

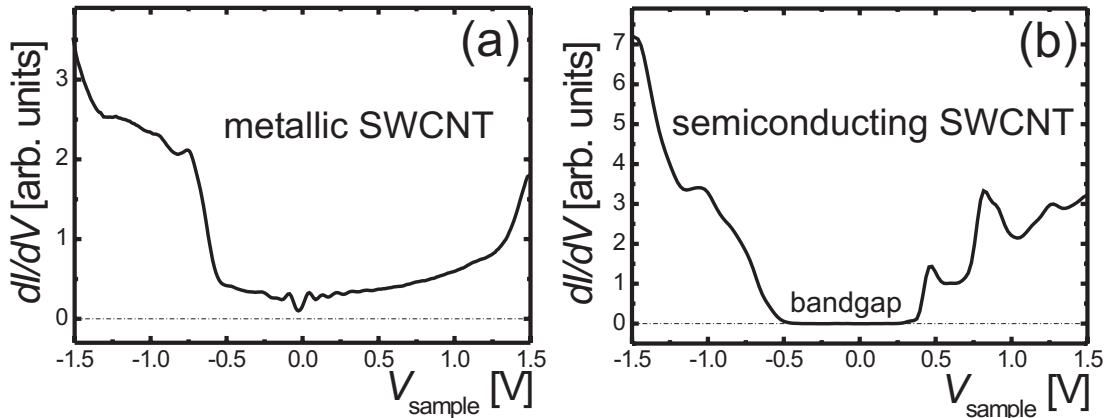


Figure 5.9: STS data taken on (a) a metallic (W tip, $T=14$ K, $I=300$ pA, and $V_{\text{stab}}=1.5$ V) and (b) a semiconducting (W tip, $T=14$ K, $I=500$ pA, and $V_{\text{stab}}=1.5$ V) individual SWCNT.

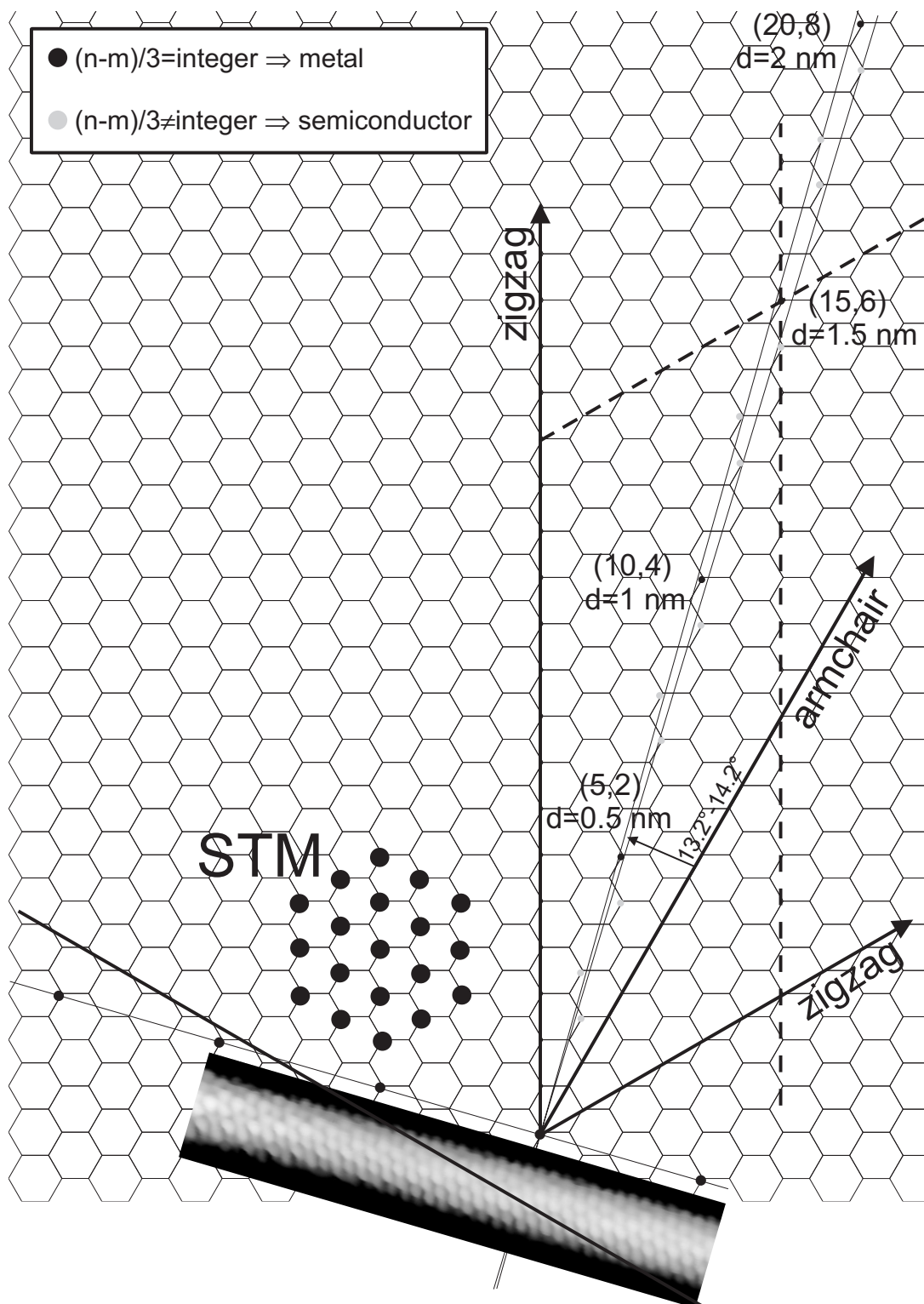


Figure 5.10: (15,6) determination of the SWCNT shown in Fig. 5.8. STM image of the SWCNT is inserted with right angle but different scale for comparison.

A new result of this study is the observation of oscillations close to the Fermi energy E_F ($V_{\text{sample}}=0$ V) on the metallic SWCNT of Fig. 5.9(a). In addition to a dip at E_F , nearly equidistant peaks are found as shown more clearly in Fig. 5.11(c). The features look like a damped oscillation starting at E_F with a period of about 87 meV. Note, there is no tip-induced band bending in this case, because the Au substrate as well as the SWCNTs are metallic. The data are recorded at the position marked in (a). At another position of the tube also marked in (a) the energy difference between the peaks is different, for example, about 38 meV as shown in (b). This change in periodicity appears quite abruptly at the dotted line in (a). To demonstrate this, the spatially resolved dI/dV signal at the energy of the 46 mV peak of (c) is shown in (d). It clearly reveals that the 46 mV peak is restricted to an area of 25 nm on the right-hand side of the dotted line.

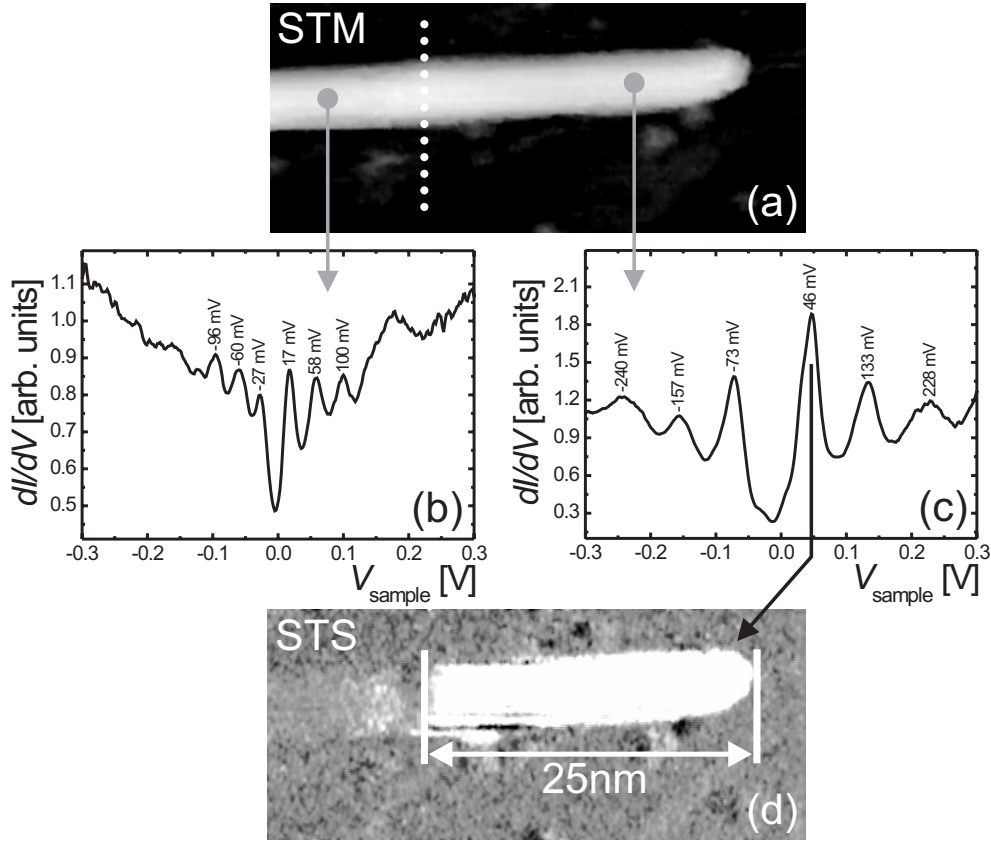


Figure 5.11: (a) STM image of a SWCNT end (W tip, $T=14$ K, $I=300$ pA, $V_{\text{sample}}=46$ mV, $45\text{ nm}\times 19\text{ nm}$). (b) STS data on the left-hand side of the dotted line in (a). (c) STS data on the right-hand side of the dotted line in (a) (zoom of the STS data shown in Fig. 5.9(a) into the region close to E_F). All STS data in (b) and (c) are taken with $V_{\text{stab}}=-300$ mV, $I_{\text{stab}}=300$ pA, and $V_{\text{mod}}=3$ mV. (d) Simultaneously recorded spatially resolved STS image ($V_{\text{stab}}=46$ mV [first peak in (c)], $I_{\text{stab}}=300$ pA, and $V_{\text{mod}}=10$ mV).

Peaks in the LDOS restricted to a certain area are strong indications for confined states. Confined states have previously been found by STS only after shortening individual SWCNTs [103, 104]. However they have never been reported on extended tubes. In the present case, the tube has a length of over 2000 nm. In order to verify that the peaks are indeed confined states, one can calculate whether the peak separation ΔE is consistent with the size of the confined region. Therefore the approximate formula [103]:

$$\Delta E = hv_F/2L \quad (5.5)$$

with $v_F = 8 * 10^5$ m/sec being the Fermi velocity is used. For $\Delta E_1=87$ meV and $\Delta E_2=38$ meV we get $L_1=19$ nm and $L_2=44$ nm, respectively. L_1 agrees approximately with the measured 25 nm restriction length of the 46 mV peak. Thus, the observed peaks close to E_F can be assigned to confined states within the SWCNT.

Confinement in an extended tube obviously requires scattering. The type of scatterer could not be identified precisely. A significant bending of the nanotube at the end of the confined region can be ruled out from STM images. There is no step edge in the metallic substrate below the tube at this position (only one at a distance of approximately 10 nm). This is shown in Fig. 5.12(a) where the contrast is chosen to make the monoatomic steps on Au visible. Note, that some nano-scale features are visible. They appear reproducibly as the ones reported in section 4.2.

Two linescans are marked in (a) and shown in (b) and (c). Only a small elevation of 0.7 Å at the scattering point is visible in (b). Thus, a large contaminant can be ruled out. In (c) one sees that the nanotube follows the morphology of the substrate. Anyhow, the scatterer is not at the step position of the substrate. The data therefore suggests that the scattering center leading to the confined states is most likely intrinsic.

Regardless of their exact nature, the data directly shows that localized defects can lead to significant backscattering. According to theory, only certain arrangements of vacancies can explain a corresponding backscattering, though extended defects should not show any backscattering at all [95]. The backscattering at vacancies is discussed in section 5.1. Backscattering has a strong influence on the transport properties of the tube: It modifies the LDOS near the Fermi level and decreases the transmittance of individual modes. The effect of two partly transmitting barriers on the transport properties of SWCNTs has been measured by Liang *et al.* [105], and was described in terms of Fabry-Perot-like electron modes in the nanotube. Pursuing this analogy, the energy- and position-dependent LDOS measurements reported here amount to spatial maps of these Fabry-Perot modes, with defect sites playing the role of the reflecting barriers.

Thus, the present experiment can give an explanation of the discrepancies in transport experiments, which are reported in section 5.1: The defects are randomly distributed within the SWCNT. If the source-drain contact envelopes a defect free tube part, no backscattering is measured. A QD within a quantum wire is found, if two opaque defects are present as in the case of [93] shown in Fig. 5.5.

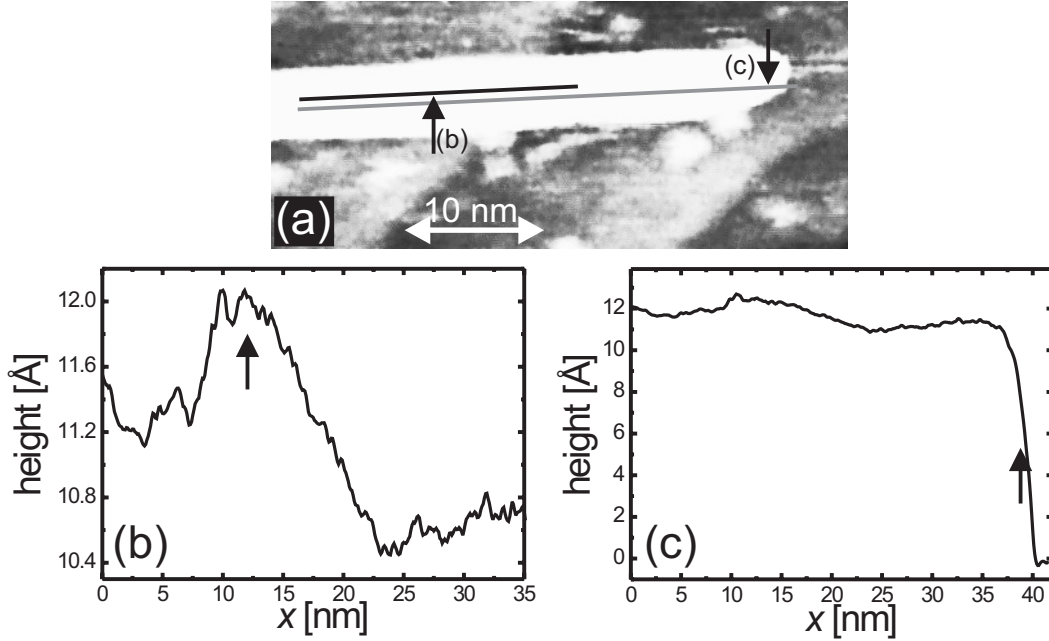


Figure 5.12: (a) Same STM image as in Fig. 5.11(a) with a different black/white contrast. (b) and (c) Linescans along the paths marked in (a). The arrows in (b) and (c) are at the positions marked in (a).

It should be mentioned that in some transport experiments the electrical conductivity seems to occur coherently over much longer distances than the defect separations. For example in [87] it is found that the current flows coherently over discrete electron states of at least 140 nm extension, which was the contact-to-contact distance. Additionally, they deduced from their data that the coherence extends even over the full tube length of $3\mu\text{m}$. In contrast, a defect-to-defect separation of only 20–40 nm is measured here. The higher defect density observed in this study could be caused by the sonification procedure of the raw material. It was found that the tubes were broken into segments at too high sonification powers or too long sonification times. Therefore it seems plausible that the sonification may create intrinsic defects in tubes.

Another point, which requires some discussion, are the peak widths of Figs. 5.11(b) and (c). Since no peaks are found at E_F , the remaining dI/dV magnitude appears to be related to the widths of the surrounding peaks. These widths are much larger than the predicted energy resolution of the experiment [106]:

$$\delta E = \sqrt{(3.3 \cdot kT)^2 + (2.5 \cdot V_{\text{mod}})^2} = 8.5 \text{ meV}.$$

For comparison, the FWHM of the 46 meV peak is 47 meV. The peak widths increase with increasing distance from E_F suggesting lifetime effects guided by electron-electron interaction. A simple broadening by the transition of the electrons into the Au substrate would usually not be symmetric around E_F because the single-electron states at positive V_{sample} are less strongly confined than the states at negative V_{sample} . Electron-phonon interaction in SWCNTs is known to be weak [107]. Thus, only electron-electron interaction remains as a possible cause.

The same magnitude and energy dependence of the peak widths are also observed for shortened SWCNTs [108]. A similar, even higher, lifetime broadening in SWCNTs can be deduced from the phase coherence of scattered electron waves observed by STM [109]. They report, for example, at a wave vector $k = 7.45 \text{ 1/nm}$ a coherence length of $l = 1.82 \text{ nm}$, resulting in:

$$\Delta E \geq \frac{\hbar}{2\tau} = \frac{\hbar v}{2l} = \frac{\hbar^2 k}{2lm} = 157 \text{ meV}.$$

In contrast, time-resolved photoemission data of SWCNT revealed an electron lifetime close to E_F which corresponds to a broadening of only 4 meV due to electron-electron interaction [110]. Since the SWCNTs used in all STM measurements are directly deposited on a Au substrate, which is not the case for the bucky paper samples used for photoemission experiments, it might be that lifetime effects in SWCNTs depend significantly on the substrate.

Summary

Individual SWCNTs are prepared on Au substrates and imaged with tmAFM in air. With low temperature UHV STM atomic resolution is obtained and the (n, m) values are determined. Additionally, metallic and semiconducting tubes are identified with STS. A new result of this study is the observation of confined states in an extended, individual, and metallic SWCNT with STS. Thus, direct evidence for backscattering is found in metallic tubes.

An atomic-scale identification of the scatterer will be an interesting goal for the future.

Chapter 6

Summary and outlook

Quantum dots (QDs) of InAs, nanocrystals of InAs, InP, and CdSe, and single-walled carbon nanotubes (SWCNTs) are prepared for and analyzed with low temperature UHV STM and STS and, additionally, with AFM in air. The following results are obtained:

Wave-function mapping is realized with STS on freestanding strain-induced InAs QDs, which are grown by MBE and transferred within UHV to the STM system. The number of nodes in $[1\bar{1}0]$ direction is larger than the number of nodes in $[110]$ direction. This effect is attributed to shape asymmetry of the QDs, which are elongated in $[1\bar{1}0]$ direction. However, the shape asymmetry cannot completely explain the experimental results.

The influence of an oxide layer is analyzed by SCM and conductive AFM in air. The conductance and the capacitance are larger above the oxidized QDs than above the oxidized wetting layer. This effect is attributed to a different Fermi level pinning between oxidized wetting layer and oxidized InAs QDs.

InAs nanocrystal agglomerates are prepared from solution on a Au substrate and are measured in air with STM. Unfortunately, wave-function mapping could not be realized so far on nanocrystals which are synthesized by colloidal chemistry.

In contrast to the two QD systems described above, SWCNTs are one-dimensional quantum wires. Confined states are resolved by STS in an extended, individual, and metallic SWCNT. Thus, direct evidence for backscattering is found in metallic tubes.

In the future, the experiments can be continued in the following directions:

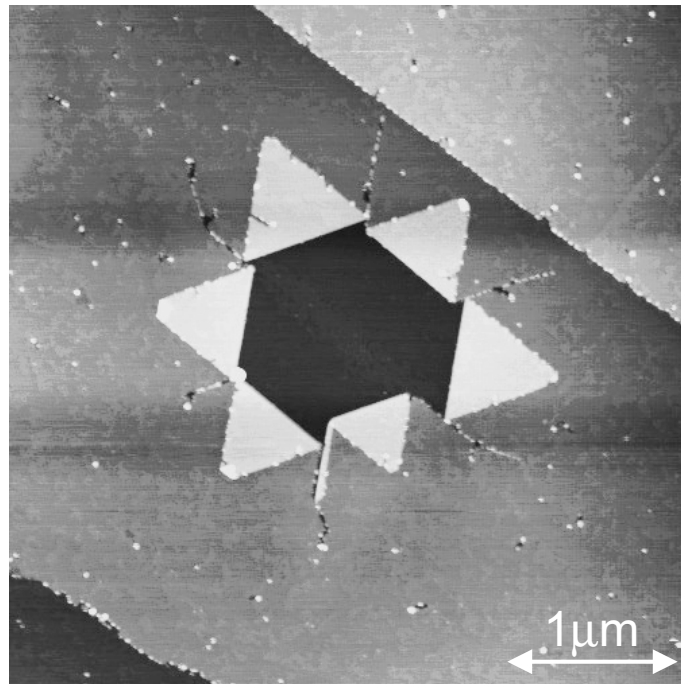
If InAs QDs are grown on AlAs instead of GaAs, they should exhibit more quantized states due to the higher band offset between InAs and AlAs compared to InAs and GaAs. Additionally, a wave-function mapping of the valence band states should be possible, if the InAs QDs are grown on p-doped substrates. After completion of the low temperature UHV scanning capacitance microscope (SCM), single-electron states in individual dots could also be measured by SCM.

Clusters, which are synthesized by colloidal chemistry, are also QDs with single-electron states. Consequently, wave-function mapping with STS should also be possible. I am afraid that the cluster agglomerates, presented in section 4.2, are still not adequate, since stable imaging was not possible with STM under ambient conditions.

I propose to further improve the preparation, or to try other preparation procedures, for example, a direct deposition of the cluster solution in UHV with a pulse valve.

The nature of the defects in SWCNTs can be further analyzed with STM and complementary with non-contact AFM. This work is currently under way.

Additionally, STS and spin-polarized STS should resolve the pure charge-density wave and the superposition of charge- and spin-density wave in nanotubes, respectively, as proposed by Luttinger–Tomonaga liquid theory [89, 111, 112]. Therefore, the nanotubes have to be separated from the surface in order to avoid screening of the Coulomb interaction of the electrons within the tube.



Nanostar: This tmAFM image is obtained on a HOPG sample with nanopits, prepared by Ralf Wellmann in the group of Prof. Dr. Manfred Kappes (Institute of Physical Chemistry, University of Karlsruhe, Germany). The star is created during cleavage of the HOPG substrate. The small white features originate from the solvent preparations as discussed in section 4.2.



Bibliography

- [1] Y. Qiu, P. Gogna, S. Forouhar, A. Stintz, L. F. Lester: *High-performance InAs quantum-dot lasers near 1.3 μm* . Appl. Phys. Lett. **79**, 3570 (2001).
- [2] C. Ribbat, R. L. Sellin, I. Kaiander, F. Hopfer, N. N. Ledentsov, D. Bimberg, A. R. Kovsh, V. M. Ustinov, A. E. Zhukov, M. V. Maximov: *Complete suppression of filamentation and superior beam quality in quantum-dot lasers*. Appl. Phys. Lett. **82**, 952 (2003).
- [3] P. Michler, A. Kiraz, C. Becher, W. V. Schoenfeld, P. M. Petroff, L. Zhang, A. I. E. Hu: *A quantum dot single-photon turnstile device*. Science **290**, 2282 (2000).
- [4] S. Coe, W. K. Woo, M. Bawendi, V. Bulović: *Electroluminescence from single monolayers of nanocrystals in molecular organic devices*. Nature **420**, 800 (2002).
- [5] M. T. Harrison, S. V. Kershaw, M. G. Burt, A. L. Rogach, A. Kornowski, A. Eychmüller, H. Weller: *Colloidal nanocrystals for telecommunications. Complete coverage of the low-loss fiber windows by mercury telluride quantum dots*. Pure Appl. Chem. **72**, 295 (2000).
- [6] M. Bruchez, M. Moronne, P. Gin, S. Weiss, A. P. Alivisatos: *Semiconductor nanocrystals as fluorescent biological labels*. Science **281**, 2013 (1998).
- [7] M. S. Dresselhaus, G. Dresselhaus, P. C. Eklund: *Science of fullerenes and carbon nanotubes*. Academic Press Inc., San Diego (1996).
- [8] R. Saito, G. Dresselhaus, M. S. Dresselhaus: *Physical properties of carbon nanotubes*. Imperial College Press (1998).
- [9] C. Dekker: *Carbon nanotubes as molecular quantum wires*. Physics Today **52**, 22 (1999).
- [10] R. H. Baughman, A. A. Zakhidov, W. A. de Heer: *Carbon nanotubes—the route toward applications*. Science **297**, 787 (2002).
- [11] A. Javey, J. Guo, Q. Wang, M. Lundstrom, H. Dai: *Ballistic carbon nanotube field-effect transistors*. Nature **424**, 654 (2003).

-
- [12] Z. Yao, C. L. Kane, C. Dekker: *High-field electrical transport in single-wall carbon nanotubes*. Phys. Rev. Lett. **84**, 2941 (2000).
- [13] N. de Jonge, Y. Lamy, K. Schoots, T. H. Oosterkamp: *High brightness electron beam from a multi-walled carbon nanotube*. Nature **420**, 393 (2002).
- [14] K. Jiang, Q. Li, S. Fan: *Spinning continuous carbon nanotube yarns*. Nature **419**, 801 (2002).
- [15] R. Wiesendanger: *Scanning probe microscopy and spectroscopy. Methods and applications*. Cambridge University Press (1994). ISBN 0-521-42847-5.
- [16] C. J. Chen: *Introduction to scanning tunneling microscopy*. Oxford University Press (1993). ISBN 0-19-507150-6.
- [17] D. A. Bonnell (ed.): *Scanning tunneling microscopy and spectroscopy. Theory, techniques, and applications*. VCH Publishers (1993). ISBN 0-89573-768-X / 3-527-27920-2.
- [18] S. Gasiorowicz: *Quantum physics*. John Wiley & sons (1974). ISBN 0 471 29281 8.
- [19] D. Haude: *Rastertunnelspektroskopie auf der InAs(110)-Oberfläche: Untersuchung an drei-, zwei- und nulldimensionalen Elektronensystemen im Magnetfeld*. Thesis, Institute of Applied Physics, University of Hamburg, Germany (2001).
- [20] R. Dombrowski: *Aufbau eines Ultrahochvakuum-Tiefemperatur-Rastertunnelmikroskops mit rotierbarem Magnetfeld und magnetfeldabhängige Rastertunnelspektroskopie an der InAs(110)-Oberfläche*. Thesis, Institute of Applied Physics, University of Hamburg, Germany (1998).
- [21] C. Wittneven: *Aufbau eines Ultrahochvakuum-Tiefemperatur-Rastertunnelmikroskops mit drehbarem Magnetfeld und Untersuchung der Streuzustände ionisierter Dotieratome an InAs(110)*. Thesis, Institute of Applied Physics, University of Hamburg, Germany (1998).
- [22] J. Bardeen: *Tunneling from a many-partical point of view*. Phys. Rev. Lett. **6**, 57 (1961).
- [23] J. Tersoff, D. R. Hamann: *Theory and application for the scanning tunneling microscope*. Phys. Rev. Lett. **50**, 1998 (1983).
- [24] J. Tersoff, D. R. Hamann: *Theory of the scanning tunneling microscope*. Phys. Rev. B **31**, 805 (1985).
- [25] M. Morgenstern, D. Haude, V. Gudmundsson, C. Wittneven, R. Dombrowski, C. Steinebach, R. Wiesendanger: *Low temperature scanning tunneling spectroscopy on InAs(110)*. J. Electr. Spect. Rel. Phen. **109**, 127 (2000).

- [26] O. Pietzsch, A. Kubetzka, D. Haude, M. Bode, R. Wiesendanger: *A low-temperature ultrahigh vacuum scanning tunneling microscope with a split-coil magnet and a rotary motion stepper motor for high spatial resolution studies of surface magnetism*. Rev. Sci. Instr. **71**, 424 (1997).
- [27] C. Wittneven, R. Dombrowski, S. H. Pan, R. Wiesendanger: *A low-temperature ultrahigh-vacuum scanning tunneling microscope with rotatable magnetic field*. Rev. Sci. Instr. **68**, 3806 (1997).
- [28] J. Klijn: *Local density of states of the adsorbate-induced two-dimensional electron system studied at zero and strong magnetic fields*. Thesis, Institute of Applied Physics, University of Hamburg, Germany (2003).
- [29] F. J. Giessibl: *Advances in atomic force microscopy*. Rev. Mod. Phys. **75**, 949 (2003).
- [30] D. Bimberg, M. Grundmann, N. N. Ledentsov: *Quantum dot heterostructures*. John Wiley & Sons (1999). ISBN 0471973882.
- [31] J. Márquez, L. Geelhaar, K. Jacobi: *Atomically resolved structure of InAs quantum dots*. Appl. Phys. Lett. **78**, 2309 (2001).
- [32] Y. Hasegawa, H. Kiyama, Q. K. Xue, T. Sakurai: *Atomic structure of faceted planes of three-dimensional InAs islands on GaAs(001) studied by scanning tunneling microscope*. Appl. Phys. Lett. **72**, 2265 (1998).
- [33] E. E. Vdovin, A. Levin, A. Patané, L. Eaves, P. C. Main, Y. N. Khanin, Y. V. Dubrovskii, M. Henini, G. Hill: *Imaging the electron wave functions in self-assembled quantum dots*. Science **290**, 122 (2000).
- [34] A. Patané, R. J. A. Hill, L. Eaves, P. C. Main, M. Henini, M. L. Zambrano, A. Levin, N. Mori, C. Hamaguchi, Y. V. Dubrovskii, E. E. Vdovin, D. G. Austing, S. Tarucha, G. Hill: *Probing the quantum states of self-assembled InAs dots by magnetotunneling spectroscopy*. Phys. Rev. B **65**, 165308 (2002).
- [35] B. Grandidier, Y. M. Niquet, B. Legrand, J. P. Nys, C. Priester, D. Stiévenard, J. M. Gérard, V. Thierry-Mieg: *Imaging the wave-function amplitudes in cleaved semiconductor quantum boxes*. Phys. Rev. Lett. **85**, 1068 (2000).
- [36] O. Stier, M. Grundmann, D. Bimberg: *Electronic and optical properties of strained quantum dots modeled by 8-band $k\cdot p$ theory*. Phys. Rev. B **59**, 5688 (1999).
- [37] A. Bolz: *X-Ray diffraction on InAs quantum dots*. Thesis, Institute of Applied Physics, University of Hamburg, Germany (2003).
- [38] G. L. Snider, I. H. Tan, E. L. Hu: *Electron states in mesa-etched one-dimensional quantum well wires*. J. of Appl. Phys. **68**, 2849 (1990).

- [39] G. L. Snider: <http://www.nd.edu/~gsnider> .
- [40] I. Kegel, T. H. Metzger, A. Lorke, J. Peisl, J. Stangl, G. Bauer, J. M. García, P. M. Petroff: *Nanometer-scale resolution of strain and interdiffusion in self-assembled InAs/GaAs quantum dots*. Phys. Rev. Lett. **85**, 1694 (2000).
- [41] A. Bolz, C. Kumpf, C. Heyn, S. Schnüll, O. Bunk, F. Wu, A. Zolotaryov, A. Stahl, R. Kosuch, R. L. Johnson, W. Hansen: *Grazing-incidence x-ray diffraction on self-assembled InAs quantum dots in UHV*. HASYLAB Ann. Rep. **1**, 733 (2002).
- [42] G. Vincent, A. Chantre, D. Bois: *Electric field effect on the thermal emission of traps in semiconductor junctions*. J. of Appl. Phys. **50**, 5484 (1979).
- [43] C. M. A. Kapteyn, F. Heinrichsdorff, O. Stier, R. Heitz, M. Grundmann, N. D. Zakharov, D. Bimberg, P. Werner: *Electron escape from InAs quantum dots*. Phys. Rev. B **60**, 14265 (1999).
- [44] M. Grundmann, O. Stier, D. Bimberg: *InAs/GaAs pyramidal quantum dots: Strain distribution, optical phonons, and electronic structure*. Phys. Rev. B **52**, 11969 (1995).
- [45] A. J. Williamson, A. Zunger: *InAs quantum dots: Predicted electronic structure of free-standing versus GaAs-embedded structures*. Phys. Rev. B **59**, 15819 (1999).
- [46] L. R. C. Fonseca, J. L. Jimenez, J. P. Leburton, R. M. Martin: *Self-consistent calculation of the electronic structure and electron-electron interaction in self-assembled InAs-GaAs quantum dot structures*. Phys. Rev. B **57**, 4017 (1998).
- [47] M. Fricke, A. Lorke, J. P. Kotthaus, G. Medeiros-Ribeiro, P. M. Petroff: *Shell structure and electron-electron interaction in self-assembled InAs quantum dots*. Europhys. Lett. **36**, 197 (1996).
- [48] B. T. Miller, W. Hansen, S. Manus, R. J. Luyken, A. Lorke, J. P. Kotthaus, S. Huant, G. Medeiros-Ribeiro, P. M. Petroff: *Few-electron ground states of charge-tunable self-assembled quantum dots*. Phys. Rev. B **56**, 6764 (1997).
- [49] R. J. Warburton, B. T. Miller, C. S. Dürr, C. Bödefeld, K. Karrai, J. P. Kotthaus, G. Medeiros-Ribeiro, P. M. Petroff, S. Huant: *Coulomb interactions in small charge-tunable quantum dots: A simple model*. Phys. Rev. B **58**, 16221 (1998).
- [50] I. Tanaka, I. Kamiya, H. Sakaki, N. Qureshi, S. J. Allen, P. M. Petroff: *Imaging and probing electronic properties of self-assembled InAs quantum dots by atomic force microscopy with conductive tip*. Appl. Phys. Lett. **74**, 844 (1999).
- [51] H. U. Baier, L. Koenders, W. Mönch: *Oxidation of InAs(110) and correlated changes of electronic surface properties*. J. Vac. Sci. Technol. **B 4**, 1095 (1986).

- [52] T. K. Johal, R. Rinaldi, A. Passaseo, R. Cingolani, A. Vasanelli, R. Ferreira, G. Bastard: *Imaging of the electronic states of self-assembled $In_xGa_{1-x}As$ quantum dots by scanning tunneling spectroscopy*. Phys. Rev. B **66**, 075336 (2002).
- [53] B. T. Miller, W. Hansen, S. Manus, R. J. Luyken, A. Lorke, J. P. Kotthaus, G. Medeiros-Ribeiro, P. M. Petroff: *Fine structure in the spectrum of the few-electron ground states of self-assembled quantum dots*. Physica B **249-251**, 257 (1998).
- [54] L. Tröger: *Aufbau eines Tief-Temperatur-Rasterkraftmikroskops*. Thesis, Institute of Applied Physics, University of Hamburg, Germany (2001).
- [55] A. Born: *Nanotechnologische Anwendungen der Rasterkapazitätsmikroskopie und verwandter Rastersondenmethoden*. Thesis, Institute of Applied Physics, University of Hamburg, Germany (2000).
- [56] J. Isenbart, A. Born, R. Wiesendanger: *The physical principles of scanning capacitance spectroscopy*. Appl. Phys. A **72**, 243 (2001).
- [57] H. Yamamoto, T. Takahashi, I. Kamiya: *Local capacitance measurements on InAs dot-covered GaAs surfaces by scanning capacitance microscopy*. Appl. Phys. Lett. **77**, 1994 (2000).
- [58] A. A. Guzelian, J. E. B. Katari, A. V. Kadavanich, U. Banin, K. Hamad, E. Juban, A. P. Alivisatos, R. H. Wolters, C. C. Arnold, J. R. Heath: *Synthesis of size-selected, surface-passivated InP nanocrystals*. J. Phys. Chem. **100**, 7212 (1996).
- [59] A. A. Guzelian, U. Banin, A. V. Kadavanich, X. Peng, A. P. Alivisatos: *Colloidal chemical synthesis and characterization of InAs nanocrystal quantum dots*. Appl. Phys. Lett. **69**, 1432 (1996).
- [60] S. Haubold: *Synthese und Charakterisierung von III-V Halbleiter-Nanoclustern*. Thesis, Institute of Physical Chemistry, University of Hamburg, Germany (2000).
- [61] D. Talapin: *Experimental and theoretical studies on the formation of highly luminescent II-VI, III-V and core-shell semiconductor nanocrystals*. Thesis, Institute of Physical Chemistry, University of Hamburg, Germany (2002).
- [62] H. Weller: *Quantized semiconductor particles: A novel state of matter for materials science*. Adv. Mater. **5**, 88 (1993).
- [63] A. P. Alivisatos: *Perspectives on the physical chemistry of semiconductor nanocrystals*. J. Phys. Chem. **100**, 13226 (1996).
- [64] M. Tews, D. Pfannkuche: *Stark effect in colloidal indium arsenide nanocrystal quantum dots: Consequences for wave-function mapping experiments*. Phys. Rev. B **65**, 073307 (2002).

- [65] G. Ge, L. E. Brus: *Evidence for spinodal phase separation in two-dimensional nanocrystal self-assembly*. J. Phys. Chem. B **104**, 9573 (2000).
- [66] G. Ge, L. E. Brus: *Fast surface diffusion of large disk-shaped nanocrystal aggregates*. Nano Lett. **1**, 219 (2001).
- [67] T. Maltezopoulos: *Deposition von ligandenstabilisierten InAs-Clustern auf HOPG*. Thesis, Institute of Applied Physics, University of Hamburg, Germany (2000).
- [68] E. Rabani, D. R. Reichman, P. L. Geissler, L. E. Brus: *Drying-mediated self-assembly of nanoparticles*. Nature **426**, 271 (2003).
- [69] V. L. Colvin, A. N. Goldstein, A. P. Alivisatos: *Semiconductor nanocrystals covalently bound to metal surfaces with self-assembled monolayers*. J. Am. Chem. Soc. **114**, 5221 (1992).
- [70] U. Banin, Y. W. Cao, D. Katz, O. Millo: *Identification of atomic-like electronic states in indium arsenid nanocrystal quantum dots*. Nature **400**, 542 (1999).
- [71] O. Millo, D. Katz, Y. W. Cao, U. Banin: *Scanning tunneling spectroscopy of InAs nanocrystal quantum dots*. Phys. Rev. B **61**, 16773 (2000).
- [72] B. Alpers, I. Rubinstein, G. Hodes, D. Porath, O. Millo: *Energy level tunneling spectroscopy and single electron charging in individual CdSe quantum dots*. Appl. Phys. Lett. **75**, 1751 (1999).
- [73] O. Millo, D. Katz, Y. W. Cao, U. Banin: *Imaging and spectroscopy of artificial-atom states in core/shell nanocrystal quantum dots*. Phys. Rev. Lett. **86**, 5751 (2001).
- [74] E. P. A. M. Bakkers, Z. Hens, L. P. Kouwenhoven, L. Gurevich, D. Vanmaekelbergh: *A tunneling spectroscopy study on the single-particle energy levels and electron-electron interactions in CdSe quantum dots*. Nanotechnology **13**, 258 (2002).
- [75] D. Katz, O. Millo, S. H. Kan, U. Banin: *Control of charging in resonant tunneling through InAs nanocrystal quantum dots*. Appl. Phys. Lett. **79**, 117 (2001).
- [76] T. Y. B. Leung, M. C. Gerstenberg, D. J. Lavrich, G. Scoles, F. Schreiber, G. E. Poirier: *1,6-hexandithiol monolayers on Au(111): A multitechnique structural study*. Langmuir **16**, 549 (2000).
- [77] M. J. Esplandiú, H. Hagenström, D. M. Kolb: *Functionalized self-assembled alkanethiol monolayers on Au(111) electrodes: 1. Surface structure and electrochemistry*. Langmuir **17**, 828 (2001).

- [78] J. Pflaum, G. Bracco, F. Schreiber, R. Colorado, O. E. Shmakova, T. R. Lee, G. Scoles, A. Kahn: *Structure and electronic properties of CH₃- and CF₃-terminated alkanethiol monolayers on Au(111): A scanning tunneling microscopy, surface X-ray and helium scattering study.* Surf. Sci. **498**, 89 (2002).
- [79] H. Hövel, T. Becker, A. Bettac, B. Reihl, M. Tschudy, E. J. Williams: *Controlled cluster condensation into preformed nanometer-sized pits.* J. of Appl. Phys. **81**, 154 (1997).
- [80] S. M. Lee, Y. H. Lee, Y. G. Hwang, J. R. Hahn, H. Kang: *Defect-induced oxidation of graphite.* Phys. Rev. Lett. **82**, 1999 (1999).
- [81] G. Bräuchle, S. Richard-Schneider, D. Illig, J. Rockenberger, R. D. Beck, M. M. Kappes: *Etching nanometer sized holes of variable depth from carbon cluster impact induced defects on graphite surfaces.* Appl. Phys. Lett. **67**, 52 (1995).
- [82] C. Bartsch: *Rastersondenmikroskopie an ligandenstabilisierten Metallclustern.* Thesis, Institute of Applied Physics, University of Hamburg, Germany (2000).
- [83] M. Holmberg, A. Kühle, J. Garnaes, K. A. Morch, A. Boisen: *Nanobubble trouble on gold surfaces.* Langmuir **19**, 10510 (2003).
- [84] A. Thess, R. Lee, P. Nikolaev, H. Dai, P. Petit, J. Robert, C. Xu, Y. H. Lee, S. G. Kim, A. G. Rinzler, D. T. Colbert, G. E. Scuseria, D. Tománek, J. E. Fischer, R. E. Smalley: *Crystalline ropes of metallic carbon nanotubes.* Science **273**, 483 (1996).
- [85] The Smalley group: <http://smalley.rice.edu/> .
- [86] L. C. Venema: *Electronic structure of carbon nanotubes.* Thesis, Department of Nanoscience and DIMES, Delft University of Technology, The Netherlands (2000).
- [87] S. J. Tans, M. H. Devoret, H. Dai, A. Thess, R. E. Smalley, L. J. Geerligs, C. Dekker: *Individual single-wall carbon nanotubes as quantum wires.* Nature **386**, 474 (1997).
- [88] M. Bockrath, D. H. Cobden, P. L. McEuen, N. G. Chopra, A. Zettl, A. Thess, R. E. Smalley: *Single-electron transport in ropes of carbon nanotubes.* Science **275**, 1922 (1997).
- [89] M. Bockrath, D. H. Cobden, J. Lu, A. G. Rinzler, R. E. Smalley, L. Balents, P. L. McEuen: *Luttinger-liquid behaviour in carbon nanotubes.* Nature **397**, 598 (1999).
- [90] S. J. Tans, C. Dekker: *Potential modulations along carbon nanotubes.* Nature **404**, 834 (2000).
- [91] T. Ando, T. Nakanishi, R. Saito: *Berry's phase and absence of back scattering in carbon nanotubes.* J. Phys. Soc. Japan **67**, 2857 (1998).

-
- [92] P. L. McEuen, M. Bockrath, D. H. Cobden, Y. G. Yoon, S. G. Louie: *Disorder, pseudospins, and backscattering in carbon nanotubes*. Phys. Rev. Lett. **83**, 5098 (1999).
- [93] M. Bockrath, W. Liang, D. Bozovic, J. H. Hafner, C. M. Lieber, M. Tinkham, H. Park: *Resonant electron scattering by defects in single-walled carbon nanotubes*. Science **291**, 283 (2001).
- [94] M. T. Woodside, P. L. McEuen: *Scanned probe imaging of single-electron charge states in nanotube quantum dots*. Science **296**, 1098 (2002).
- [95] T. Ando: *Theory of transport in carbon nanotubes*. Semicond. Sci. Technol. **15**, R13 (2000).
- [96] J. W. G. Wildöer, L. C. Venema, C. Dekker, A. G. Rinzler, R. E. Smalley: *Electronic structure of atomically resolved carbon nanotubes*. Nature **391**, 59 (1998).
- [97] S. J. Tans, C. Dekker: *Fullerene ‘crop circles’*. Nature **385**, 781 (1997).
- [98] T. Vossmeier, S. W. Chung, W. M. Gelbart, J. R. Heath: *Surprising superstructures: Rings*. Adv. Mater. **10**, 351 (1998).
- [99] R. Martel, H. R. Shea, P. Avouris: *Rings of single-walled carbon nanotubes*. Nature **398**, 299 (1999).
- [100] H. R. Shea, R. Martel, P. Avouris: *Electrical transport in rings of single-wall nanotubes: One-dimensional localization*. Phys. Rev. Lett. **84**, 4441 (2000).
- [101] M. Sano, A. Kamino, J. Okamura, S. Shinkai: *Ring closure of carbon nanotubes*. Science **293**, 1299 (2001).
- [102] L. C. Venema, V. Meunier, P. Lambin, C. Dekker: *Atomic structure of carbon nanotubes from scanning tunneling microscopy*. Phys. Rev. B **61**, 2991 (2000).
- [103] L. C. Venema, J. W. G. Wildöer, J. W. Janssen, S. J. Tans, H. L. J. T. Tuinstra, L. P. Kouwenhoven, C. Dekker: *Imaging electron wave functions of quantized energy levels in carbon nanotubes*. Science **283**, 52 (1999).
- [104] S. G. Lemay, J. W. Janssen, M. v. d. Hout, M. Mooij, M. J. Bronikowski, P. A. Willis, R. E. Smalley, L. P. Kouwenhoven, C. Dekker: *Two-dimensional imaging of electronic wavefunctions in carbon nanotubes*. Nature **412**, 617 (2001).
- [105] W. Liang, M. Bockrath, D. Bozovic, J. H. Hafner, M. Tinkham, H. Park: *Fabry-Perot interference in a nanotube electron waveguide*. Nature **411**, 665 (2001).

-
- [106] M. Morgenstern, D. Haude, C. Meyer, R. Wiesendanger: *Experimental evidence for edge-like states in three-dimensional electron systems*. Phys. Rev. B **64**, 205104 (2001).
- [107] T. Hertel, R. Fasel, G. Moos: *Charge-carrier dynamics in single-wall carbon nanotube bundles: A time-domain study*. Appl. Phys. A **75**, 449 (2002).
- [108] S. G. Lemay: (unpublished) .
- [109] M. Ouyang, J. L. Huang, C. M. Lieber: *One-dimensional energy dispersion of single-walled carbon nanotubes by resonant electron scattering*. Phys. Rev. Lett. **88**, 066804 (2002).
- [110] T. Hertel, G. Moos: *Influence of excited electron lifetimes on the electronic structure of carbon nanotubes*. Chem. Phys. Lett. **320**, 359 (2000).
- [111] C. Kane, L. Balents, M. P. A. Fisher: *Coulomb interactions and mesoscopic effects in carbon nanotubes*. Phys. Rev. Lett. **79**, 5086 (1997).
- [112] H. Ishii, H. Kataura, H. Shiozawa, H. Yoshioka, H. Otsubo, Y. Takayama, T. Miyahara, S. Suzuki, Y. Achiba, M. Nakatake, T. Narimura, M. Higashiguchi, K. Shimada, H. Namatame, M. Taniguchi: *Direct observation of Tomonaga-Luttinger-liquid state in carbon nanotubes at low temperatures*. Nature **426**, 540 (2003).

Publications

- **Th. Maltezopoulos**, A. Bolz, Chr. Meyer, Chr. Heyn, W. Hansen, M. Morgenstern, and R. Wiesendanger:
Wave-function mapping of InAs quantum dots by scanning tunneling spectroscopy
Phys. Rev. Lett. **91**, 196804 (2003)
- **Th. Maltezopoulos**, A. Kubetzka, M. Morgenstern, R. Wiesendanger, S. G. Lemay, and C. Dekker:
Direct observation of confined states in metallic single-walled carbon nanotubes
Appl. Phys. Lett. **83**, 1011 (2003)
- N. Duhayon, P. Eyben, M. Fouchier, T. Clarysse, W. Vandervorst, D. Alvarez, S. Schoemann, M. Ciappa, M. Stangoni, W. Fichtner, P. Formanek, V. Raineri, F. Giannazzo, D. Goghero, Y. Rosenwaks, R. Shikler, S. Saraf, S. Sadewasser, N. Barreau, T. Glatzel, M. Verheijen, S. A. M. Mentink, M. von Sprekelsen, **Th. Maltezopoulos**, R. Wiesendanger, and L. Hellemans:
Assessing the performance of two dimensional dopant profiling techniques
Ultra Shallow Junctions (2003) 215.
Accepted for publication in J. Vac. Sci. Technol. B, January or February 2004.
- A. Bolz, A. Zolotaryov, Chr. Heyn, C. Kumpf, **Th. Maltezopoulos**, F. Wu, A. Stahl, W. Hansen, and R. L. Johnson:
Grazing-incidence x-ray diffraction on InAs/AlAs quantum dots
HASYLAB Annual Report (2003)

Contributions to conferences and workshops

- Th. Maltezopoulos, M. Tews, M. Morgenstern, A. Rogach, S. Haubold, and R. Wiesendanger:
Halbleiter-Cluster für die Rastertunnelspektroskopie
Frühjahrstagung der Deutschen Physikalischen Gesellschaft
Hamburg, Germany, March 26, 2001 (poster)
- Th. Maltezopoulos, M. Morgenstern, A. Rogach, S. Haubold, D. Talapin, and R. Wiesendanger:
RTM und RTS an ligandenstabilisierten Halbleiter-Clustern
Nachwuchswissenschaftlerworkshop des DFG-Schwerpunktes
"Halbleiter- und Metallcluster als Bausteine für organisierte Strukturen"
Mülheim/Ruhr, Germany, April 20, 2001 (talk)
- Th. Maltezopoulos, A. Bolz, J. Klijin, Chr. Meyer, V. Hagen, Chr. Heyn, D. Talapin, A. Rogach, M. Morgenstern, and R. Wiesendanger:
Rastertunnelmikroskopie und -spektroskopie an Halbleiter-Quantenpunkten
Frühjahrstagung der Deutschen Physikalischen Gesellschaft
Regensburg, Germany, March 11, 2002 (poster)
- Th. Maltezopoulos:
Präparation von Nanostrukturen für Rastertunnelmikroskopie und -spektroskopie
Diskussions-Seminar über aktuelle Probleme der Rastensorphysik
Hamburg, Germany, May 15, 2002 (talk)
- Th. Maltezopoulos, A. Bolz, J. Klijin, Chr. Meyer, V. Hagen, M. Tews, D. Talapin, A. Rogach, Chr. Heyn, M. Morgenstern, and R. Wiesendanger:
Scanning probe microscopy and spectroscopy on semiconductor quantum dots
Euresco Conference "Cluster-surface interactions"
Granada, Spain, June 1, 2002 (poster)
- Th. Maltezopoulos:
Scanning tunneling spectroscopy applied to nanostructures
Workshop des Graduiertenkollegs
"Design and Characterisation of Functional Materials"
Berlin-Wandlitz, Germany, October 11, 2002 (talk)

- Th. Maltezopoulos:
Confined states in single-walled carbon nanotubes
Seminar über Nahfeldgrenzflächenphysik und Nanotechnologie
Hamburg, Germany, November 11, 2002 (talk)
- Th. Maltezopoulos:
Rastertunnelspektroskopie an verspannungsinduzierten InAs-Quantenpunkten
Seminar über Nahfeldgrenzflächenphysik und Nanotechnologie
Hamburg, Germany, January 6, 2003 (talk)
- Th. Maltezopoulos, A. Bolz, Chr. Meyer, M. v. Sprekelsen, Chr. Heyn,
M. Morgenstern, and R. Wiesendanger:
*Scanning capacitance microscopy and scanning tunneling spectroscopy applied
to strain-induced InAs quantum dots*
Herculas project meeting
Berlin-Wannsee, Germany, February 13, 2003 (talk)
- Th. Maltezopoulos, A. Kubetzka, M. Morgenstern, S. G. Lemay, C. Dekker,
and R. Wiesendanger:
*Rastertunnelspektroskopie an defektinduzierten Quantenpunktzuständen in
single-walled Carbon Nanotubes*
Frühjahrstagung der Deutschen Physikalischen Gesellschaft
Dresden, Germany, March 24, 2003 (talk)
- Th. Maltezopoulos, A. Bolz, Chr. Meyer, Chr. Heyn, W. Hansen,
M. Morgenstern, and R. Wiesendanger:
Wave-function mapping of strain-induced InAs quantum dots
12th international conference on scanning tunneling microscopy/spectroscopy
and related techniques
Eindhoven, Netherlands, July 21, 2003 (talk)
- Th. Maltezopoulos, A. Kubetzka, A. Bolz, Chr. Meyer, Chr. Heyn,
W. Hansen, M. Morgenstern, R. Wiesendanger, S. G. Lemay, C. Dekker,
D. Talapin, and H. Weller:
Electronic states in nanostructures studied by scanning tunneling spectroscopy
Workshop des Graduiertenkollegs
"Design and Characterisation of Functional Materials"
Leck, Germany, October 17, 2003 (talk)
- Th. Maltezopoulos, A. Bolz, Chr. Meyer, Chr. Heyn, W. Hansen,
M. Morgenstern, and R. Wiesendanger:
*Wave-function mapping of InAs quantum dots by scanning tunneling
spectroscopy*
Seminar über ausgewählte Kapitel der Festkörperphysik, -technologie und
Photonik
Berlin, Germany, November 10, 2003 (talk)

Acknowledgements

At the end, I would like to thank everybody who contributed to this work:

My doctoral thesis supervisor Prof. Dr. Roland Wiesendanger integrated me into his excellent group and gave me the opportunity to accomplish very exciting studies.

My direct supervisor was Dr. Markus Morgenstern. His good expertise, daily help, and friendly motivation made this thesis possible. He always believed in the project even at very hard times. He is the best supervisor one can desire!

Dr. Jan Klijn and Dr. Christian Meyer showed me the world of low temperature UHV STM and, additionally, I want to thank Dr. Daniel Haude for his help in the lab. It was a very funny and productive time in lab 014, which I will definitely miss.

I will also definitely miss the time in the "nanobrother container". All members of the subgroup nanoelectronics contributed to a very familiar atmosphere. It was always work and pleasure. Additionally, I want to thank Lilli Sacharow for her help in theory and as my "private secretary" and Dr. Martin Janson for a lot of useful discussions and for the correction of the present manuscript.

The low temperature UHV STM measurements on nanotubes have been done in cooperation with Dr. André Kubetzka. I remember some long August nights in lab 013 where we obtained for the first time atomic resolution on the carbon nanotubes.

Volker Hagen showed me how to use the air AFMs and we had an unforgettable time in lab 102 and 103. For the SCM measurements I got help from Dr. Axel Born, Johannes Isenbart, and Martin von Sprekelsen.

I want to thank Dr. Alexander Schwarz for a lot of useful discussions concerning AFM and I also want to thank Dr. Makoto Ashino and Timo Behnke for cooperation in the carbon nanotube project.

Norbert Dix helped me with the construction of various devices and prepared the Au on mica substrates. Together we found out that he knows Greece better than I do but I know Germany better than he does.

In short, I want to thank all group R members for their cooperation and support during my PhD thesis.

I presented results of three projects in this thesis. They would have been impossible without a good collaboration between different groups.

Arne Bolz and Dr. Christian Heyn in the group of Prof. Dr. Wolfgang Hansen grew the strain-induced InAs QDs. I worked often together with Arne Bolz and it was always a very exciting and good time. I will never forget how we pulled the first sample out of the MBE and our "Friday Alster jogging". Additionally, I want to thank Dr. Christian Heyn and Prof. Dr. Wolfgang Hansen for fruitful discussions and help.

Dr. Dimitri Talapin and Dr. Andrey Rogach in the group of Prof. Dr. Horst Weller did the chemical synthesis of the semiconductor nanocrystals. I hope that this effort will also lead to wave-function mapping in the future.

Ralf Wellmann in the group of Prof. Dr. Manfred Kappes prepared the nanopit samples, which were used for cluster preparation.

The single-walled carbon nanotubes were prepared in the group of Prof. Dr. Richard E. Smalley. I learned the preparation of nanotubes on Au from Dr. Serge G. Lemay in the group of Prof. Dr. Cees Dekker in Delft, The Netherlands. I want to thank them for integrating me into their group for one week and for a very good cooperation afterwards via e-mail.

Haiko Rolff made the electrical bonds of the nanotube samples for STM measurements.

I gratefully acknowledge discussions with Michael Tews and Prof. Dr. Daniela Pfannkuche about nanocrystals and Stark effect.

For the introduction into self-assembled monolayers I thank Dr. Markus Brunnbauer, Dr. Alexander Bittner, and Dr. Erik Scher. I also want to thank Prof. Dr. Uri Banin for discussions about nanocrystal preparations.

A lot of adapters and equipment were built by the mechanical and electrical workshops. I want to thank Rolf-Peter Benecke and Horst Biedermann representative for all their co-workers for their competent help in the past years.

I got financial support from the EU Project "Herculus" and I was associated member of the Graduiertenkolleg "Design and Characterization of Functional Materials".

Last but not least, I want to thank all of my friends and, especially, my parents Christoforos and Sofia Maltezopoulos for their support during my entire study.

Lebenslauf

Name: Theophilos Maltezopoulos
Anschrift: Schwarzenbergstraße 56
21073 Hamburg
e-mail: tmaltezo@physnet.uni-hamburg.de
Tel.: +49-40-42838-3051
Privat: +49-40-7659120

Geburtsdatum/-ort 14. August 1974 in Hamburg

Staatsangehörigkeit griechisch
Familienstand ledig

Schulbildung

1980 – 1981 Vorschule SCHULE KERSCHENSTEINERSTRASSE
in Hamburg
1981 – 1985 Grundschule SCHULE KERSCHENSTEINERSTRASSE
in Hamburg
1985 – 1994 Gymnasium FRIEDRICH-EBERT-GYMNASIUM
in Hamburg

Schulabschluß

Juni 1994 Abitur mit Gesamtnote: 2,2

Studium

1994 – 2000 Studium der Physik UNIVERSITÄT HAMBURG
Oktober 1996 Vordiplom mit Gesamtnote: „sehr gut“
April 1999 – Mai 2000 Diplomarbeit am Institut für Angewandte Physik, Universität
Hamburg, in der Gruppe von Prof. Dr. R. Wiesendanger, Thema: „*Deposition von ligandenstabilisierten InAs-Clustern auf HOPG*“

Studienabschluß

Mai 2000 Hauptdiplom mit Gesamtnote: „sehr gut“

Promotion

August 2000 – Januar 2004 Anfertigung der Doktorarbeit am Institut für Angewandte
Physik, Universität Hamburg, in der Gruppe von Prof. Dr. R. Wiesendanger, Thema: „*Wave-function mapping of electronic states in nanostructures by scanning tunneling spectroscopy*“